

# 3D Printing

A study of the intralayer bonding strength of extrusion-based additively manufactured polymers and its relevance for the design of structural elements.

C.L. Helmer

**Aectual**

**DUS**

 **TU Delft**

 **TEN  
TECH**

# 3D Printing

A study of the intralayer bonding strength of  
extrusion-based additively manufactured  
polymers and its relevance for the design of  
structural elements

by

C.L. Helmer

to obtain the degree of Master of Science  
at the Delft University of Technology,  
to be defended publicly on Friday February 22, 2019 at 15:30.

Student number: 4087402  
Project duration: November 1, 2017 – February 22, 2019  
Thesis committee: Prof. ir. R. Nijssse, TU Delft, chair  
Dr. ir. F. A. Veer, TU Delft  
Dr. ir. H. R. Schipper, TU Delft  
Ir. R. Houtman, Tentech B.V.

**Aectual**

**DUS**

 **TU Delft**

 **TEN  
TECH**

# Abstract

The additively manufacturing industry is emerging rather quickly and has find its way within numerous fields of expertise. Slowly the building industry is adopting these fabrication methods as well, but there are still a lot of challenges. Especially the bonds within the layered structure are demand more research. Numerous researches have acknowledged the importance of the bonding strength, but only a few have actually examined its mechanical properties of the bonds.

A distinction between the interlayer and intralayer bonds is made. The former indicates the bonds between vertically stacked layers, while the latter is related to the coalescence between filament within one lamina. This report assesses the relevance of the intralayer bonding strength for extrusion-based additive manufacturing by the large-scale printers of company Aectual. Firstly, the complete fabrication process and the relevant parameters for the construction of 3D printed object are elaborated. Based on the layered structure of prints and regarding the desired geometries, the additively manufactured products are linked to Unidirectional Fibre Reinforced Composites. Subsequently, the international standards of the ISO and the ASTM are consulted for the design of the test specimens for the estimation of the material properties of interest, namely the tensile and flexural test for general understanding of the mechanical behaviour of the material and a test method for the Interlaminar Fracture Toughness to evaluate the intralayer bond strength.

As the preliminary have shown promising result, the print geometry and the printing settings are optimised to achieve a high print quality and reliable test result as uniform as possible. The results of the flexural and tensile test indicated that this optimisation have proven to be successful. Despite the high number of test specimen, the interlaminar fracture toughness of the intralayer bond is not quantified. The post-processing of the insert relevant for delamination affected the crack front and reduced the probability of deformation. Nevertheless, almost 30% of the samples have delaminated and have confirmed the dependability of the bonding strength on the height of the print and the printed pattern. Moreover, the print orientation appears to be of significant relevance. Finally, this research appoints the importance of the intralayer bonds for the mechanical behaviour of the total product as well as for the further development of 3D printed structural elements.

# Contents

<b>1</b>	<b>Introduction</b>	<b>1</b>
1.1	Dare to pioneer . . . . .	1
1.2	The ultimate goal . . . . .	2
1.3	The objective of this research . . . . .	3
1.3.1	The particulars of Additive Manufacturing . . . . .	3
1.3.2	The weakest link . . . . .	4
1.4	The outline of this research . . . . .	4
<b>2</b>	<b>Additively Manufacturing</b>	<b>5</b>
2.1	The principles . . . . .	5
2.2	The extrusion process . . . . .	6
2.3	The mesostructure . . . . .	7
2.4	Print parameters . . . . .	8
2.5	The bonding process . . . . .	9
2.5.1	Thermal development . . . . .	9
2.5.2	Thermal history . . . . .	10
2.6	Residual stresses. . . . .	12
2.6.1	The bond strength . . . . .	12
2.7	The capacity of an additively manufactured structure . . . . .	12
<b>3</b>	<b>Test description</b>	<b>14</b>
3.1	Expected material behaviour. . . . .	15
3.1.1	Comparable materials . . . . .	15
3.1.2	Type of Composite . . . . .	16
3.2	Tensile Strength . . . . .	16
3.2.1	Dimensions of the tensile specimen . . . . .	17
3.3	Flexural Strength . . . . .	17
3.3.1	Dimensions of the flexural specimen . . . . .	18
3.4	Interlaminar Fracture Toughness . . . . .	19
3.4.1	The principles of Fracture Mechanics . . . . .	19
3.4.2	Load-displacement records . . . . .	20
3.4.3	The compliance method . . . . .	22
3.4.4	Testing methods . . . . .	23
3.4.5	Test setup . . . . .	25
3.4.6	Dimensions of the delamination specimen . . . . .	26
<b>4</b>	<b>Fabrication of the test specimens</b>	<b>27</b>
4.1	Two 3D Printers. . . . .	27
4.1.1	KamerMaker 1 and 2 . . . . .	27
4.1.2	Static and Track Robots . . . . .	28
4.2	Print geometries . . . . .	28
4.2.1	Restrictions regarding the print path. . . . .	28
4.2.2	Horizontal limitations . . . . .	28
4.2.3	Vertical limitations . . . . .	29
4.3	Material . . . . .	29
4.4	Optimisation of the extruded polymer . . . . .	31
4.4.1	Resizing the print geometry . . . . .	32

4.5	Orientation of the prints . . . . .	32
4.6	Process parameters . . . . .	32
4.6.1	The extrusion temperature . . . . .	32
4.6.2	Envelope temperature . . . . .	33
4.6.3	Build location . . . . .	33
4.6.4	Print height . . . . .	33
4.6.5	The print pattern . . . . .	33
4.7	Preparation of the specimens . . . . .	34
4.7.1	Post-processing . . . . .	34
4.7.2	Marking the specimens. . . . .	34
<b>5</b>	<b>Results</b>	<b>35</b>
5.1	Tensile test . . . . .	35
5.1.1	Evaluation of the specimens after testing . . . . .	36
5.1.2	Determination of tensile properties . . . . .	37
5.1.3	Test results . . . . .	38
5.2	Flexural test. . . . .	40
5.2.1	Evaluation of the specimens after testing . . . . .	40
5.2.2	Determination of the flexural properties . . . . .	40
5.2.3	Test results . . . . .	41
5.3	Mode II Delamination test . . . . .	43
5.3.1	Examination of the tested specimens . . . . .	43
5.3.2	Test results . . . . .	44
5.4	Summary . . . . .	48
5.5	Design criteria . . . . .	48
<b>6</b>	<b>Summary</b>	<b>51</b>
6.1	Previous research . . . . .	51
6.2	Test setup . . . . .	51
6.2.1	Tensile test . . . . .	52
6.2.2	Flexural test. . . . .	52
6.2.3	Interlaminar fracture toughness test . . . . .	52
6.3	Influential factors on the intralayer bonding strength . . . . .	52
<b>7</b>	<b>Conclusions</b>	<b>53</b>
7.0.1	Prior knowledge . . . . .	53
7.1	Determination of the bond strength . . . . .	53
7.2	Influential factors . . . . .	53
7.3	The relevance of the intra layer bonds . . . . .	54
<b>8</b>	<b>Recommendation</b>	<b>55</b>
8.1	Test specimens . . . . .	55
8.2	Further research . . . . .	55
<b>A</b>	<b>Properties of feed material</b>	<b>56</b>
<b>B</b>	<b>Print patterns for the single layered, double layered and delamination geometries</b>	<b>59</b>
<b>C</b>	<b>Parameters of the cross-section</b>	<b>63</b>
C.1	Parameters . . . . .	63
C.1.1	Cross-section of the core. . . . .	63
C.1.2	Cross-section of the ribs . . . . .	63
C.1.3	Number of ribs . . . . .	64
C.1.4	Total area of the cross-section . . . . .	64
C.2	Centre of gravity . . . . .	65
C.2.1	Centre of gravity of the core element . . . . .	65
C.2.2	Centre of gravity of the ribs . . . . .	65
C.3	Moment of inertia . . . . .	66
C.3.1	Moment of inertia of the core element. . . . .	66
C.3.2	Moment of inertia of the ribs . . . . .	66

---

<b>D</b>	<b>The equivalent length</b>	<b>69</b>
D.1	Previous researches . . . . .	69
D.1.1	Definition of the width as function of the length . . . . .	69
D.1.2	Deformation of the specimen . . . . .	70
D.1.3	The equivalent length . . . . .	71
D.2	Deviation from previous reports . . . . .	71
<b>E</b>	<b>Domain of Tensile Chord Modulus</b>	<b>73</b>
<b>F</b>	<b>Raw data - Tensile Test</b>	<b>75</b>
<b>G</b>	<b>Domain of Flexural Chord Modulus</b>	<b>80</b>
<b>H</b>	<b>Raw data - Flexural Test</b>	<b>82</b>
<b>I</b>	<b>Raw data - Mode II Interlaminar Fracture Toughness Test</b>	<b>87</b>
<b>J</b>	<b>Estimation of Characteristic values</b>	<b>94</b>
J.1	Coefficient of variation . . . . .	94
J.2	The characteristic fractile factor . . . . .	95
<b>K</b>	<b>Interlaminar Fracture Toughness of various adhesives and resins</b>	<b>96</b>
	<b>List of Figures</b>	<b>103</b>

# Introduction

The building industry is regarded as a low-tech industry<sup>80</sup>. Over the past centuries the principles of construction have not changed and improvements are mostly related to the acceleration of the production process instead of the development of new technologies. Safety and cost reduction are the main motives within this competitive industry and lead to small margins of time, money and energy available for innovation<sup>20</sup>. Therefore, the implemented innovations are often adopted from other industries as they already have proven to be safe and/or cost-reducing.

Aside from this conventional approach, this industry is also quite environmental unfriendly. It is responsible for at least 30% of all CO<sub>2</sub> emissions worldwide<sup>72</sup> and it is the second largest consumer of raw materials, after the food industry<sup>17</sup>. In 2014 the construction industry was accountable for 34.7% of waste material in the European Union<sup>1</sup> and very little of the waste is recycled and reintroduced in its original product line without loss of quality.<sup>41</sup>

As the conventional building industry has a large impact on the environment, the industry of Additively Manufacturing, also known as 3D Printing, may provide a solution. This fabrication method has the potential to significantly reduce the material waste<sup>36</sup>. Moreover, 3D Printing has the opportunity to reduce the fabrication cost of a single exclusive structural component that can be printed directly at the building site. But considering the size of structural components, the printers have to be much larger than the prevailing machines. Fortunately, due to the growing public interest in Additively Manufacturing, the possibilities for large scale fabrication are explored more and more<sup>37</sup>. As Wu et al.<sup>80</sup> has pointed out, the success of this fabrication method within the construction industry highly relies on the variability and the quality of printed material, the required fabrication time and the total production costs.

## 1.1. Dare to pioneer

3D Printing offers great opportunities to build complex geometries, reduce waste, require less manpower and contributes to the aim of mass customisation within the building industry. The mass customisation is related to the individualisation and contextualisation of structures, which means that parts of the structure can easily be adapted to individual preferences and contextual needs without completely re-evaluating the design. Furthermore, 3D printing promotes the integration of design and engineering, because obviously every adaptation of the design must be feasible and safe. Hence, although the focus of 3D printing is mainly on the design, the engineering and the material aspect is at least as important for the realisation of Additive Manufacturing<sup>36</sup>.

Since 2013, DUS. Architects is one of the pioneers that are exploring the opportunities of large-scale Additive Manufacturing by means of melt extrusion of polymers, which are preferably bio-based or recycled. What initially started with the dream to create a 3D printed canal house has grown into unique architectural company that use technological innovation to realise challenging projects for various notable companies. In 2017 DUS. Architects continued its research on digitally produced building components in a new firm, named Aectual. It is the company's goal to accomplish design freedom in its widest sense, reduce costs and produce no waste. Over the years they have

developed a wide scatter of products from which three groups can be distinguished:

- Full prints** This product are completely made out of 3D printed polymers and include façade panels, furniture and sculptures.
- Hybrids** This term refers to 3D printed objects that are combined with conventional products to create unique designs like the integration of 3D printed shapes and Terrazzo floors.
- Formwork** The 3D printed objects are designed to be filled with concrete. This fabrication method allows more complex shape than conventional castings. An good example is the concrete staircase that is produced by DUS. in 2015.



Figure 1.1: Full printed planters



Figure 1.2: Hybrid Floor



Figure 1.3: Staircase created with printed formwork

To release their dream, DUS. Architects and Aectual have co-operated with several engineering companies, including Tentech. Together with Tentech the structural purposes of the 3D printed products have been researched via several master theses. The first report dates back to November 2014 and was an exploratory research on the structural feasibility of full printed elements for the 3D print canal house<sup>74</sup>. Subsequently, the integration of steel cores in printed columns as improvement of its buckling resistance was examined<sup>51</sup>. After this second research, the focus shifted from full prints to formwork. The third research was dedicated to the estimation of engineering properties of single layered prints and the modelling of its mechanical behaviour<sup>13</sup>. This model was converted into the design of moulds that were shaped in a such away to cancel out its deformation due to hydrostatic pressure of the concrete. This topic was further investigated in the final research prior to this study. New materials were introduced, multilayered prints were examined and the planar patterns to withstand bigger deformations were implemented in the design of the moulds<sup>77</sup>. With new materials, the interest for full print products returned and DUS. have participated in a design contest for façades that should prevent vandalism of utility buildings. This generated new challenges and along with previous researches form the fundamentals for this research.

## 1.2. The ultimate goal

The ultimate goal for the is a computer model that predict the strength and deformation capacities of the façade over time. But to obtain a full-functional model, various aspects of the design of façade and the properties of the additively manufactured material had to be examined. The panel itself is divided in smaller segments, further indicated as cells, that can be adjusted by means of a parametric model. Meaning that it is possible that each individual cell of the façade have its own dimensions and shape. Hence, the properties of various configuration had to be tested and a correlation with its dimensions had to be established prior to the complete evaluation of the design. Within the cell element two core components are identified: the printed paths and the connections. The mechanical properties of the single and multiple layered print paths can be determined in similar fashion as in the previous



researches. However, the structural behaviour of the connections has not been examined before and require are more extensive research. Lastly, the past few years have learned that the (composition of) recycled materials used by DUS. Architects and Aectual as feed material can vary regularly. Hence, the designed model should be easily adapted for panels printed with other materials. In short, the preferred goal is a model to determine the structural behaviour of 3D printed panels based on one specific material, but is easily adapted for other materials. This can be broken down into the following topics:

- General material properties: tensile, flexural, shear tests,
- Mechanical properties of the connections within the façade,
- Estimation of the correlation between the shape of an individual cell and mechanical, properties by means of experiments for different configurations of the the cell,
- Design and validation of a model of an individual cell, which can be adjusted to preferred shapes,
- Implementation and validation of multiple cells in the model,
- Determination of time-dependent behaviour of the material and implementation in the model,
- Coupling of the parameteric model and the numerical model.

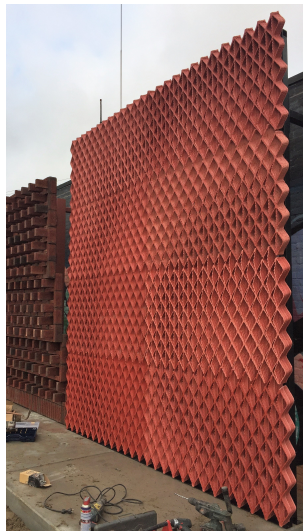


Figure 1.4: Façade designed by DUS. Architects

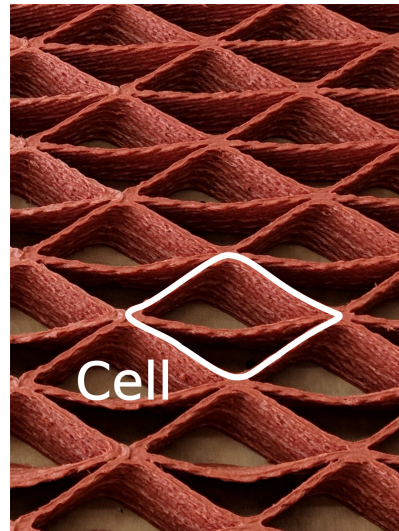


Figure 1.5: Façade is composed of cells

## 1.3. The objective of this research

Regarding the intended time span for this report, this research is related to the connection within the façade and its main purpose is to determine its relevance for the design of structural elements.

### 1.3.1. The particulars of Additive Manufacturing

Of the researchers personal interest are the fundamentals of Additive Manufacturing and its relevance for printed structural elements in general. Because despite of increasing interest by industry, academies and governments, a lot of the fundamental questions related to its mechanical behaviour are still unanswered. While various researchers have indicated that conventional mechanical properties are not adequate to model and predict the structural behaviour of this materials<sup>4</sup>. Furthermore, since the introduction of Additive Manufacturing 40 years ago, no standards have yet been established for the determination of its critical properties<sup>36</sup>.

The majority of researches related to Additive Manufacturing has focussed on Acrylonitrile Butadiene Styrene (ABS) which is the most commonly used feedstock material<sup>70</sup>. However, the materials used by Aectual have a higher crystallinity and which results in a more dramatic transitions in material

properties during the solidification process and results a more brittle behaviour of the material. Moreover, a lot of studies mainly focus on the process related requirements, but only a few account for the review on the requirement related to its implementation and structural properties like load-bearing resistance, thermal behaviour and deterioration factor<sup>36</sup>. However, the feasibility of additive manufacturing structural elements clearly depends on these construction related requirements. Hence, a detailed understanding of the relationship between this structural requirements and the parameters of the print process is an essential fundament for additive manufacturing of structural elements<sup>55,62,65,69</sup>.

### 1.3.2. The weakest link

When gaps are present between the bonded filaments, the load-bearing capacity in the cross-section is reduced. But even without gaps the bonds are regarded as an discontinuity due to a poorer molecular diffusion of polymers between adjacent filaments than in the filaments itself<sup>75</sup>. Consequently, the bonds introduce stress concentrations in the material and therefore enhance the change of failure<sup>3</sup>. This stress concentration develop, for instance, during shrinkage of the material. Hence, the bonds are the weakest link in the 3D printed structure. Accordingly, the relationship between the construction related requirements and the print process of a structural element can be evaluated by the bond strength of adjacent printed filaments within and between layers<sup>29,68,71</sup>. This is often referred to as the intra- and interlayer bond strength respectively. Moreover, comprehensive knowledge of the possible failure mechanisms will help to design geometries that prevent premature mechanical failure<sup>30</sup>. Regarding the evaluation of the bond strengths, earlier research have indicated that the interlayer shear strength can be greater than the intralayer shear strength<sup>40</sup>. The other strength properties of the bonds strongly depends on the printed geometry<sup>29,66</sup>.

## 1.4. The outline of this research

Given the desired printed geometries and there possible load conditions, failure of the intralayer bonds is assumed to be the most critical. When these bonds in connections fail, the connection loses its functionality. While fracture of the interlayer, only reduces the load bearing capacity of the connection. So, the objective of this research is to answer the follow main, which is supported by three sub-questions:

### What is the relevance of intralayer bonding of extrusion-based additively manufactured material for structural purposes?

- What is known within the 3D community about the bonding strength between filaments?
- Which failure test setup is the most relevant and reliable method for the determination of the bonding strength?
- What affects the intralayer bonding strength?

This research will first elaborate on the current knowledge within the additive manufacturing print community. This will result in the relevant print process parameters for the determination of the intralayer bond strength. Subsequently, the relevant test setups will be described to compare the material of interest with previous researches. All applicable test set-ups for the determination of the bonding strength will be evaluated and the most relevant and reliable test setup will be selected. The next part will elaborated on the fabrication of the test specimen taken into account the earlier reported print process parameters. Lastly, all specimens will be tested and the results will be evaluated. Based on the literature study and these test results, this report will conclude with the answers on the drafted main and sub questions.

# 2

## Additively Manufacturing

The principles of Additive Manufacturing originate back to the last quarter of the previous century. The ideas of a rapid prototyping system were introduced by Dr. Hideo Kodama of the Nagoya Municipal Industrial Research Institute in Japan, for which he applied a patent in May 1980<sup>79</sup>. He proposed a fabrication method that is based on the hardening properties of photosensitive polymers. Via a concentrated beam of UV-light the resin solidifies at specific locations on a horizontal plane. When the predefined pattern has been created, the plane is lowered into the liquid resin to cover the hardened polymers. Subsequently, a new pattern of solidified polymer is created, which adheres to the previous layer. After a sufficient amount of layers of photo-hardened polymer, a three-dimensional object has been created<sup>34</sup>. Unfortunately, due to a lack of funding his application was declined and the patent was later re-applied and assigned to Charles Hull<sup>32</sup>. But after all, the description of this so-called stereolithography process of Dr. Kodama is regarded as the fundament of Additive Manufacturing (AM), popularly known as 3D Printing.

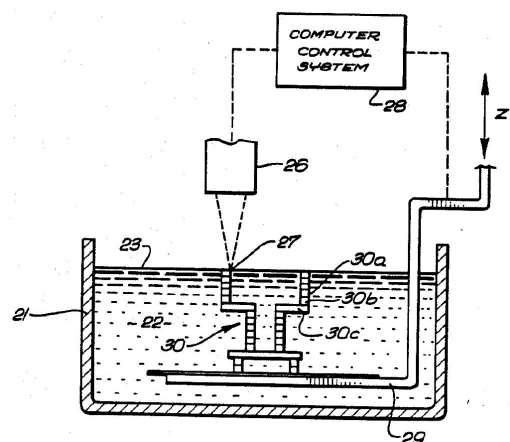


Figure 2.1: Sketch of a system for stereolithography in the patent of Charles Hull<sup>32</sup>

Over the past decades AM has evolved and improved quickly. Multiple print technologies for various materials have been introduced and 3D Printing has found its application in numerous areas, e.g. aerospace, architecture and medicine<sup>65</sup>. It is now one of the fastest growing production methods within the whole fabrication industry<sup>63</sup>.

### 2.1. The principles

Since the beginning of 3D printing, polymers have always predominated the AM industry. Although printing of steel products has been emerging quickly over the past few years, 65 percent of the printed products are still created out of polymers<sup>63</sup>. All polymers that provides sufficient support for the next layer by means of hardening within adequate time span are potential feed material for a 3D Printer<sup>80</sup>. This solidification process is usually initiated by means of removal of heat or a catalyst. The latter is either heat, light or change in pH which triggers polymerisation of a liquid polymer<sup>7</sup>.

The most commonly known technology is the Fused Deposition Modelling (FDM), which is capable to produce durable and inexpensive objects at relatively high speed<sup>35</sup>. Besides thermoplastics, the technology has been developed for numerous other materials, e.g. metals, glass, ceramics. It was introduced, commercialised and trademarked by Strataysys Inc. in 1991 and the technology has been widely adopted<sup>4</sup>. Because of the trademark<sup>64</sup>, this process is also appointed as Fused Filament Fabrication (FFF) or Extrusion-based Additive Manufacturing (EAM). The last term is also used to refer to the fabrication process of Aectual, because the feed materials is provided in the form of

pellets instead of a filament.

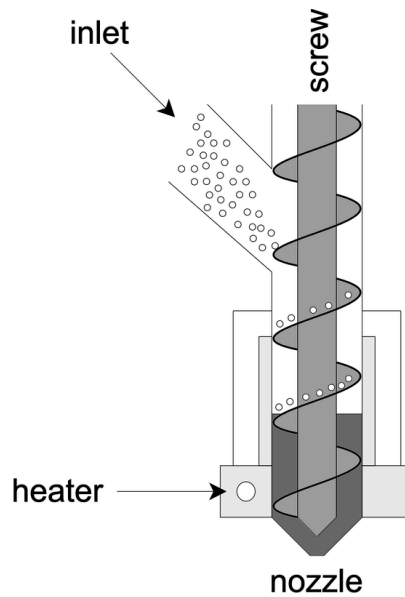


**Figure 2.2:** The core elements of the printhead<sup>23</sup>

The thermoplastic is fed to the print head of the 3D Printer, where it is heated above its glass transition point,  $T_g$  and extruded via nozzle on a platform in a predefined pattern. The key characteristic of an appropriate feed material are its pumpability, printability, buildability and open time<sup>37</sup>. The first term refers to the ease of delivering to and liquefy the feed material by the heater. The feed material is the raw thermoplastic supplied in the form of a filament or pellets prior to printing. The second term evaluates the deposition of the liquefied material by the extruder. The buildability evaluates the resistance of the extruded material against loads during the solidification process. It is often linked to deformation of the printed bead by for example gravity and warping. The last term is defined as the period where these key characteristic do not change significantly.

## 2.2. The extrusion process

In the printer head the material is under a certain amount of pressure before extrusion. When the material leaves the nozzle of the print head, the material is allowed to move freely and its stored elastic energy is released. This results in expansion of the bead in radial direction, also known as die swelling<sup>71</sup>. The dimensions of the extruded bead depends on the geometry of the nozzle, the mechanical properties of the raw material and the movement of the printhead. As is indicated by Agarwala et al.<sup>2</sup>, the width the road extruded through a circular opening is usually 1.2 to 1.5 bigger than the diameter of nozzle.

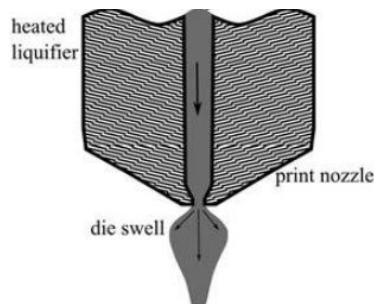


**Figure 2.3:** Die swelling of the extruded material<sup>71</sup>

A circular opening will result in an oblong shape of the bead after extrusion due to gravity and the interaction with its support. During solidification the viscosity of the thermoplastic will increase. Hence, the spreading of the bead is depended on the cooling rate. As the resolution of print is determined by the height and width of each layer, a slower solidification process will increase the resolution. However, more layers are required to create the object and thus the printing time will increase.

In addition to the nozzle diameter, the dimensions of the printed road is influenced by the volumetric flow rate and the head speed as well. A higher speed will result in smaller road, but will decrease the required build time. The print speed is limited by the minimum cross-sectional area of the bead, because a smaller area will result into tearing of the printed road<sup>21</sup>.

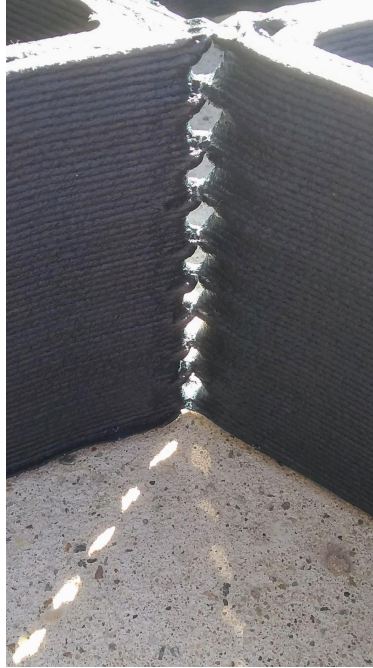


**Figure 2.4:** Insufficient volumetric flow rate at the corners



**Figure 2.5:** Insufficient volumetric flow rate at the joint

Finally, the printed road is also affected by the volumetric flow rate, i.e. the amount of material extruded per unit time. This related to the preferred geometry and can vary along the print path. Sharp corners, for instance, need a sufficient amount of printed material to prevent it from being dragged along the print path<sup>70</sup>. Lastly, the build speed is determined by the solidification rate, because the printed filament must have hardened sufficiently to support the next layer. Obviously, the relevance of this limitation is depending on the size of the desired object as bigger geometry resulting in an longer printing time per layer.

## 2.3. The mesostructure

Apart from the building speed, the solidification process is also relevant for the bonding of adjacent filaments. The extruded material must have a sufficient amount of time to adhere to its neighbouring elements, otherwise the printed material is not able to support the successive layers and the strength of additively manufactured object is significantly reduced.

As the bond formation strongly affects the strength of the material, a further evaluation of the so-called mesostructure is rather important. For a additively manufactured product, three different scales can be identified<sup>15</sup>:

- the Microstructure** It is related to a single printed filament or bond between two adjacent filament within or between layers.
- the Macrostructure** This is the complete additively manufactured object. Each printed layer is usually regarded as a lamina.
- the Mesostructure** Referring to a part of the geometry, which includes multiple filaments and bonds that interact with each other within and across successive layers.

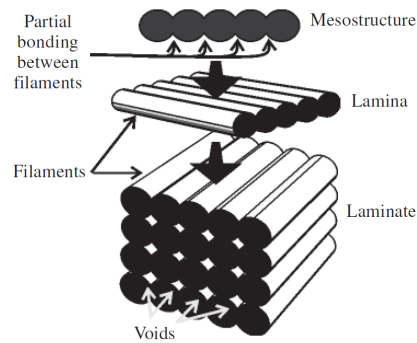


**Figure 2.6:** Composition of 3D printed structure<sup>15</sup>

Regarding the evaluation of the mechanical properties of a 3D printed object, it is of most relevance to evaluate its mesostructure<sup>56</sup>. The mesostructure is determined by the porosity of the material and the extent of fibre bonding<sup>54</sup>. Due to the elliptical shape of the printed filaments, the coalescence of a printed road with the surrounding filaments varies per principle direction. As depicted in figure 2.7, the first principle direction is along the print path, the second is transversely orientated with the printed layer and the third direction is pointed in the vertical print direction. The strength along the print path is determined by the properties of the printed filaments and the so-called void density, which is defined as ratio of the area of the gaps between the filaments and the total cross-sectional area<sup>54</sup>. While the other directions are affected by the degree of bonding between the filaments as well as the presence of gaps. Two different type of bonding can be identified: intralayer and interlayer bonds. The former refers to the coalescence between adjacent fibres within one layer, while the latter indicates the cohesion between fibres in different layers. Consequently, mechanical behaviour of 3D printed structures is characterised as orthotropic<sup>16,24</sup>.

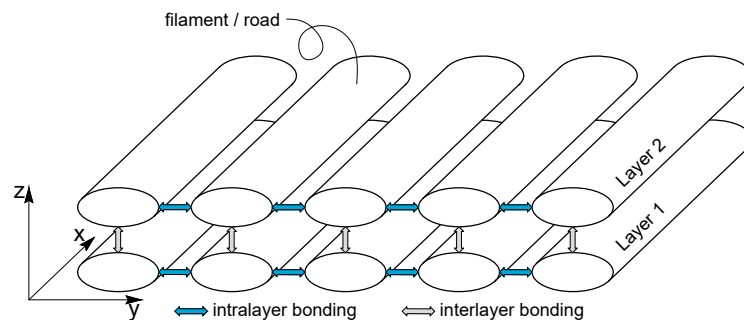


**Figure 2.7:** The mesostructure of an additively manufactured product

## 2.4. Print parameters

The mechanical properties of the macrostructure are affected by specific parameters related to the hardware and the software of the 3D-printer. The increment of nozzle for each layer, the extrusion flow rate, the envelope temperature and extrusion temperature are proprieties related to the printer and therefore part of the hardware. The fibre-to-fibre gap, the print path, the rotation orientation of the layers relative to each other and the layer translation configuration are part of the design of the geometry are software parameters. The layer rotation orientation is the direction of the print path compared to the previous layers, while the layer translation configuration is related to the shift of the fibres in vertical print direction, i.e. skewed or aligned<sup>54</sup>.

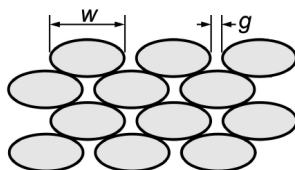


**Figure 2.8:** Skewed Configuration<sup>54</sup>

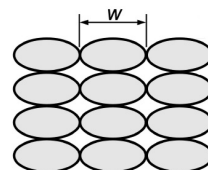


**Figure 2.9:** Aligned Configuration<sup>54</sup>

Take into account that a reduction of the fibre-to-fibre gap will lower the void-density and may increase the transverse strength of the print. Especially, when sharp corners in the junction between adjacent roads are diminished. As the bonds already have decreased mechanical properties due to insufficient coalescence of the fibres, the sharp edges of the void will further enhance this discontinuity. Subsequently, the discontinuities will introduce stress concentrations and therefore, promote failure of the bond<sup>21</sup>. However, if the gap is closed, but no sufficient bond formation is established, this will result in distortion of adjacent filaments or even jamming of the print head due to excessive material build up<sup>54</sup>. Hence, the bond formation is really important for the mechanical properties of the additively manufactured material.

## 2.5. The bonding process

As the bonding of the filaments is a thermal driven process<sup>66</sup>, the envelope and extrusion temperature have obviously a influences on the print quality. A higher temperature will decrease the viscosity of the thermoplastic and increase the spreading of the printed bead. Hence, the interface with the sublayer increases<sup>4</sup>. However, elevated temperatures can also cause degradation of the polymer and reduces the strength of the final product and can even clog the nozzle of the printhead<sup>71</sup>. Besides the temperature settings, the contact area between adjacent filaments is relevant to consider in the design of the mesostructure. This mainly affected by the gap size, extrusion rate and the translation of layers. In order to improve the mechanical properties of the print by adjusting these print parameters, a better understanding of the thermal process is required.

The bonding process of two adjacent filaments is visualised in figure 2.10 and is a result of several mechanisms. As soon as a bead is deposited the bonding process starts with the sintering of the bead with adjacent material: (1) and (2). In this process coalescence is established between the bead and neighbouring filaments without liquefaction of the material and is mainly driven by surface tension<sup>14</sup>. This process responsible for most of the neck-growth and is stopped as the temperature drops underneath the material related critical sintering temperature<sup>66</sup>. Research have indicated the temperature drops rather quickly, hence this strong bond formation occurs only during a fraction of time. According to Bellehumeur et al.<sup>15</sup>, this sintering process is mainly affected due to temperature of the extruder rather than the envelope temperature.

Below the critical sintering temperature, it is assumed that the bonds grow due to creep deformation and intermolecular diffusion until the glass-transition temperature,  $T_g$  of the thermoplastic<sup>25,66</sup>. This part of the bonding process is depicted at (3) in figure 2.10. Moreover, this intermolecular diffusion, often indicated as healing, continues when the bead is reheated by newly extruded adjacent filaments above the glass-transition point. Hence, not only the thermal development directly after extrusion, but also during the rest of the fabrication process is relevant for the formation of the bonds between adjacent filaments.

### 2.5.1. Thermal development

Although the importance of thermal development of the printed bead over time is acknowledged, very little effort has been devoted to the investigation of the true temperature profiles of the printed structured for different print settings. Rodriguez et al.<sup>54</sup> have modelled the thermal gradient of a printed bead of the commonly used acrylonitrile-butadiene-styrene material by means of a transient heat transfer analysis. Two different temperature conditions were examined and the results are depicted in the diagram of figure 2.11. For both conditions the temperature rapidly drops below the grass-transition point. The sintering process of the ABS only occurs above 200°C, which is the critical sintering temperature<sup>15</sup>.

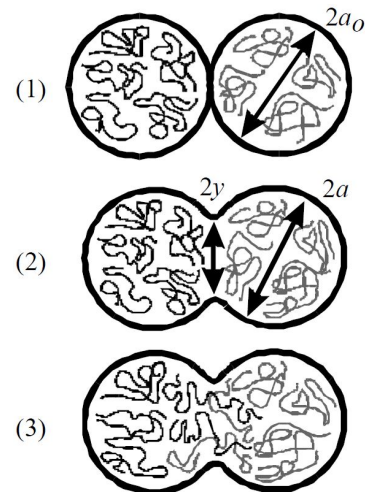
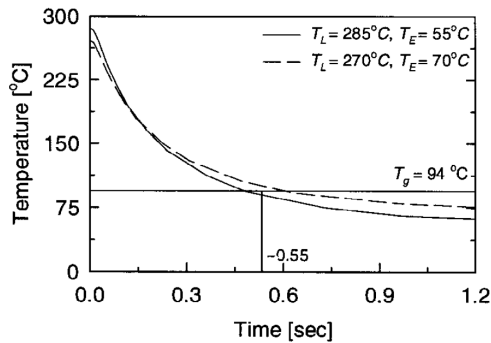
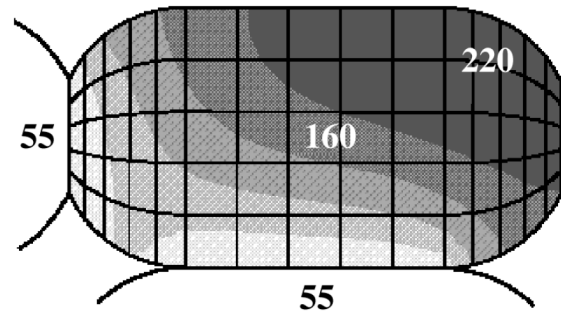


Figure 2.10: The bond formation between two adjacent filaments<sup>66</sup>



**Figure 2.11:** The thermal development at the centre of a single printed bead over time for two different conditions as reported by Rodriguez et al. <sup>54</sup>.



**Figure 2.12:** The thermal gradient within a single printed bead for  $T_L = 285^\circ\text{C}$  and  $T_E = 55^\circ\text{C}$  at approximately 0.18s after extrusion as reported by Rodriguez et al. <sup>54</sup>.

Within the models the adjacent filament are kept at constant temperature, so the actual timespan before reaching  $T_g$  is probably a little longer. Otherwise, the bonding process takes place at the boundaries of the bead, while the graph depicts the thermal development at the centre of the bead and reduce this timespan. Hence, the actual length of the bonding process is unknown, but the graph gives a good indication. Moreover, the thermal development of a single bead is strongly related to material specific properties and thermal history of the bead and its surrounding material. So the figures 2.11 and 2.12 provide a good understanding of the thermal development, but deviates per type of material and printed geometry.

### 2.5.2. Thermal history

The bond formation only occurs within a specific temperature domain and is dependent on the available thermal energy in both the freshly extruded as in the surrounding material. But it also works the other way around. The thermal energy of the printed bead is redistributed via conduction to earlier printed filaments <sup>81</sup>. However, this reheating of adjacent filaments will never lead to complete coalescence and is more pronounced in the vertical than in horizontal direction of the printed structure <sup>24,66</sup>. Therefore, the bottom layers remain at elevated temperatures for a longer time, which results in a more advanced neck-growth compared to the upper layers <sup>35,61</sup>. Even so, a higher geometry will improve the bond quality at the lower part of the print. The difference in gap size between the upper and lower apart are shown in figure 2.13.

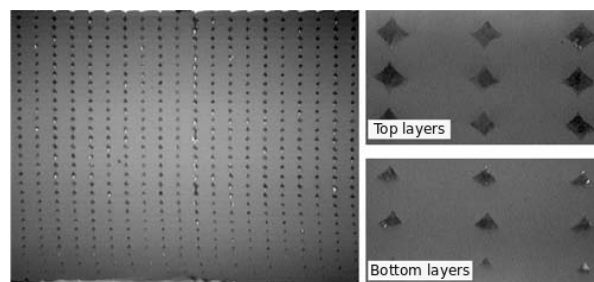


**Figure 2.13:** Different gap sizes within the print. <sup>65</sup>

Concluding, the degree of bonding, and thus the mechanical strength of the additively manufactured product, depends on thermal history of the printed filament <sup>15</sup>. This thermal history is determined by the following process parameters <sup>24,29,37,66</sup>:

- Extrusion temperature,  $T_L$
- Envelope temperature,  $T_E$
- The number of layers above the bond
- Design of the print pattern  
*The length, the shape and the order of the designed pattern*
- Build location  
*The convectonal conditions and variation of temperature within the build envelope*



Sun et al.<sup>66</sup> have printed multiple cuboids out of ABS-material under various print conditions and recorded the temperature of bottom layer during the printing process. Each condition is linked to variation of a single process parameter, so the obtained records indicate the effect of that specific process parameter on thermal history of the bottom layer. These records are shown in the figures below.

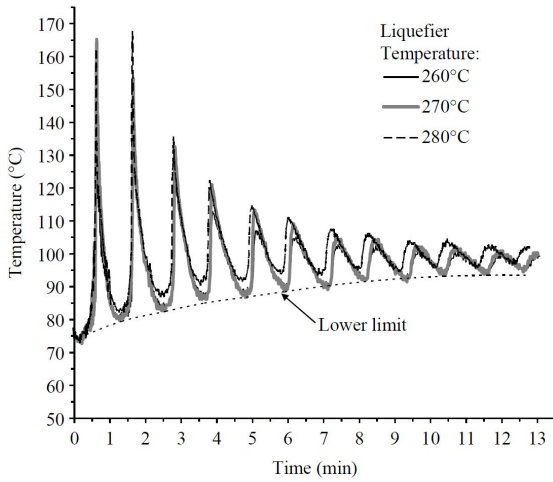


Figure 2.14: The thermal history for three extrusion temperatures<sup>66</sup>.

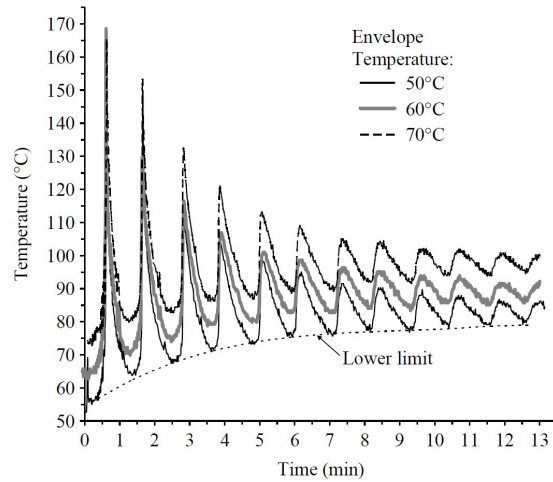


Figure 2.15: The thermal history for three envelope temperatures<sup>66</sup>.

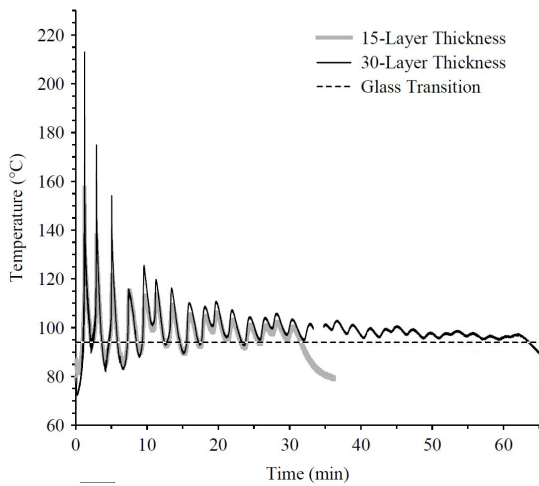


Figure 2.16: The thermal history for two print heights<sup>66</sup>.

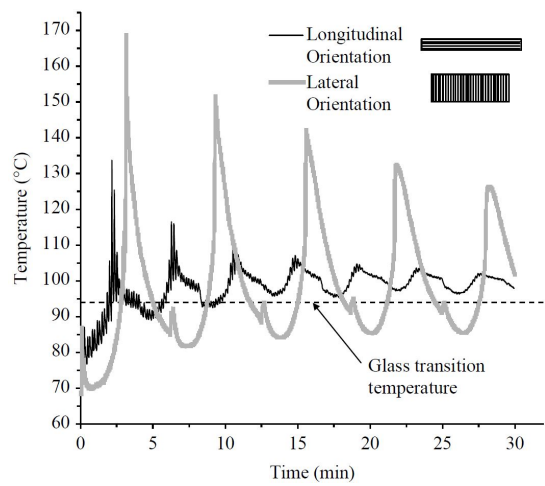


Figure 2.17: The thermal history for two print patterns.<sup>66</sup>

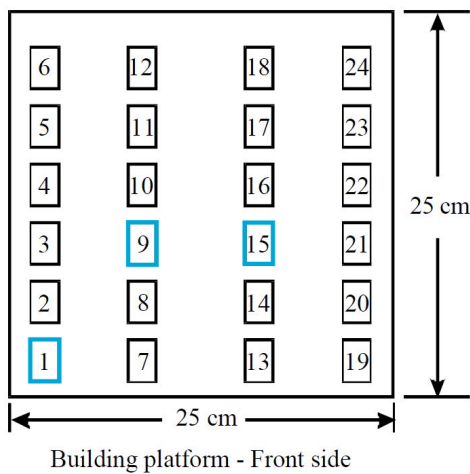


Figure 2.18: The build location of each printed structure<sup>66</sup>.

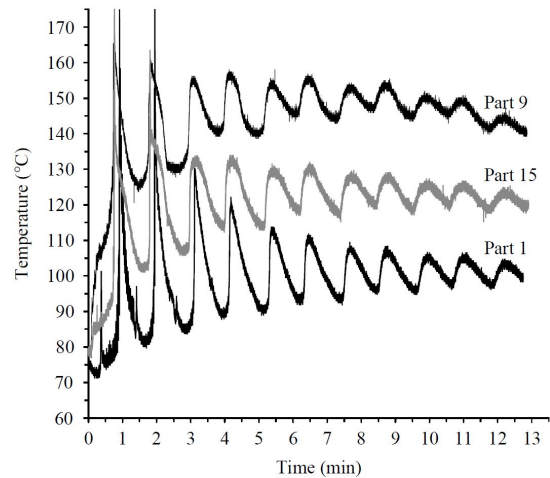
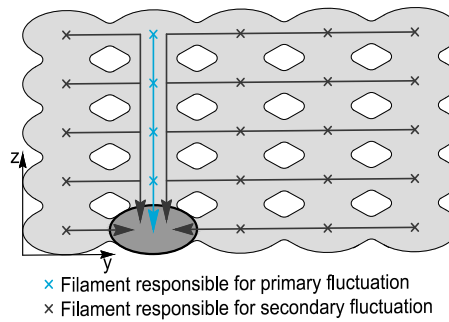


Figure 2.19: The thermal history for three different build locations<sup>66</sup>.

Regarding the process parameters, the thermal history is affected the most by the build location, the



**Figure 2.20:** The extrusion of a filament reheats the material in the layers below.

print pattern and the envelope temperature respectively. The height of the print and the extrusion temperature have little effect on the thermal history.

Independent of the process parameter, the thermal history shows two kinds of fluctuations over the complete operation time of the printer. These fluctuations are caused by the reheating of the bead due to extrusion of the surrounding filaments. As indicated in figure 2.20, the primary fluctuations are caused by conduction of heat from the extruded filament above the bead, while the secondary fluctuation is a consequence of all other filaments across the layers.

## 2.6. Residual stresses

Figure 2.16 confirms the increase in intermolecular diffusion for higher prints. However, more layers do not always result in a stronger structure, because the reheating of the earlier printed layers results in thermal gradients in the vertical direction and along the print path. If these thermal gradients are sufficiently large, the printed structure will warp<sup>78</sup>. Moreover, the reheating cycles within the lamina below the freshly printed layer cause contractions and distortions, which result in non-uniform stresses and strains<sup>35</sup>. Besides an increasing print height, a longer printing pattern increases the thermal gradient as well. Hence, for both process parameters the possible accumulation of stresses at the lower parts of the print<sup>83</sup> have to be considered as they eventually result in delamination, fracture or even collapse of the complete structure<sup>61</sup>.

### 2.6.1. The bond strength

Despite the fact that a lot of research has mentioned the importance of these distortions and accumulated stresses, only a few researches have examined the effects on the mechanical properties of the bond<sup>4,60,62</sup>. All three researches have confirmed the dependability of the bond on its thermal history, but none have documented the numerical results of the fracture test. Moreover, all test specimens were fabricated by means of small scale fused filament fabrication. Hence, the samples are composed of multiple layers and the thermal development is expected to strongly deviate from parts fabricated by the printers of Aectual. Lastly, only the interlayer bonding was examined, but for the geometries designed by DUS, Architects the intralayer bonding is significantly more relevant. As can be seen in the figures on the next page, most of the products can be schematised as single layered planes, which are connected by means of an intralayer bond. All loads acting on the structure are transferred towards the supports via these intralayer bonds, so failure of these bonds will reduce the strength and the stiffness of the macrostructure significantly. Thomas and Rodríguez<sup>68</sup> have even indicated that a double layered print enhances the interlayer bonding strength.

## 2.7. The capacity of an additively manufactured structure

Based on the available literature and the examination of the most commonly printed products by Aectual, the intralayer bond is assumed to be the weakest link within the structure. Hence, a better understanding of the mechanical behaviour of these bonds and dependability on the print process parameters is required to evaluate the structural behaviour of the extrusion-based additively manufactured products on macro scale.



Figure 2.21: Front view of a full-print façade designed by DUS. Architects and produced by Aectual



Figure 2.22: Close-up of the full-print façade.



Figure 2.23: Close-up of a joint of the full-print façade. The intralayer bonds within the joint are clearly visible.

# 3

## Test description

Over the past years Aectual and DUS. Architects have designed various mixture of polymers used for additive manufacturing. By means of tweaking settings of the printers and the compositions of the mixture the people of Aectual attempt to optimise the prints. This optimisation process is mainly based on the aesthetics of the printed products. Each test sample is evaluated on the following aspects:

### **The corners of the print**

The sharpness of the corners depends on the adhesion of the freshly printed bead with the previous layers. When the adhesion is not sufficient, the nozzle can drag the printed material along increasing the corner radius. It is possible that the corner radius varies per layer.

### **The angle over the height**

The filaments can be stacked on top of each other with a maximum angle of 45° from vertical axis. If this angle is increased, less than half of the bead is support by the printed layers underneath it, which is likely to cause instability. The bonding is evaluated by means of printing straight and curved surfaces under a 45 degree angle.

### **Large and small curvatures**

Similar to the corners, bad adhesion of bead to its supports causes the nozzle drag the filament along changing the geometry from the intended design.

### **The straight lines**

With the evaluation of straight lines the supply of extruded material can be reviewed. If the flow rate is adequate, smooth lines with evenly distributed material along its print path will be printed. When the flow rate is too low, the filament can not provide sufficient support to the next layer print and it is not likely that the print can be finished. An excess amount of extruded material on the contrary won't provide smooth lines and may cause jamming of the printer head.

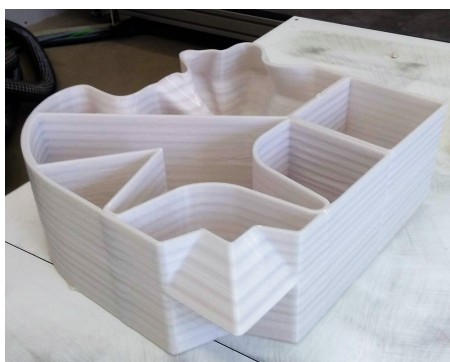


**Figure 3.1:** Test sample to assess the print quality



**Figure 3.2:** The curved surface of the test sample

**The adhesion of filaments in double layered prints**

The adhesion is monitored during the printing process. When the print is finished, the rate of bonding between the filaments is only judged by inspecting the outside of the print. The samples are not cut for further evaluation of the bonding between filaments.

**The distribution of material along curved paths for double layered prints**

Especially for double layered prints, inadequate bonding of the printed bead with the support underneath will cause variation in distribution of printed material along the print path (e.g. the second printed filament can be pulled over the neighbouring filament in the same layer).

**The bonding in small and large joints**

The judgement of bonding in connections is similar to the evaluation of the corners. The adhesion must be sufficient to prevent breaking up the freshly printed bead from neighbouring material in the joints. Within large joints evenly distributed amount of material along the printed trajectory must be available to assure adequate bonding.

**The resemblance of the whole print with the design**

Afterwards the prints are judged on their overall appearance which includes discolouration, degradation and other possible deviations in the prints.

Although the prints and the printing process are examined thoroughly, assessment of the prints on its appearance and print quality is not enough for the evaluation of the designed materials. To determine whether a new mixture of polymers is better for the building industry than the previous compositions, the printed material has to be evaluated on its strength, stiffness and the resistance to environmental conditions with extreme exposures. As is demonstrated by Bui<sup>19</sup>, the properties of the raw materials in the mixture do not assure similar behaviour of the melt extruded material. So for structural purpose, the development of new polymer mixture as print material must be evaluated on its own mechanical properties.

### 3.1. Expected material behaviour

Despite the history of Additive Manufacturing, still no specific standards have been designed for the usage of polymers fabricated by Fused Filament Fabrication or Melt Extrusion in the building industry. Consequently, the design of the tests have to be compared to test set-ups prescribed by the international standards for materials of comparable compositions and behaviour.

#### 3.1.1. Comparable materials

Since the material fabricated by Melt Extrusion Methods have a laminated structure, it can be compared to structures of Fibre Reinforced Composite. Within a Fibre Reinforced Composites fibres are positioned in a matrix. This matrix is a polymer resin which fixes the fibres in a desired geometry. Glass, carbon and aramid fibres are the most commonly used fibres within the building industry. The stiffness and strength of the resin are normally ten times lower than those of the fibres<sup>50</sup>. The resin only transfers the forces to and between the fibres. Due to the relative weak resin failure of the composite is likely to occur between the fibres instead of failure of the fibres itself.

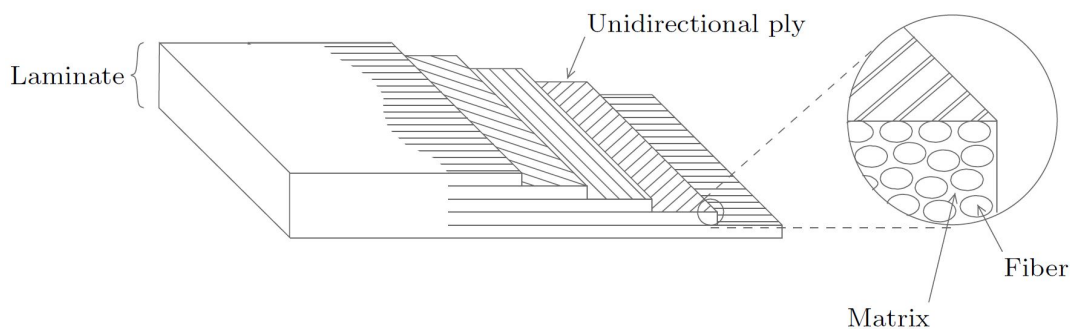


Figure 3.3: The structure of a fibre reinforce composite<sup>73</sup>.

As can be seen in figure 3.3 each layer is unidirectional, which means that all fibres in this so-called ply have the same orientation. This is similar to a printed layer within the Additively Manufactured products. The printed roads represent the fibres and the bonding between these filament can be considered as the resin. As elaborated in the previous chapter, the cohesion between adjacent filaments is often the weakest and most critical link in 3D-printed product.

### 3.1.2. Type of Composite

As the Extrusion Deposited products are similar to Fibre Reinforce Composites, the standards relevant for FRP can be used for the assessment of the mechanical properties of 3D-printed objects as well. Various standards are available, but not all can be used. To take into account the most common designs of DUS. Architect, it can be stated that the 3D-products have an unidirectional structure. Since the designs are often constructed out of sections with not more than two adjacent filaments within one layer, the orientation of the layers does not vary over the height. Hence, the products designed by DUS. Architects and fabricated by Aectual can be regarded as unidirectional composites.

Based on these conclusions, relevant standards as described by either the American Society for Testing Materials International (ASTM) or the International Organisation for Standardisation (ISO) will be consulted for each type of material test. The more the designed test are in accordance to the relevant standard, the more accurate the obtained mechanical properties are considered.

## 3.2. Tensile Strength

With the axial tensile test general information about the mechanical properties of the printed material, which can be compared to the materials examined in the previous researches of [Baran](#), [Wang](#) and [Bui](#). The relevant standards are listed below. Preferably the test method as prescribed by the

<b>ASTM D638-14</b>	Standard Test Method for Tensile Properties of Plastics <sup>8</sup>
<b>ASTM D3039/D3039M-17</b>	Standard Test Method for Tensile Properties of Polymer Matrix Composite Materials <sup>11</sup>
<b>NEN-EN-ISO 527-1</b>	Plastics - Determination of Tensile Properties - Part 1: General principles <sup>48</sup>
<b>NEN-EN-ISO 527-4</b>	Plastics - Determination of Tensile Properties - Part 4: Test conditions for isotropic and orthotropic fibre-reinforced plastic composites <sup>42</sup>
<b>NEN-EN-ISO 527-5</b>	Plastics - Determination of Tensile Properties - Part 5: Test conditions for unidirectional fibre-reinforced plastic composites <sup>46</sup>

standards ASTM D3039/D3039M-17 and NEN-EN-ISO 527-5 is used. Both standards prescribe the application of tabs at both end of the test specimen for testing unidirectional materials to failure in the fibre direction. These tabs are bonded to the specimens with a high-stretch adhesive to assure failure at a location between the tabs.

Unfortunately, the 3D printed materials fabricated by Aectual are unsuited for the application of adhesives. Since the tabs require to be strong than the material of interest, the tabs can not be printed either. Both standards mention the use of specimens without end tabs is permitted, when an acceptable failure modes occur with reasonable frequency. Concerning the cross-section of the prints, the edges which are clamped by the grips are ribbed. Adequate grip is doubted when the specimen have the same cross-section over the whole length of the specimen. Consequently, the consistency in result tensile tests is not be assured, which questions the validity of the test.

Moreover, it is reasonable that peak stresses are introduced at location of the grips due to the ribbed surface of the specimens. Therefore, guidance of the failure mechanism is desirable. The remaining standard prescribe a so-called dog-bone tensile specimen, which contains a narrow section in the middle and a wider section at both ends, the shoulders. The transition of the narrow section towards shoulders is accommodated by fillets of a certain radius, this is illustrated in figure 3.4.

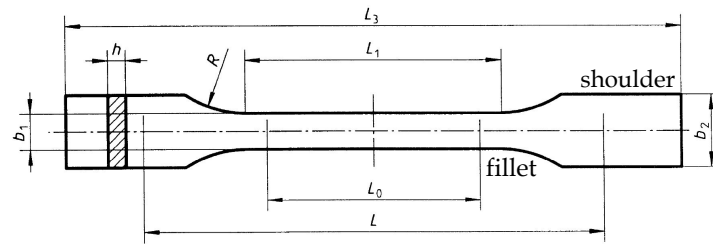


Figure 3.4: Specimen as prescribed by ISO527-4<sup>42</sup>.

### 3.2.1. Dimensions of the tensile specimen

The dimensions of the tensile specimen are identical to the specimens tested by Wang<sup>77</sup>. The test specimens are placed in the testing machine Zwick Z010 where both shoulder are fixated in grips. The lower grip is located while the upper grip moves upward with a constant strain rate of 10mm/min until failure of the specimen. Due to the unequal surface of the specimens the application of extensometers is difficult and the reliability of the measurement of the extensometers is doubted. Hence extensometers are excluded from the tensile test. Table 3.1 provides an overview of the specification of the tensile tests.

Table 3.1: Specifications for the tensile test

Tensile test	
<b>Test setup</b>	
<b>Geometry</b>	
<b>Specimen type</b>	Single layered Double layered
<b>Equipement</b>	ZwickZ 010
<b>Testing speed</b>	10 mm/min
<b>Test environment</b>	$(20 \pm 2)^\circ\text{C}$ , $(50 \pm 10)\% \text{ RH}$
<b>Output</b>	Axial force $P$ [N] Nominal displacement between the grips $u$ [mm]

## 3.3. Flexural Strength

The flexural properties of a material are obtained by means of bending tests. This is either a four-point or a three-point loading test. The latter is more suitable for materials that do not rupture or yield within the 5.0% strain limit<sup>12</sup>. For the determination of the flexural properties four standards are considered.

<b>ASTM D790-17</b>	Standard Test Methods for Flexural Properties of Unreinforced and Reinforced Plastics and Electrical Insulating Materials <sup>12</sup>
<b>ASTM D7264/D7264M-15</b>	Standard Test Method for Flexural Properties of Polymer Matrix Composite Materials <sup>10</sup>
<b>NEN-EN-ISO 178</b>	Plastics - Determination of flexural properties <sup>47</sup>
<b>NEN-EN-ISO 14125</b>	Fibre-reinforced plastic composites - Determination of flexural properties <sup>43</sup>

The applicability of NEN-EN-ISO 14125 is questionable, because the standards explicitly states "unreinforced and particle-filled plastics and plastics reinforced with short (i.e. less than 1 mm length) fibres are covered by ISO 178". The length of the glass fibres in the products of Aectual is not defined, but there are already in the propylene pellets. Concerning the analogy between the structure of a 3D-printed object and a fibre reinforced polymer structure, the standard may still be relevant. Still, extensive use of the standard in the design of the test setup is avoided.

Based on previous reports a three-point loading test (Method A) is assumed to be sufficient to determine the flexural properties of the additively manufactured material. The use of extensometer is not necessary, because the deflection at the midspan is recorded by the testing apparatus as the cross head movement of the loading nose (Type I). The loading nose is carried by the moving member and has a radius of 5mm. The support noses have the same radii and are part of the fixed member upon which the test specimen is placed.

### 3.3.1. Dimensions of the flexural specimen

According to the standards, a span-to-thickness of at least 16:1 is required. For the single and double layered specimens this results in a span length of at least 85mm and 165mm respectively. But the standard prescribe that results of the flexural test may not be compared with data obtain from a setup with a different support span-to-thickness ratios<sup>10</sup>. Since both Baran<sup>13</sup> and Wang<sup>77</sup> have used a span length of 115mm and the thickness of the samples have not changed, the span length of 115mm is adopted in this research. Similarly and in accordance with NEN-EN-ISO 14125, the other settings have been embraced as well resulting in a width of 50mm and a testing speed of 10mm/min.

**Table 3.2:** Specifications for the flexural test

Flexural test	
<b>Test setup</b>	
<b>Geometry</b>	
<b>Specimen type</b>	Single layered Double layered
<b>Equipement</b>	ZwickZ 010
<b>Testing speed</b>	10 mm/min
<b>Test environment</b>	$(20 \pm 2)^{\circ}\text{C}$ , $(50 \pm 10)\% \text{RH}$
<b>Output</b>	Applied force at midspan $P$ [N] Deflection at mid-span $\delta$ [mm]



### 3.4. Interlaminar Fracture Toughness

The interlaminar fracture toughness of a material is equal to its resistance against (the propagation of) cracks. As reported by various researchers, the bonding between printed filaments is the weakest link within the mesostructure of Additively Manufactured products<sup>16,18,28,56</sup>. Therefore, the interlaminar fracture toughness for additively manufactured materials is associated with failure of the bonding between the printed filaments, also indicated as delamination. This type of failure is examined extensively within the study of Fracture Mechanics. Within this expertise three failure mechanisms are distinguished: Mode I, II and III. Each mode corresponds to a stress in a specific direction, which is depicted in figure 3.5 for each specific failure mode.

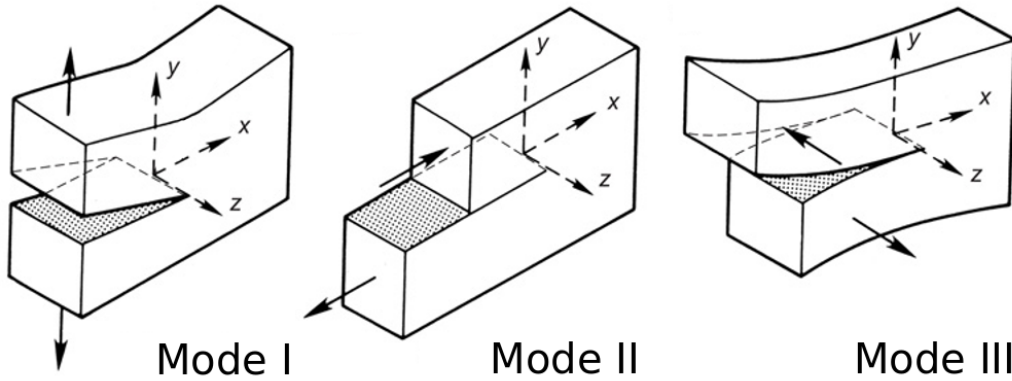


Figure 3.5: Three fracture modes (after Kanninen and Popelar<sup>33</sup>).

The first mode is the opening mode, which is a result of a critical tensile stress perpendicular to the interface. The second mode is indicated as the sliding mode and the third mode is the tearing mode. Both modes are a result of critical shear stresses acting parallel to the crack. In mode II these shear stresses act in direct of the printed filaments, whilst the stresses in mode III are directed perpendicularly to the printed filament.

#### 3.4.1. The principles of Fracture Mechanics

The purpose of Fracture mechanics is to determine the maximum of load an structure prone to cracking can resist in order to predict and control the crack development. Besides the orientation and duration of the load, the cracks present prior to loading affects the resistance against fracture<sup>82</sup>. The crack growth prediction is based on the energy balance of the material. For the propagation of a crack, a sufficient amount of energy must be available at the crack tip. This is provided by potential energy,  $\Pi$ , which is a function of the total strain energy,  $\Omega$ , and the work done by external loads on the structure,  $U$ . Strain energy is stored in the bonds between the atoms of the material. When a structure undergoes a deformation, the inter-atomic distance increases and energy is stored. When the amount of energy available exceeds the atomic bond strength, the bonds break and the stored energy is released. This released energy is transformed in surface, dissipative and kinetic energy<sup>59</sup>. The transition to surface energy will result in new free surface, i.e. fracture. In short, until fracture all work done by the external loads on the body are transformed into strain energy. When a crack arise or propagates, this strain energy stored in the adjacent material is released and the material is unloaded. The release of energy due to fracture is illustrated in figure 3.6 for Mode I failure.

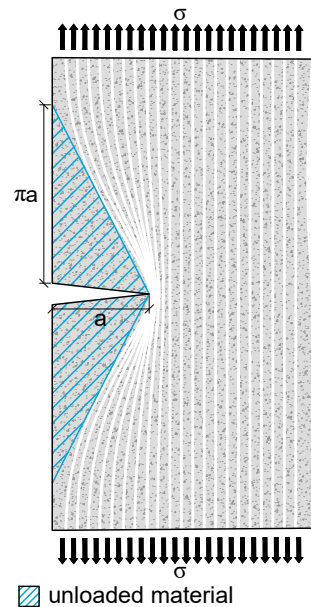


Figure 3.6: Unloading due to fracture (after Roylance<sup>57</sup>).

$$\begin{aligned}
 G \cdot dA &= -d\Pi \\
 G \cdot dA &= -d(\Omega - U) \\
 G &= -\frac{\partial}{\partial A} \left[ \Omega - U \right] \quad (3.1)
 \end{aligned}$$

The parameter  $G$  in equation (3.1) is the so-called Strain Energy Release Rate (SERR) and indicates the interlaminar fracture toughness of the material. This is equal to the amount of energy dissipated by crack propagation per unit newly formed crack area,  $dA$ , and is expressed in joule per squared meter ( $\text{J m}^{-2}$ ). Note that the projected crack area,  $A$ , is equal to the integral of width over the crack length, while the crack surface,  $s$ , is twice this term<sup>76</sup>. As elaborated by Zehnder<sup>82</sup>, the work of external loads on a solid body can be expressed as an function of tractions,  $\vec{t}$ , on its surfaces, body forces,  $\vec{b}$ , and their corresponding local displacements,  $\vec{u}$ . However, for the examination of the interlaminar fracture toughness, any load applied to the structure can be represented by a individual generalised load,  $P$ , and a corresponding displacement,  $q$ . In this report the latter will be used for the establishment of the interlaminar fracture toughness related to the Melt Extrusion Manufactured material.

$$G = -\frac{\partial}{\partial A} \left[ \Omega - \left( \int_{\Gamma_t} \vec{t} \cdot \vec{u} \, d\Gamma + \int_V \vec{b} \cdot \vec{u} \, dV \right) \right] \quad (3.2)$$

$$G = -\frac{\partial}{\partial A} \left[ \Omega - P \cdot q \right] \quad (3.3)$$

As earlier indicated, the released energy during snapping of the atomic bonds is not solely converted in surface energy. Energy is also dissipated due to other mechanism like microcracking, phase transformation and plastic deformation<sup>26</sup>. The ratio between energy dissipation due to surface generation and other dissipative mechanisms is an indication for the brittleness of the material. A fracture is considered brittle, when the energy is mainly converted into surface energy. But when a significant amount of the energy is also transformed in dissipated energy and kinetic energy, the material is ductile.

### 3.4.2. Load-displacement records

Since the fundamentals of fracture mechanics has been explained, the next section will focus on the estimation the interlaminar fracture toughness from experiments. The energy balance as described by (3.1) can be linked to load-displacement diagram for a structure and relevant test setups. A distinction can be made between prescribed displacement and the fixed load approach. The former method records the change in load as a consequence of the displacement increment, while the latter prescribes a fixed load step and the measurement of the corresponding displacement. Both methods provide a load-displacement diagram which is useful for the determination of the resistance against fracture. Figure 3.7 depicts a possible load-displacement diagram of a body made from solid material with a crack area  $A_0$ . The area underneath the curve, indicated by the gray shaded area, is equal to the stored elastic strain energy,  $\Omega$ .

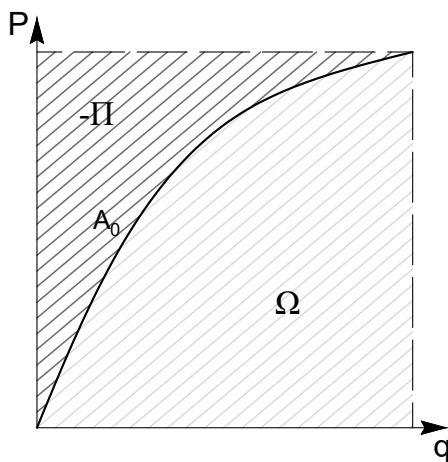


Figure 3.7: Load-displacement diagram for a solid body with crack area  $A_0$ .

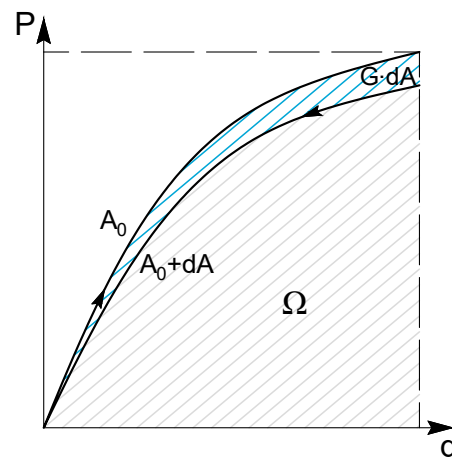


Figure 3.8: Load-displacement diagram for a solid body with an increased crack area  $A + dA$ .

When the maximum capacity of elastic strain energy has been reached, the stored energy is released and the crack propagates. Consequently, the resistance of the body against deformation is affected

and the load-displacement curve is altered. The difference between the work done,  $P \cdot q$ , and the remaining strain energy recovered upon unloading after crack growth,  $\Omega$ , is equal to the energy release rate,  $G$ , multiplied with the newly developed crack area  $dA$ . This dissipated energy is indicated by the blue shaded area in figure 3.8.

So, the elastic strain energy is a function of the fracture area and on either the applied load or the induced displacement, which is related to prescribed load or displacement approach respectively. The increment of elastic strain energy  $\Omega(q, A)$  can be written as:

$$d\Omega = \frac{\partial \Omega}{\partial q} \cdot dq + \frac{\partial \Omega}{\partial A} \cdot dA \quad (3.4)$$

Before fracture there is no crack growth, so each increment in displacement or load is solely converted to strain energy. As indicated in the figure this elastic strain energy before crack propagation is equal to the area underneath the load-displacement curve. This results in the following expression of the external load  $P$ .

$$\begin{aligned} G \cdot dA &= -d(\Omega - U) \\ G \cdot dA &= -\left(\frac{\partial \Omega}{\partial q} \cdot dq + \frac{\partial \Omega}{\partial A} \cdot dA\right) + P \cdot dq \\ 0 &= -\frac{\partial \Omega}{\partial q} dq + P \cdot dq \\ P &= \frac{\partial \Omega}{\partial q} \end{aligned} \quad \left. \begin{array}{l} \\ \\ \\ \end{array} \right\} dA = 0 \quad (3.5)$$

During crack growth the displacement doesn't change, but the reduction of the stiffness of the material results in a load drop. Both the external work and the first term of the increment of elastic strain energy are equal to zero, which result in the following expression.

$$\begin{aligned} G \cdot dA &= -d(\Omega - U) \\ G \cdot dA &= -\left(\frac{\partial \Omega}{\partial q} \cdot dq + \frac{\partial \Omega}{\partial A} \cdot dA\right) + P \cdot dq \\ G &= -\frac{\partial \Omega}{\partial A} \end{aligned} \quad \left. \begin{array}{l} \\ \\ \end{array} \right\} dq = 0 \quad (3.6)$$

In figure 3.9 an domain  $dq$  is indicated. Within this domain the increase of the term  $G \cdot dA$  is equal to the difference in strain energy before and after the load drop. For a specific displacement the difference between the corresponding loads before and after crack is only affected by the magnitude of the fracture. Hence, the load drop is defined by the partial derivative of the load with respect to the crack area multiplied with the newly formed crack area. The displacement increment  $dq$  is infinitely small, so the grey shaded area is regarded as a rectangular shape with dimensions equal to the load drop and the displacement increment. It represents the difference between the dissipated energy corresponding to crack growth at displacement  $q$  and  $q + dq$ . Equating the definitions of this area integrating them with respect to the displacement  $q$ , provides a new definition for the strain energy release rate that can be obtain from the load-displacement recordings.

$$\begin{aligned} G(q + dq, A) dA - G(q, A) dA &= (P(q, A) - P(q, A + dA)) dq \\ \left(\frac{G(q + dq, A) - G(q, A)}{dq} dq\right) dA &= \left(\frac{P(q, A) - P(q, A + dA)}{dA} dA\right) dq \\ \frac{\partial G}{\partial q} dA dq &= -\frac{\partial P}{\partial A} dA dq \\ G &= -\int_0^q \frac{\partial P}{\partial A} dq \end{aligned} \quad (3.7)$$

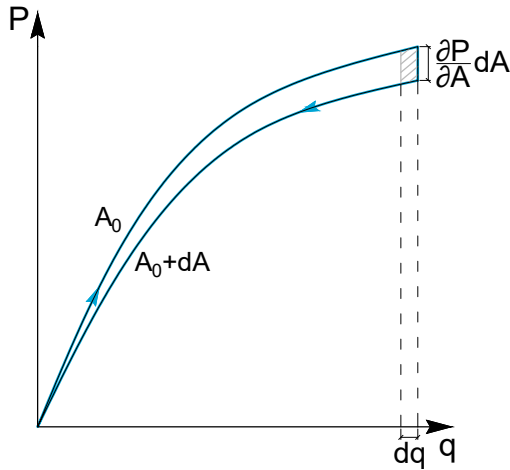


Figure 3.9: Evaluation of the energy balance on an infinite small domain  $dq$ .

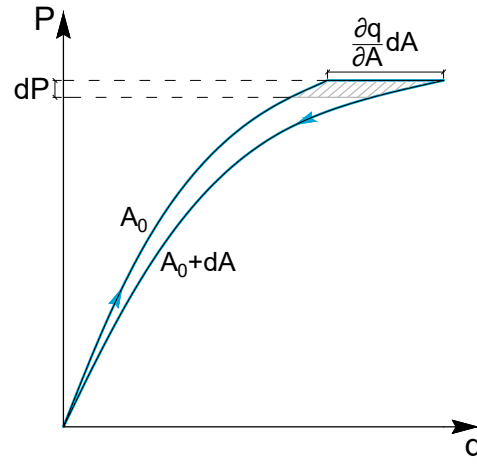


Figure 3.10: Evaluation of the energy balance on an infinite small domain  $dP$ .

Similarly, the expression of  $G$  for the fixed load approach can be estimated. Whilst the prescribed displacement method involves a load drop, crack growth in the fixed load approach results in a increase of displacement under a constant load. An infinite small domain  $dP$  is regarded and the difference between the dissipated energy corresponding to crack growth at load  $P$  and  $P + dP$  is equal to the increment of the displacement times the load domain, see figure 3.10.

$$\begin{aligned}
 G(P + dP, A) dA - G(P, A) dA &= (q(P, A + dA) - q(P, A)) dP \\
 \frac{\partial G}{\partial P} dA dP &= \frac{\partial q}{\partial A} dA dP \\
 G &= \int_0^P \frac{\partial q}{\partial A} dP \quad (3.8)
 \end{aligned}$$

### 3.4.3. The compliance method

The derivation of the strain energy release rate provides a better understanding of the inter laminar fracture toughness and is suitable for testing both linear as non-linear materials, but to obtain the derivatives with respect to fracture area a set of samples with a varying crack length must be tested. Consequently, a good estimation of  $G$  is only established, when all samples have identical mechanical properties<sup>82</sup>. Based on previous test and the recent developments in printed quality of the 3D-printers at Aectual, this requirement is not fulfilled and this so-called multiple specimen method is not useful.

Fortunately, the printed material is regarded as linearly elastic and the determination of interlaminar fracture toughness can be simplified by the use of the Compliance Method. In this method multiple test are executed for various crack lengths on a single test sample. Each test provides a compliance related to a particular crack length for that tested sample. The compliance,  $C$ , is inversely proportional to the slope of the load-displacement curve. For linearly elasticity materials the relationship between the load and the displacement is linear, which results in the following expressions of the compliance and elastic strain energy:

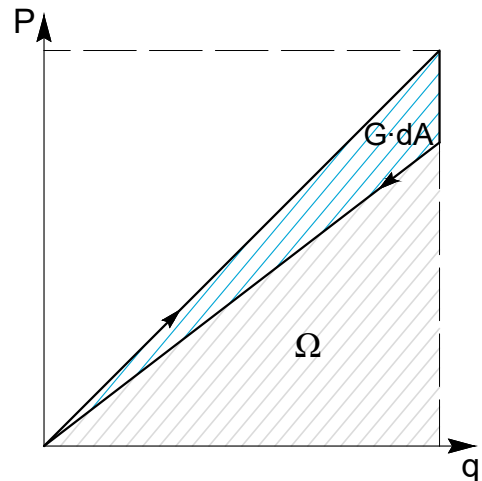


Figure 3.11: Load displacement diagram of a linear elastic material.

$$C = \frac{q}{P} \quad (3.9)$$

$$\Omega = \frac{1}{2} Pq \quad (3.10)$$

Subsequently, the definitions for  $G$  is converted into a function of the compliance. Remember that the displacement is predefined in expression (3.7) and therefore independent of the crack area. On the contrary, the compliance for a linearly elastic material is constant and only is affected by crack growth, because a bigger crack alters the slope of the force-displacement diagram, i.e. the stiffness of the material.

$$\begin{aligned}
 G &= - \int_0^q \frac{\partial}{\partial s} \left( \frac{q}{C} \right) dq \\
 &= \int_0^q \frac{q}{C^2} \frac{\partial C}{\partial A} dq \\
 G &= \frac{1}{2} \frac{q^2}{C^2} \frac{\partial C}{\partial A}
 \end{aligned}
 \left. \vphantom{\int_0^q} \right) \frac{d}{dx} \left( \frac{1}{f(x)} \right) = - \frac{1}{f^2(x)} \frac{df(x)}{dx}
 \tag{3.11}$$

Definition (3.8) is related to a load controlled approach, hence the displacement and crack growth are a consequence of load increment.

$$\begin{aligned}
 G &= \int_0^P \frac{\partial}{\partial A} (P \cdot C) dP \\
 &= \int_0^P P \frac{\partial C}{\partial A} dq \\
 G &= \frac{1}{2} P^2 \frac{\partial C}{\partial A}
 \end{aligned}
 \tag{3.12}$$

Given the definition of the compliance for linearly elastic material is evident that expressions of SERR for the load and displacement control are identical. Lastly, within the fracture mechanics it is assumed when the work done by the external load and/or displacement has reached the maximum capacity of stored strain energy, all bonds at crack tip along the width of the specimen break simultaneously<sup>59</sup>. Because the specimens used for the determination of interlaminar fracture resistance have an uniform width,  $w$ , along the length. If the crack develops as depicted in figure 3.6, the fracture area,  $A$  is equal to  $w \cdot a$ .

$$G = \frac{1}{2} \frac{P^2}{w} \frac{\partial C}{\partial a}
 \tag{3.13}$$

### 3.4.4. Testing methods

As the experiments of Hill and Haghi<sup>30</sup> have shown, the bonding between two printed filaments are more prone to shear and tension than the filaments itself. Therefore, all three failure modes are of relevance. The ASTM and ISO prescribed various testing methods for the determination of the interlaminar fracture toughness, but none related to the third failure mode. The two most reviewed test setups for the evaluation of the failure mechanism are depicted in figures 3.12 and 3.13. Both test methods require complex test setups and the achieved relationship between the crack length and  $G_{IIIc}$  are incompatible<sup>67</sup>. Furthermore, research has indicated that the distribution of released energy during fracture development along a straight crack front during crack propagation is non uniform making it difficult to monitor the crack growth. This complicates the determination of the energy release rate<sup>39,53</sup>. Based on the exploratory researches it is concluded that the attainment of pure Mode III delamination is challenging. Consequently, additional validation of these testing methods is required before an acceptable standard can be designed.

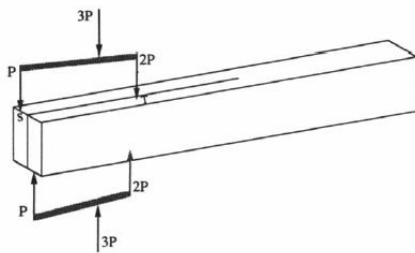


Figure 3.12: Modified split-cantiliver beam (MSCB) specimen designed for the determination of  $G_{IIIc}$ <sup>53</sup>.

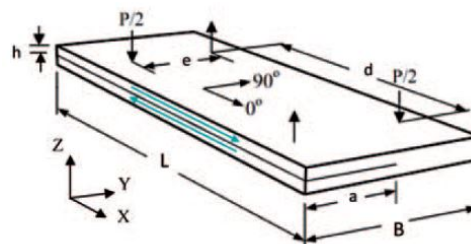


Figure 3.13: Edge-crack torsion (ECT) specimen designed for the determination of  $G_{IIIc}$ <sup>39</sup>.

This research tends to establish a reliable judgement on the relevance of interlaminar fracture for the design of additively manufactured geometries, it is favourable to reduce the unpredictability of test methods to a minimum. Hence, only the test methods as described by the international standards of ASTM and ISO are considered.

#### Mode I

##### ASTM D5528-13

Standard test method for Mode I interlaminar fracture toughness of unidirectional fibre-reinforced polymer matrix composites<sup>6</sup>

##### NEN-ISO 15024

Fibre-reinforced plastic composites - Determination of mode I interlaminar fracture toughness,  $G_{Ic}$ , for unidirectionally reinforced materials<sup>44</sup>

#### Mode II

##### ASTM D7905/7905M-14

Standard test method for determination of the Mode II interlaminar fracture toughness of unidirectional fibre-reinforced polymer matrix composites<sup>9</sup>

##### NEN-ISO 15114

Fibre-reinforced plastic composites - Determination of the Mode II fracture resistance for unidirectionally reinforced materials using the calibrated end-loaded split (C-ELS) test and an effective crack length approach<sup>49</sup>

#### Mixed Mode I-II

##### ASTM D6671/D6671M-13<sup>e1</sup>

Standard test method for mixed Mode I-Mode II interlaminar fracture toughness of unidirectional fibre reinforced polymer matrix composites<sup>7</sup>

#### Mode I Fatigue

##### ASTM D6115-87

Standard test method for Mode I Fatigue delamination growth onset of unidirectional fiber-reinforced polymer matrix composites<sup>5</sup>

Even though delamination is often caused by a combination of several modes, the mixed failure modes are too complex for this exploratory research into the resistance of melt extrusion manufactured material against delamination. Hence, only the standards for the individual failure modes are examined. Moreover, the Mode I Fatigue standard is excluded from examination as well, since it is more reasonable to determine the fracture resistance due to the increase of displacement or load up to failure before examination of delamination due to cyclic loading.

The remaining standards identify three different test specimens. The test method prescribed for the opening mode is identical in both standards, but requires the measurement of the location of the crack front with an accuracy of  $\pm 0.5\text{mm}$ . This requires advanced equipment and reduces the feasibility of the test. In addition to this restriction, the specimen is loaded perpendicular to the crack surface by the use of load blocks or piano hinges. As depicted in figure 3.14, these elements are attached to the specimen with adhesive to achieve a uniformly distributed load. As explained before, the use of adhesives is unfavourable, because the reliability of the test result is questionable.

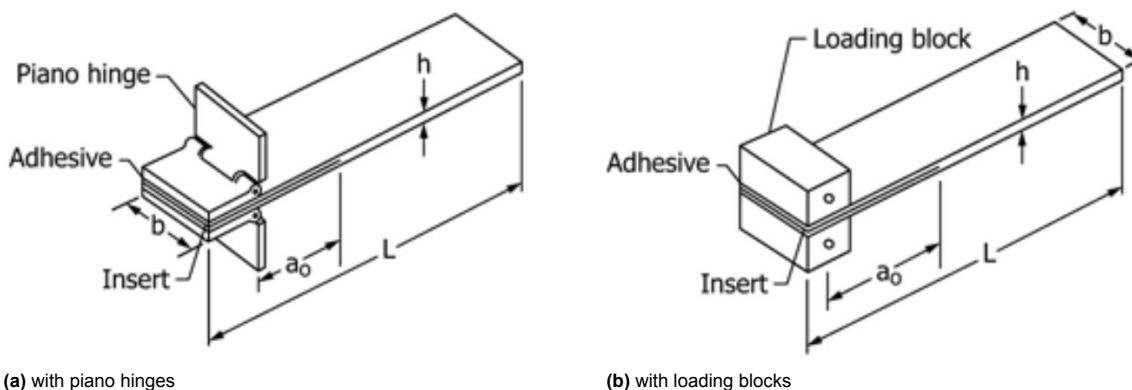


Figure 3.14: Double cantilever beam (DCB) specimen designed for the determination of  $G_{Ic}$ <sup>6</sup>.

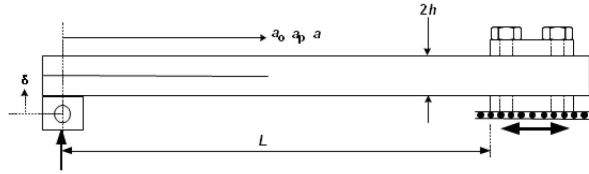


Figure 3.15: End-loaded split (ELS) specimen designed for the determination of  $G_{IIc}$ <sup>49</sup>.

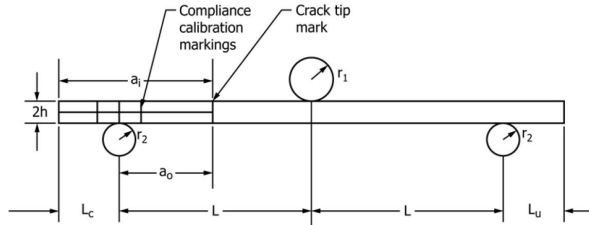


Figure 3.16: End notched flexure (ENF) specimen designed for the determination of  $G_{IIc}$ <sup>9</sup>.

The test setup of Mode II in accordance to the ASTM requires an end notched flexure specimen, while the method of ISO tests an end-loaded split specimen. The geometry of both samples is quite similar, it is mainly the application of the loads on and the fixation of the specimens that varies. Both methods rely on the compliance method and the failure mode is initiated by means of shear stresses due to bending. However, the ELS specimen is directly loaded until failure and an ENF specimen is tested multiple times for various crack lengths to determine the compliance for each crack length. The latter favours the test method as defined by the ASTM, because the crack length doesn't require detailed records of the development of the crack width during the test. Moreover, the ELS requires a loading block attached by means of an adhesive, which is regarded as undesirable.

Reviewing all four options, the ASTM standard test method for determination of the Mode II interlaminar fracture toughness<sup>9</sup> is the most practical. Although this test method is more time demanding, the set-up is simple and does not require accurate measurement of the crack length during testing or adhesives. Hence, it is expected to obtain the most reliable results for the evaluation of the resistance of the melt extruded material against delamination.

### 3.4.5. Test setup

According to the ASTM Standard, the characterisation of Interlaminar Mode II Fracture requires an End Notched Flexure Specimen (ENF) as depicted in 3.16. This design of the specimen is supposed to have a rectangular shape with a uniform thickness and width along its length. The ENF Specimen contains a pre-implanted insert and is subjected to a three point-bending test.

As specified by Davidson and Sun<sup>22</sup>, the most accurate determination of Mode II is achieved by means of a compliance method. A single specimen is tested thrice for various crack lengths. The first two tests are non-destructive, while in the third test the specimen is loaded until failure. The length of the insert for each test is 20mm, 40mm and 30mm respectively. All three tests are displacement controlled and in the non-destructive tests the specimen is subjected until a specific load, which is based on either  $G_{IIc}$ -values of comparable material or an exploratory test. Since no relevant researches are available, the latter is required. In this test the crack front of the sample is placed at 30mm from the crack front and is tested destructively. When the tested specimen fails due to delamination, the load at break,  $P_c$ , and crack length,  $a$ , provide a first estimation of the  $G_{IIc}$ .

$$G_{IIc} = \frac{P_c^2 \cdot 9a^2}{16w^2 \cdot E_{If} \cdot h^3} \quad (3.14)$$

To assure non-destructive testing the peak force or load limit,  $P_j$ , is set to be 50% of the expected maximum load corresponding to each crack length. The maximum load for each crack length is calculated with expression (3.15), which includes the earlier estimated value of  $G_{IIc}$ . The index  $j$  is either 0, 1 or 2 and is related to test setup with a crack length of 30mm, 20mm and 40mm respectively.

$$P_{c,j} = \frac{4w}{3a_j} \cdot \sqrt{G_{IIc} \cdot E_{If} \cdot h^3} \quad (3.15)$$

$$P_j = \frac{2w}{3a_0} \cdot \sqrt{G_{IIc} \cdot E_{If} \cdot h^3}$$

After the assessment of the load limits, the test as prescribed in the standard is executed. If the specimen delaminates in the final test, the load limits are evaluated to assure a reliable estimation of the interlayer fracture toughness. Only if criterion (3.16) is fulfilled, the results are accepted.

$$15 \leq \%G_{Q,j} \leq 35 \quad (3.16)$$

$$\%G_{Q,j} = 100 \cdot \left[ \frac{(P_j \cdot a_j)^2}{(P_{C,0} \cdot a_0)^2} \right] \quad (3.17)$$

The upper limit of this criterion guarantee that the delamination do not occurs prior to final and destructive test, while the lower limit assures that the load-displacement curves of the first two test contain sufficient part that is linear. The latter is essential for a good estimation of the compliance and therefore the interlaminar fracture toughness.

When the criterion is met, the compliance,  $C_j$  for each of the three test is determined by means of linear least squares regression analysis. During the first stage of each test, it possible the recordings show a non linear relationship between the load and the induced displacement. To exclude non-linearities, the standard prescribes a lower limit of 90N, but can be adjusted if necessary.

As explained in the previous section, the compliance is a function of the crack length,  $a$ . The compliance of the end notched flexure specimen is expressed as:

$$C = A + ma^3 \quad (3.18)$$

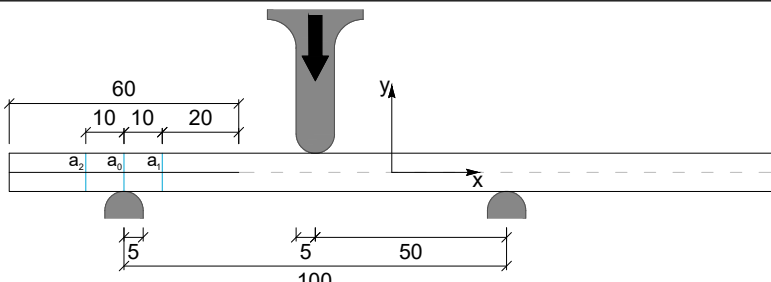
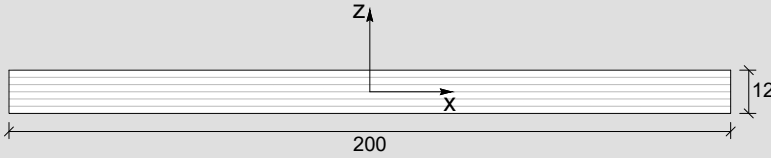
Based on the expression (3.13), the mode II interlaminar fracture toughness can be calculated with the following definition.

$$G_{IIc} = \frac{3m \cdot P_{max}^2 \cdot a_0^2}{2w} \quad (3.19)$$

### 3.4.6. Dimensions of the delamination specimen

The ASTM standard indicates that the remaining length outside the support is preferred to be at least 15 mm. Moreover, the total length of the specimens must be equal or larger than 160 mm. The standard specifies a criterion for the thickness of the laminated specimen, which must be between 3.4 and 4.7 mm. However, the width of a single filament is expected to be 5 mm or even bigger. Hence, the criterion will never be satisfied. In consultation with the supervisors of this research the dimensions of the specimens are determined and tested by means of a preliminary test.

**Table 3.3:** Specifications for the Mode II delamination test

Delamination test	
<b>Test setup</b>	
<b>Geometry</b>	
<b>Specimen type</b>	Double layered
<b>Equipement</b>	ZwickZ 010
<b>Testing speed</b>	5 mm/min
<b>Test condition</b>	$(20 \pm 2)^\circ\text{C}$ , $(50 \pm 10)\% \text{RH}$
<b>Output</b>	Applied force at midspan $P$ [N] for $a_1$ , $a_2$ and $a_0$ Deflection at mid-span $\delta$ [mm] for $a_1$ , $a_2$ and $a_0$



# 4

## Fabrication of the test specimens

All test specimens are cut out of printed plates, which are composed of either a single filament or two fused filaments per layer, referred to as single or double layered specimens respectively. But to obtain the test specimens several aspects and settings of the fabrication process have to be considered.

### 4.1. Two 3D Printers

The principles of the fabrication method are identical for both printers. This print method is denoted as Extrusion-based Additive Manufacturing and is categorised as Solid Freeform Fabrication (SFF). This is the branch of Additive Manufacturing that includes Fused Filament Fabrication as well. The feed material is supplied to the printers in form of pellets, which have been mixed and dried prior to extrusion. For the fabrication of 3D printed products Aectual have developed two types of printers over the years. The KamerMaker uses a gantry system to print three dimensional products and is basically a scaled up version of the commonly used Fused Filament Fabrication printers. The other printers are extruders mounted on a robot arm and is officially appointed as ABB irb6400r/2.8-200, but are appointed to as the Static and the Track Robot. Theoretically, the KamerMakers are capable of printing higher geometries (along the z-axis) and the robot arms can print bigger dimensions in the xy-plane.



Figure 4.1: KamerMaker



Figure 4.2: Static and Track Robot

#### 4.1.1. KamerMaker 1 and 2

The development of the first KamerMaker started in 2011 and had been realised in 2013. The KamerMaker 1 and 2 have been used for the production of all geometries in the researches of Baran<sup>13</sup>, Peulen<sup>51</sup>, van der Veen<sup>74</sup>, Wang<sup>77</sup> and Bui<sup>19</sup>. KamerMaker 1 is optimized for printing with the bio-based material Loctite 3D 6910, formerly known as Technomelt and Macromelt. This material is the fully developed version of the material researched by van der Veen<sup>74</sup> and Baran<sup>13</sup> and

especially designed for fabrication method of Aectual.

The print technology of the KamerMaker 2 contains a different heating system, which includes five temperature zones to liquefy the pellets before extrusion. Each temperature zone is separately regulated. Although KamerMaker 2 is able to print the bio-based Loctite 3D 6910, it is especially designed for the to extrusion of multiple types of (recycled) polymers. KamerMaker 2 has fabricated several end-products, but now is mainly used for the exploration and the development of new (mixtures of) polymers as a printing material. Both the test specimen of Wang<sup>77</sup> and Bui<sup>19</sup> are fabricated with KamerMaker 2. The maximal printable volume of KamerMaker 1 and 2 are 1.60 x 1.70 x 2.50 m<sup>3</sup> and 1.48 x 1.70 x 4.0 m<sup>3</sup> respectively.

#### 4.1.2. Static and Track Robots

Both robots have been introduced in 2017. One of them is installed on a track and is restricted to a print bed with dimensions of 9.00 x 2.00 m<sup>2</sup>. The track robot depicted in figure 4.2. The other robot is identical to the Track Robot, but is only allowed to pivot upon its base point and therefore referred to the Static Robot. The robot arm has a printable envelope in the shape of a donut with an inner radius of 1.50 m and outer radius of 3.20 m. However a rectangular printbed of 4.00 x 2.00 m<sup>2</sup> is normally used. Hence, the printable envelope is significantly enlarged by the use of the robot arms, but there are more improvements compared to KamerMakers.

- Three different motors within the print head, including a melt pump. These are linked to the supply of the pellets, the extrusion of the liquefied material and the extrusion screw that pushes the material through the temperature zones and ascertain heating of the pellets.
- 3D Spatial movement of the print head due to 6-axes of rotation in stead of a gantry system.
- The ability to synchronize the robot program with the extruder process
- PID control for pressure and temperatures regulation to keep all of the print related devices in sync with the robot motion. The control unit receives signals and variables from the robot, e.g. speed, and adjusts the action of the motors, heaters, and material feeder accordingly.
- A sixth temperature zone
- More accurate live information of the pressure, temperature and material supply.

These adaptations assure a more constant extrusion flow and more stable material properties of the extruded product.

## 4.2. Print geometries

As elaborated in the previous chapter, the test specimens must meet specific requirements. However, as the geometry were initially printed by the KamerMaker, extra limitations to the dimensions of the prints were introduced. These limitations will be briefly described in this section for a better understanding of the determined dimensions. The final test specimen are cut out of the plate that are printed by the Static Robot. For these prints the dimensions of the prints designed for the KamerMaker have been adopted, because the prints of KamerMaker 2 used for the preliminary test showed adequate results and a change of the dimensions introduces new uncertainties.

### 4.2.1. Restrictions regarding the print path

Because the printing technique of the KamerMaker 2 is based on a continuous feeding system, the print process cannot be easily interrupted. Hence each layer have to be printed with a continuous print path before the print head is raised to the next layer.

### 4.2.2. Horizontal limitations

The test specimens are cut from single and double layered plates. If the plates are skewed, the specimens will obviously not be straight either. These distortion will probably introduce stress concentrations within the specimen during testing. Consequently, this will not guarantee failure purely due to the intended stress. Hence, the design of the geometry has to ascertain straight plates, while these plates must be sufficiently large to cut the test samples with the earlier estimated proportions. The limits of the horizontal dimensions are determined by the warp deformation<sup>78</sup> and distortions

induced by corners and connections. Preliminary prints have indicated that the maximum printable horizontal length without significant warping is approximately 240 mm excluding the distorted areas close to the corners and joints. Moreover, the first layers of the printed are pressed against the print bed to create a brim. Staples must ascertain sufficient adhesion of the printed layers to the print bed and arrest the warping due to thermal gradients within the print.

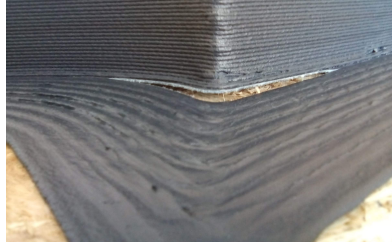


**Figure 4.3:** A brim of compressed layers and warping failure.



**Figure 4.4:** Fixation of the brim.



**Figure 4.5:** Distortion within the printed plate due to the corner.

### 4.2.3. Vertical limitations

Due to the vertical thermal gradient which arise over time, internal stress in the printed geometry develop. These stresses increase with the addition of layers in the vertical directions and causes the geometry to warp. Beyond a specific print height, the internal stress have reached a magnitude which the staples will no longer counteract the distortion and the attachment to the print bed is lost. The printed material can wrap freely causing the nozzle to be pushed into the previous layers and eventually jams the printhead. The maximum printable height of the Kamermaker is 120 mm, which is equal to approximately 60 printed layers.

However, the research of Wang<sup>77</sup> has shown that the properties of first layers varies significantly from the rest of the printed geometry. Subsequently, the lowest two centimetres of the printed plates are excluded from testing.

## 4.3. Material

Over the past few years Aectual has printed with various (mixtures of) polymers. Regarding the environment, recycled polymers are preferred. The available and printable materials during this research are listed below. The recycled HDPE is mainly post-consumer material from pre-sorted plastic packaging waste and contains 5% impurities. Both PP and LDPE are industrial production debris and are refined to be re-used.

### Bio-based polymers

- Loctite 3D 6910
- Technomelt 7616-Y
- Technomelt 7616-9704
- Technomelt 7616-9703
- Technomelt 3909
- Macromelt 6900E

### High Density Polyethylene (HDPE)

- EXPE 851B 0216
- QCP PE 5450EX - 0100

### Polypropylene (PP)

- PPH35 - G30
- PPH08G30 - Black
- Scolefin 53 G10-0 Natural
- Mafill\_CR XG 5344 M
- Scolefin 52 T 10-0
- Scolefin 52 H 13-7
- Scolefin 62 T 01-9

### Low Density Polyethylene (LDPE)

- RDP-V-007572

As indicated before, the evaluation of mechanical properties by means of newly designed test, require reliable results with preferably small variations. This is most likely achieved with print quality as constant as possible. Although the bio-based polymers has the highest print quality of all materials, these do not have adequate mechanical properties for the structural purposes<sup>74</sup>. Moreover, the bio-based material is biodegradable which is unfavourable for outdoor conditions. Hence, the bio-based polymer is excluded from consideration.

In cooperation with the material specialist of Aectual, three different compositions of polymers and additives are evaluated.

- 60% Low Density Polyethylene  
28% Polypropylene + 12% Glass fibres,
- 75% Polypropylene  
10% Glass fibres  
10% Talk  
5% Antioxidants,
- 47% High Density Polyethylene  
32.9% Polypropylene + 14.1% Glass fibres  
5% Colouring agent  
1% UV Blocking + Antistatic agent.

Each additive has a specific task and is added to either increase the printability of the polymers, reduce the warping, equalize the creep in longitudinal and transverse directions, enhance the adhesion between filaments, prevent degradation of the polymers during the operation time of the print or purely for the aesthetic effect. A single pellet of the additive affects a is spread out along the print path as can be seen in figure 4.6.



**Figure 4.6:** The distribution of a single pellet with red colouring agent along the print path of a panel with a surface area of 2.45 x 0.40 m<sup>2</sup>.



**Figure 4.7:** 1% UV+Antistatic **Figure 4.8:** 5% Colour

**Figure 4.9:** 47% PP+GF

**Figure 4.10:** 47% HDPE

The composition with LDPE is really sensitive to warping, while printing with the PP-mixture resulted in skewed plates. Both defects introduce stress concentrations within the specimens and are affecting the reliability of the test results. Fortunately, the mixture of HDPE and PP have shown significantly better print quality and is less prone to warping. Since print quality is assessed on the aesthetics of the printed product, the reliability of the printed specimens must be analysed by means of a preliminary test as well. This preliminary test showed adequate results as well, so the mixture of HDPE and PP was accepted as the material of interest. The pellets of each component in the mixture are depicted in the figures below and the technical specifications are found in Appendix A.

#### 4.4. Optimisation of the extruded polymer

The geometry for the preliminary test specimens have been optimized and printed in KamerMaker 2. Unfortunately, for the final test the print quality delivered by KamerMaker 2 has been significantly decreased. With the identical print parameters the pellets did not melted, but increasing the temperatures leads to degradation of the polymer. Hence, the KamerMaker 2 is not used for the fabrication of the geometry for main tests.



**Figure 4.11:** Insufficient molten pellets



**Figure 4.12:** Degradation of the polymers

In cooperation with the specialist of the robot arms, the print pattern have been adjusted for the Static Robot. Moreover, the chamber of the Static Robot have heated up to 37°C to reduce the thermal gradients within the prints. Hence, the stress concentrations due to warping and contraction of the material are reduced. Finally, the centre-to-centre distance within the double layered geometry has been optimised to prevent accumulation of excess material. Consequently, the surface along all plates of the geometry are even smoother than those fabricated by the KamerMaker 2. The differences are clearly visible in the figures below.

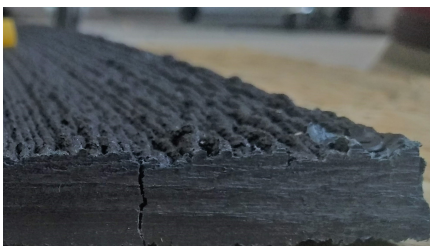


**Figure 4.13:** Plane fabricated by KamerMaker 2 for preliminary test

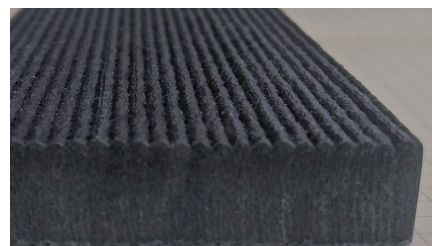


**Figure 4.14:** Plane fabricated by Static Robot for final test

#### 4.4.1. Resizing the print geometry

Due to the reduction of the thermal gradients within the geometry the plates can be printed larger than initially intended. However, a greater print height introduces new uncertainties related to buckling along the vertical build direction and a longer plane is only sufficient if it is twice as long. Hence, the size of the plates within the geometry remains unaltered for geometry of the main test.

#### 4.5. Orientation of the prints

During the whole process from printing the geometries to testing the samples, the orientation of prints keeps changing. For this reason a global and local coordinate system are introduced. Both global and local coordinate systems have a  $xy$ -plane parallel to print and  $z$ -axis is aligned with the upward print direction. The global coordinate system is fixed and located at the lower left corner of the rectangular outer-contour of the each print and is indicated by the uppercase  $X$ ,  $Y$  and  $Z$ . The Origin of the local coordinate system is located in the middle of the layered cross-section of the printed product, referred to by the lowercase  $x$ ,  $y$  and  $z$ .

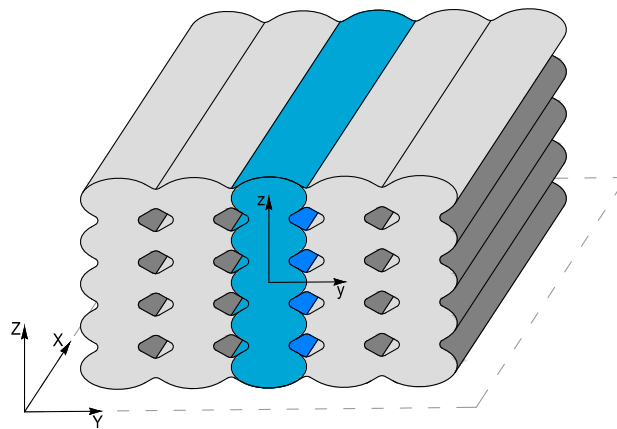


Figure 4.15: Global and local axis

For clarification, the orientation of the prints within each step of the fabrication process and during testing is indicated by either the local or global coordinate system depending on the size of the object of interest. Both systems are indicated in figure 4.15.

#### 4.6. Process parameters

As shown in the previous chapter, five different process parameters have a significant effect on the bonding strength of the printed product. The implementation and the evaluation of each parameter is briefly discussed in the following subsections.

##### 4.6.1. The extrusion temperature

This printing process these parameter is fixed for the printing process, as it has the least affect on the thermal history. Moreover, it is favourable to reduce the amount uncertainties to increase the chance of reliable results. The extrusion screw pushes the raw material through the liquefier. In this process, the material passes through six temperature zone. Each zone gradually heats up the material before it passes to the next zone. The temperature of each specific zone is depicted in the table below. After the sixth zone the material is extruded, so the extrusion temperature is equal to 240°C.

Table 4.1: The temperature of each zone

Temperature zone	1	2	3	4	5	6
Temperature [°C]	150	170	190	210	230	240

### 4.6.2. Envelope temperature

The chamber of the Static Robot is heated up to 37°C by an electric heater prior to the printing process. Hence, the Envelope temperature can not be adjusted during the printing process.

### 4.6.3. Build location

The temperature can not be measured as specific location of the geometry during printing, therefore no significant relationship can be established between the thermal history and a specific build location. So, the build location is excluded from the evaluation of the bonding strength within this research.

### 4.6.4. Print height

Although the print height is restricted to 120mm, this parameter can still be evaluated. The result of specimens cut from various vertical positions within the print plane can be compared. The vertical position is noted on the specimens as soon as it is cut from the plane by the water jet by means of a number. The specimens are count from the top layer towards the bottom layer.

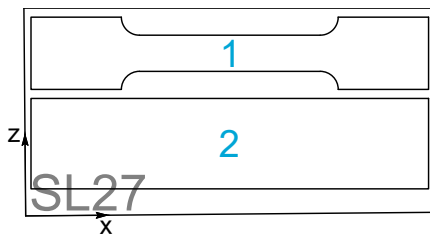


Figure 4.16: Vertical position of tensile and flexural specimens

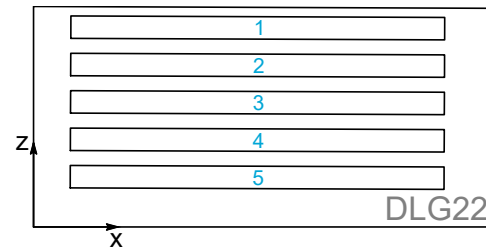


Figure 4.17: Vertical position of delamination specimens

### 4.6.5. The print pattern

The numbers in figures 4.16 and 4.17 indicate the location of the rectangular plane within the print pattern. The design of the print pattern affects the thermal history of printed bead via the so-called interaction time and the overall operation time to print one complete layer. The former is equal to the time that elapse from the moment the bead is extruded until the adjacent filament is printed and differs per printed bead. The latter is identical for each location of the print patter, as the printer must finish a layer before it start extruding the next.

The geometries for the delamination and the double layered tensile and flexural specimens are designed in such away that per vertical location five sample for five different interaction times are created. Besides these 25 plates, some extreme cases are included.

The plates are numbered in accordance with their printer order. For the double layered geometry this is related to the print order of their first filament. The designed print patterns are depicted in Appendix B. The figures below show the obtained single and double layered object. The third figure show the designed gap for the End Notched Flexure specimen.

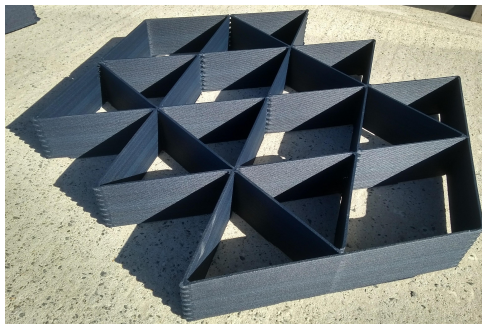


Figure 4.18: The printed single layered geometry

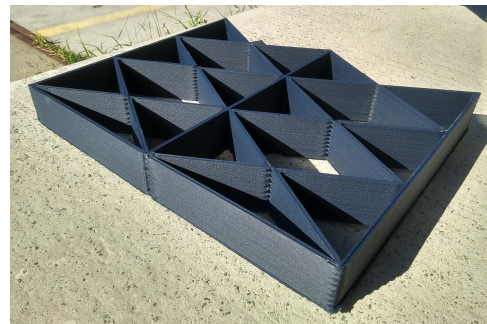
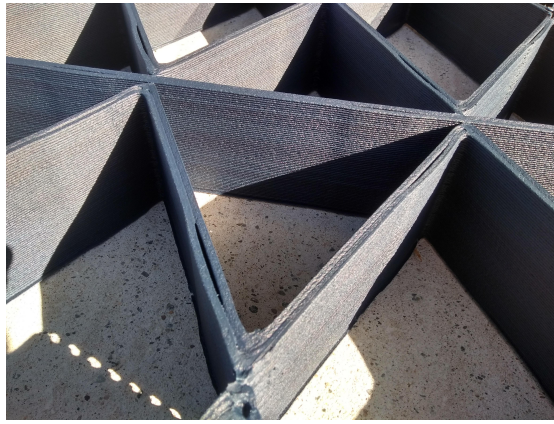


Figure 4.19: The printed double layered geometry



**Figure 4.20:** The designed gap within the geometry for delamination specimens.

## 4.7. Preparation of the specimens

4 days after printing, the geometry are cut and the plates are mounted on wooden plate. Subsequently, the specimens are cut from by water jet cutting machine and the samples are numbered in accordance with the vertical position at the number of the plate from which it originates.

### 4.7.1. Post-processing

After cutting the specimens, the gap within the delamination specimen is opened and is indicated as an insert. This insert must be at least be 55mm long to suit all three test off the compliance method. An inadequate insert is carefully enlarged by means of a jigsaw.

### 4.7.2. Marking the specimens

Prior to the delamination tests, each specimen was marked with fluorescent dots on both sides along the insert up to the location of the loading nose. This dots are required, because it allows to determine local movement from video records. Consequently, unexpected behaviour of the samples during the test can be reviewed and the crack development can be traced by means of a computer program.

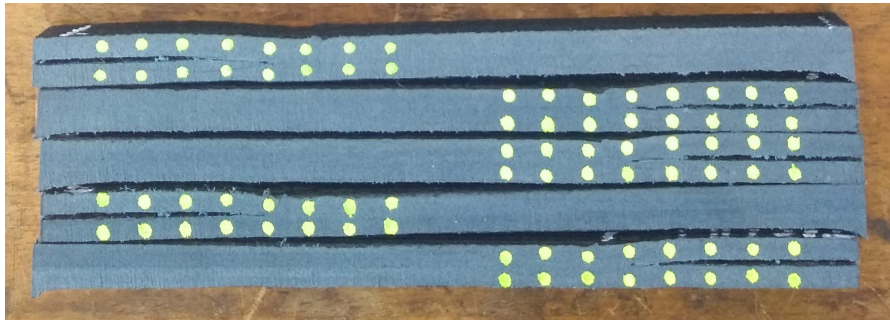


**Figure 4.21:** Delamination specimens with tracing marks.



# 5

## Results

The tests are executed in the same order as described in chapter 3: firstly the tensile test, then the flexural test and finally the Mode II interlaminar Fracture test. The obtained flexural stiffness is used for the initial estimation of the peak loads used in the compliance method for the determination of the Mode II Interlaminar Fracture Toughness.

### 5.1. Tensile test

54 tensile specimens have been destructively tested on the twentieth day after the accomplishment of the geometries by the Static Robot. Before and after each test, the specimen and the failure mechanism are examined. The results of a test are excluded when the initial failure was not introduced in the area between the shoulders of the tensile specimens. Examples of excluded specimens are depicted in figure below.

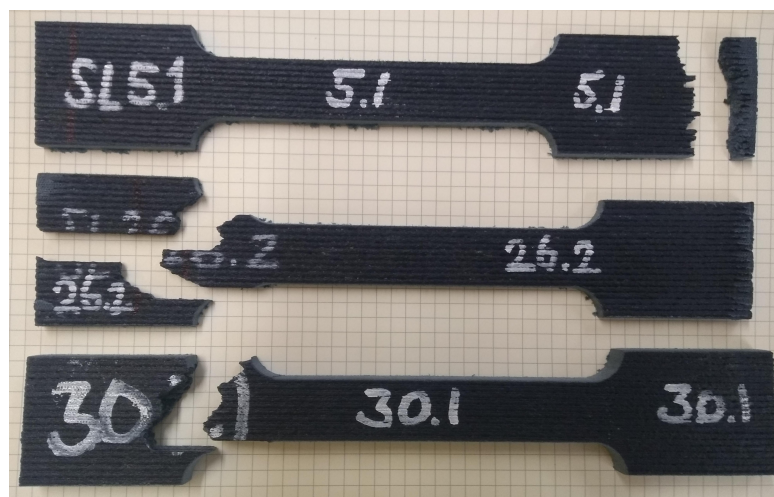


Figure 5.1: Excluded tensile specimens.

As described in ..., the reheating of neighbouring material during printing and the presence of a temperature gradient along the vertical print path involves possible residual stress. These stresses reduce the material properties of the printed material. For evaluation of the material properties, two positions along the vertical print direction are distinguished, namely "Top" and "Bottom" and are marked by a '1' and a '2' on the specimen respectively. The term refer to the upper and lower half of the additively manufactured plates from which they are cut by the water jet.

**Table 5.1:** Number of double layered tensile specimens

Position	Thickness of specimen	
	Single layered	Double layered
Top	12	11
Bottom	13	12
Total	25	23

Even so, it is aspected that the interacting time is relevant for the material properties of the printed specimens. As mentioned before, the interaction time is equal to the elapsed time between print both filaments halway in the plate of interest. Table 5.2 depicts the number of double layered specimens with respect to cooling time per vertical position.

**Table 5.2:** Number of double layered tensile specimens per unit cooling time (1 unit  $\approx$  4.65 s)

Interaction time	Position		Subtotal
	Top	Bottom	
5.4 s	3	1	4
14.6 s	2	3	5
23.8 s	1	2	3
33 s	3	1	4
42.2 s	1	3	4
189.4 s	1		1
309 s		1	1
318.2 s		1	1
Total	11	12	23

**Figure 5.2:** Cracked tensile specimens.

### 5.1.1. Evaluation of the specimens after testing

All 49 of the inspected specimens failed in the same manner and at the same location. The crack is initiated in the area between the narrow section and the root the fillets and runs diagonally towards

the centre line of the shoulder of the specimen resulting in either a v-shaped or stepped crack. Figure 5.2 gives an example of the cracks in the tensile specimens. Lastly, the test specimen fail abruptly without significant yielding. Hence, the print product is considered a brittle material.

The tapered cracks indicate that the specimens did not fail due to pure tension, but most likely due to combination of shear and tensile stresses. As elaborated in the report of Garrell, Shih, Lara-Curzio, and Scattergood<sup>27</sup>, brittle material are more prone to this failure mechanism due to stress concentrations near the fillets. Moreover, the ribbed outer surface of the additively causes an uneven clamping by the grips of the test apparatus, which may contribute to an uneven stress distribution near the fillets<sup>52</sup>.

### 5.1.2. Determination of tensile properties

The resistance of the material related to this failure mechanism is most likely lower than the strength of the printed material related to pure tensile failure. Therefore, the value can be regarded as a lower bound of the tensile strength<sup>27</sup>.

Due to the absence of extensometers during testing, the data obtained from the recordings of the cross head movement are used for the determination tensile properties. Based on conventional mechanics, the records of vertical displacement,  $u$ , and the corresponding load,  $N$ , are used to specify the stress,  $\sigma_t$  and strain,  $\varepsilon$ , for each data point.

$$\varepsilon_t = \frac{u}{L_0} \quad (5.1)$$

$$\sigma_t = \frac{N}{A_{\text{cross}}} \quad (5.2)$$

Subsequently, the chord modulus can be estimated that is a ratio of the difference in stress and strain between to specified points: point 1 and point 2.

$$E_{t,\text{chord}} = \frac{\Delta\sigma_t}{\Delta\varepsilon_t} \quad (5.3)$$

The initial length,  $L_0$ , and the cross-sectional area of the narrow section,  $A_{\text{cross}}$  are assumed to be constants.

$$\begin{aligned} E_{t,\text{chord}} &= \frac{\sigma_2 - \sigma_1}{\varepsilon_2 - \varepsilon_1} \\ &= \frac{L_0}{A_{\text{cross}}} \cdot \frac{P_2 - P_1}{u_2 - u_1} \end{aligned} \quad (5.4)$$

So, for the determination of the tensile stiffness the values for the six parameters in the above expression must be specified.

#### Area of the cross-section: $A_{\text{cross}}$

Because of the layered structure, the cross-section can be schematized as a composition of a rectangular core and small ribs along its width. The shape of these ribs is elliptical and is defined by

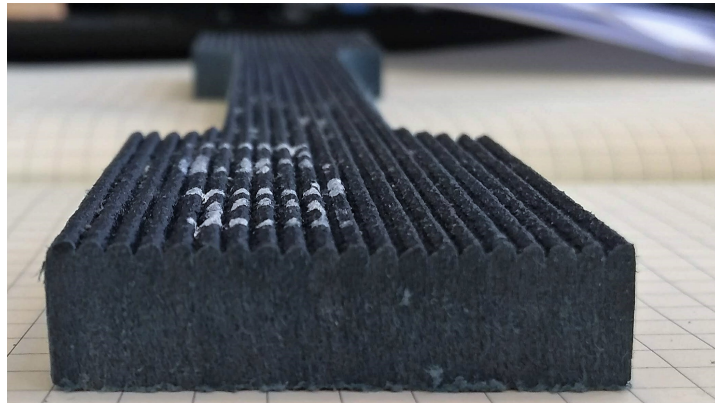


Figure 5.3: Composition of the cross-section.

the half width,  $b$ , and half height,  $a$ . Measuring the width,  $w$ , and dividing it by twice the amount of ribs along one side of this specimen provides the value of  $b$ . Parameter  $a$  is equal to the difference in thickness of the complete cross-section,  $t$ , and the rectangular core. The latter can be determined by measuring the distance between the necks.

Based on all 52 flexural samples, the values of  $b$  is equal to 1 mm. Hence, the height of a single printed filament is approximately 2 mm.  $b$  is independent of the thickness, but  $a$  varies for single and double layered specimens.  $a$  is 0.44 mm and 0.4 mm respectively. The variation of these parameters is insignificant, so they are assumed to be constant for all printed specimens. Subsequently, the cross-sectional area is determined in Appendix C, resulting in the following definition:

$$A_{\text{cross}} = \left( t - 2a + \frac{a \cdot \pi}{2} \right) \cdot w \quad (5.5)$$

$$a_{\text{SL}} = 0.44\text{mm}$$

$$a_{\text{DL}} = 0.4\text{mm}$$

$$b = 1\text{mm}$$

#### Initial length: $L_0$

Due to the absence of gauges the strain must be calculated by means of an reference length. This is the distance between two location on the specimen, wherein all deformation is aspected to take place. Baran<sup>13</sup> calculated an equivalent length,  $L_{\text{eq}}$ , which accounts for the deformation in the fillets, this method is explained in Appendix D. But the crack is initiated at the interface of the fillets and the narrow section and the crack propagates towards the centre of the shoulders, the contribution of the fillets to the elongation of the specimen is doubted. Hence, in this research the initial length is equated to the length of the narrow section:  $L_0 = 100$  mm. For the sake of comparison, the equivalent length is included as well.

$$L_0 = 100\text{mm}$$

$$L_{\text{eq}} = 116.95\text{mm}$$

#### Domain of the tensile chord modulus: $P_1, P_2, u_1, u_2$

The domain as prescribed by the standards is defined by the strain values  $\varepsilon_1 = 0.0005$  and  $\varepsilon_2 = 0.0025$ . However, this domain is located in a curved region, which is explained as take-up of slack and alignment or seating of the specimen prior to the tensile loading<sup>8</sup>. Because of this so-called toe effect, the prescribed domain insufficient. A more accurate domain which is governing for both single and double layered specimens is preferred. Evaluating the records of all tensile specimens, a domain which is identified by the percentages of the maximum load,  $P_{\text{max}}$ , is the most relevant.// Various domain sizes and boundaries have been evaluated by means of a linear least squared regression analysis and the average of the coefficient of determination,  $R^2$  for all load-displacement records. The coefficient of determination indicates the goodness of fit of the linear curve and is a value between 0 and 1. A  $R^2$  closer to 1 represent a good fit, while towards 0 the goodness of the fit of the regression is declining. All evaluated domains and their  $R^2$  are reported in Appendix E. Based on this overview, the boundaries of the domain are set to be equal 67.5%  $P_{\text{max}}$  and 82.5%  $P_{\text{max}}$ . The values of  $u_1$  and  $u_2$  are the corresponding recorded displacement and varies for each tensile specimen.

$$P_1 = 0.675 \cdot P_{\text{max}}$$

$$P_2 = 0.825 \cdot P_{\text{max}}$$

### 5.1.3. Test results

Prior to testing all specimens are measured with a caliper thrice, namely in the middle of the specimen and at the roots of the fillets on both sides of the narrow section. The averaged values for each specimen type with respect to the vertical position in the plate are represented in the table 5.3. The low Coefficient of Variance, CV, confirms the uniform print quality along the printed geometries.

**Table 5.3:** Averaged cross-sectional parameters

		$w$ [mm]	$t$ [mm]	$A_{\text{cross}}$ [mm <sup>2</sup> ]	CV of $A_{\text{cross}}$ [%]
<b>Single</b>	<b>Top</b>	19.90	5.39	103.60	2.63
	<b>Bottom</b>	19.90	5.38	103.34	2.83
<b>Double</b>	<b>Top</b>	19.97	10.44	205.12	2.79
	<b>Bottom</b>	20.02	10.38	204.32	2.01

The width of the double layered specimens is smaller than twice the width of the single layered specimens, because the filaments are printed with a centre-to-centre distance of 5 mm to guarantee sufficient adhesion between the filaments within one layer.

All tensile specimens are tested and the results are presented in table 5.4. A complete overview of the results can be found in Appendix F.

**Table 5.4:** Results from tensile tests

		$P_{\text{max}}$ [N]	$\sigma_{t,\text{max}}$ [N mm <sup>-2</sup> ]	$\varepsilon_{t,\text{max}}$ [%]	$E_{t,\text{chord}}$ [MPa]
<b>Single</b>	<b>Top</b>	3213.04	31.03	5.27	730.42
	<b>Bottom</b>	3033.47	29.38	5.49	686.35
<b>Double</b>	<b>Top</b>	5754.95	28.07	5.95	684.49
	<b>Bottom</b>	5998.34	29.38	6.48	684.71

Expect from the specimens located in the top half of the single layered plates, the tensile chord modulus,  $E_t$ , does not vary significantly. The characteristic values of the tensile strength and stiffness are determined in accordance with the Eurocode standard NEN-EN-1900<sup>45</sup> and the calculation is briefly explained in Appendix J. As is shown in tables 5.5 and 5.6, the scatter of results for all types of specimens are of the same order. The significant difference between the specimens cut out of the top and the bottom part of the single layered plates is decreased.

Considering the tensile stiffness, it is noticed that the Coefficient of Variance, CV, of the double layered specimens is twice to thrice as small as the values of the single layered specimens. Although out of the scope of this research, a possible explanation for this decrease in variation is that a double layered specimen is less prone to the flaws related to single printed filament.

**Table 5.5:** Characteristic tensile strength

		$\sigma_{\text{max},\mu}$ [N mm <sup>-2</sup> ]	CV of $\sigma_{\text{max}}$ [%]	$\sigma_{\text{max},k}$ [N mm <sup>-2</sup> ]
<b>Single</b>	<b>Top</b>	31.03	9.78	25.83
	<b>Bottom</b>	29.38	9.96	24.38
<b>Double</b>	<b>Top</b>	28.07	10.02	23.24
	<b>Bottom</b>	29.38	6.24	26.24

**Table 5.6:** Characteristic tensile stiffness

		$E_{t,\mu}$ [MPa]	CV of $E_t$ [%]	$E_{t,k}$ [MPa]
<b>Single</b>	<b>Top</b>	730.42	13.27	564.46
	<b>Bottom</b>	686.35	11.64	549.94
<b>Double</b>	<b>Top</b>	684.49	4.48	631.76
	<b>Bottom</b>	684.71	5.51	620.06

Lastly, regarding the values in 5.5 and 5.6 no significant difference in tensile properties due to vertical position in the prints can be identified.

## 5.2. Flexural test

The flexural specimens were tested 21 days after the geometries were printed. All samples are examined and measured in advance of testing. 52 rectangular shapes were cut by the water jet, but the dimensions of two specimens exceeds the prescribed range of deviation by the standard<sup>47</sup> and are excluded from the tests. Tables 5.7 and 5.8 report the amount of samples per specimen type for each vertical position and the elapsed time to cool before the printing of the neighbouring filament within a layer.

**Table 5.7:** Number of flexural specimens per type

Position	Thickness of specimen	
	Single layered	Double layered
Top	12	13
Bottom	13	12
<b>Total</b>	25	25

**Table 5.8:** Number of double layered flexural specimens per unit cooling time (1 unit  $\approx$  4.65 s)

Cooling time	Position		Subtotal
	Top	Bottom	
5.4 s	1	4	5
14.6 s	3	2	5
23.8 s	2	2	4
33 s	1	3	4
42.2 s	2	1	3
189.4 s		1	1
290.6 s	1		
309 s	1		1
318.2 s	1		1
<b>Total</b>	12	13	25

### 5.2.1. Evaluation of the specimens after testing

No extraordinary failure mechanism have occurred during the test of all flexural samples. All samples failed directly underneath the loading nose. However, some double layered specimens showed interesting fracture surfaces with a shift in the crack, see figure 5.4. This failure can be linked to shear failure<sup>75</sup> and is a confirmation of the relevance to research the intralayer debonding and its resistance against shear.

### 5.2.2. Determination of the flexural properties

The extensometers are absent in the flexural test. Hence, the flexural strength and stiffness are calculated by means of the recorded deflection at midspan,  $\delta$ , and the corresponding load,  $P$ .

$$\varepsilon_f = \frac{6\delta \cdot t}{(2L_s)^2} \quad (5.6)$$

$$\sigma_f = \frac{P \cdot L_s \cdot t}{8I_{\text{cross}}} \quad (5.7)$$

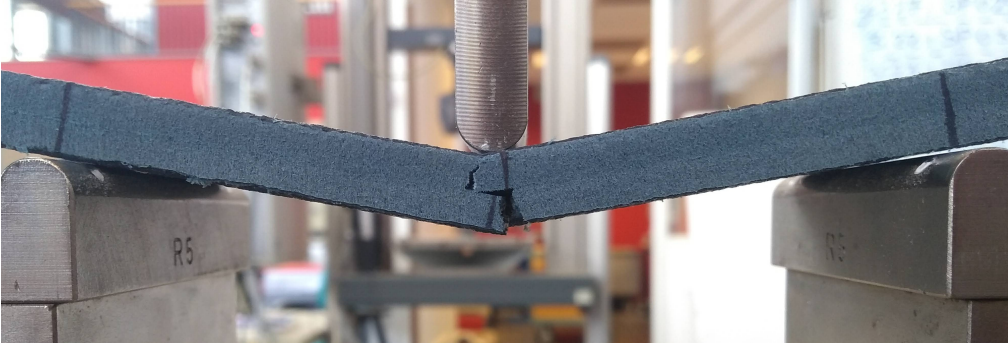


Figure 5.4: Shift in crack in the flexural specimen

The support span,  $2L_s$ , and cross-sectional parameters ( $w$ ,  $t$  and  $I_{\text{cross}}$ ) are independent of the induced displacement and the corresponding load. The flexural stiffness is determined by the chord modulus.

$$E_{f,\text{chord}} = \frac{\Delta\sigma_f}{\Delta\varepsilon_f} \quad (5.8)$$

$$= \frac{L_s^3}{12I_{\text{cross}}} \cdot \frac{P_2 - P_1}{\delta_2 - \delta_1} \quad (5.9)$$

Similar to the derivation of the strength and stiffness from the tensile test, the unknown variables have to be identified. Since the half span length is defined in the standard, only the domain over which the chord modulus is calculated and the moment of inertia of the cross-section,  $I_{\text{cross}}$ , have to be investigated.

$$L_s = 57.5\text{mm}$$

#### The moment of inertia of the cross-section: $I_{\text{cross}}$

The composition of the cross-section is described in section 5.1.2 and depicted in figure 5.3. In order to calculate the total moment of inertia, one must specify the centre of gravity,  $\bar{y}_i$ , area,  $A_i$ , and moment of inertia,  $I_i$ , of each component. See Appendix C for further explanation.

$$I_{xx}^{\text{print}} = \frac{1}{12}w \cdot (t - 2a)^3 + \left[ a^2 \cdot \left( \frac{\pi}{8} - \frac{8}{9\pi} \right) + \frac{\pi}{2} \cdot \left( \frac{4a}{3\pi} + \frac{t - 2a}{2} \right)^2 \right] \cdot wa \quad (5.10)$$

#### Domain of the flexural chord modulus: $P_1, P_2, \delta_1, \delta_2$

Once again the specified domain is not sufficient for the determination of the chord modulus. Although the domain fits for the single layered specimen, a range sufficient for both single and double layered specimens is preferred. The concept is identical to the approach of tensile domain. The table in Appendix G shows the best fit for a domain between 15% and 30% of the measured load at break.

$$P_1 = 0.15 \cdot P_{\text{max}}$$

$$P_2 = 0.30 \cdot P_{\text{max}}$$

### 5.2.3. Test results

The width and thickness of the specimen are measured at the location of the supports and of the loading nose. Table 5.9 represents the mean values for each vertical position of both specimens types.

Table 5.9: Averaged cross-sectional parameters

		$w$	$t$	$I_{\text{cross}}$	CV of $I_{\text{cross}}$
		[mm]	[mm]	[mm <sup>4</sup> ]	[%]
Single	Top	49.61	5.42	595.51	5.48
	Bottom	49.80	5.41	593.09	4.43
Double	Top	50.08	10.49	4600.31	6.07
	Bottom	50.02	10.43	4502.65	5.40

**Table 5.10:** Results from flexural tests

		$P_{\max}$ [N]	$\sigma_{f,\max}$ [N mm <sup>-2</sup> ]	$\varepsilon_{f,\max}$ [%]	$E_{f,\text{chord}}$ [MPa]
<b>Single</b>	<b>Top</b>	424.94	55.69	2.29	3167.44
	<b>Bottom</b>	402.54	52.83	2.34	2974.82
<b>Double</b>	<b>Top</b>	1624.71	53.35	2.42	2692.27
	<b>Bottom</b>	1665.11	55.47	2.43	2798.59

Where the tensile results of both layer thickness are more or less the same, there flexural chord modulus differs considerably. In extension of the observed crack shift in some of the double layered specimen, it is reasonable that shear stresses between the printed filaments have reduced the recorded stiffness of the material.

Tables 5.11 and 5.12, show once more higher values for the specimens cut from the top part of the single layered plates compared to the other specimen types. However, the difference between the results of the top and bottom double layered specimens is, although less significant, reversed. Except from speculation, no statement can be based on the examination of the specimens and their corresponding test results.

**Table 5.11:** Characteristic flexural strength

		$\sigma_{\max,\mu}$ [N mm <sup>-2</sup> ]	CV of $\sigma_{\max}$ [%]	$\sigma_{\max,k}$ [N mm <sup>-2</sup> ]
<b>Single</b>	<b>Top</b>	55.69	3.61	52.25
	<b>Bottom</b>	52.83	3.19	49.96
<b>Double</b>	<b>Top</b>	53.35	3.18	50.44
	<b>Bottom</b>	55.47	2.57	53.04

**Table 5.12:** Characteristic flexural stiffness

		$E_{t,\mu}$ [MPa]	CV of $E_t$ [%]	$E_{t,k}$ [MPa]
<b>Single</b>	<b>Top</b>	3167.44	4.43	2927.40
	<b>Bottom</b>	2974.82	3.61	2791.55
<b>Double</b>	<b>Top</b>	2692.27	3.97	2509.14
	<b>Bottom</b>	2798.59	4.56	2580.59



### 5.3. Mode II Delamination test

Based on the preliminary tests and the flexural modulus for the double layered specimens, the initial peak loads for the compliance method of test for the review of the intralayer bonding strength is estimated.

$$P_{20\text{ mm}} = 227.5\text{N}$$

$$P_{40\text{ mm}} = 113.7\text{N}$$

Excluding the preliminary test, 160 specimens were prepared for this part of the experiment. Unfortunately, all samples from the plate 3 were excluded before the start of the experiments. These specimens were too damaged after post-processing. Table 5.13 depicts all tested samples related to their vertical position regarded from the tap and the cooling time.

**Table 5.13:** Number of delamination samples.

Interaction time	Position					Subtotal
	16.5 mm	36.5 mm	55.5 mm	75.5 mm	95.5 mm	
7.5 s	5	5	5	5	5	25
20 s	5	5	5	5	5	25
32.5 s	6	6	6	6	6	30
45 s	5	5	5	5	5	24
57.5 s	5	5	5	5	5	25
207.5 s	1	1	1	1	1	5
257.5 s	1	1	1	1	1	5
395 s	1	1	1	1	1	5
407.5 s	1	1	1	1	1	5
420 s	1	1	1	1	1	5
<b>Total</b>	31	31	31	31	31	155

The samples are not tested simultaneously, but in four batches of 50, 52, 25 and 26 samples. All specimens in one batch are tested successively on the same day, which is the 30<sup>th</sup>, 31<sup>st</sup>, 44<sup>th</sup> and 50<sup>th</sup> day after printing respectively. The time periods in between the tests were necessary to evaluate the results and prepare the new specimens.

#### 5.3.1. Examination of the tested specimens

Each failure mechanism was easily derived from the obtained load-displacement diagram. Hence, the video records are useful for reviewing the failure, but the marked dots were not necessary for further analysis.

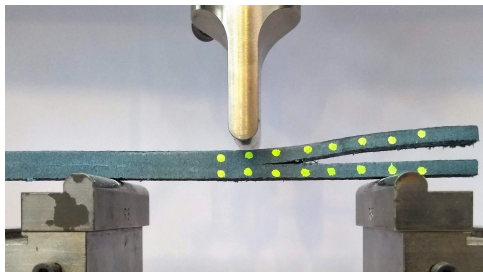


**Figure 5.5:** Failure due to pure delamination

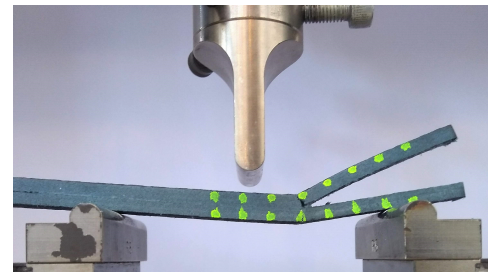


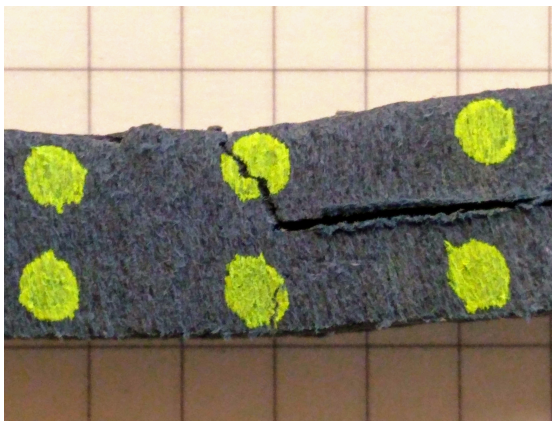
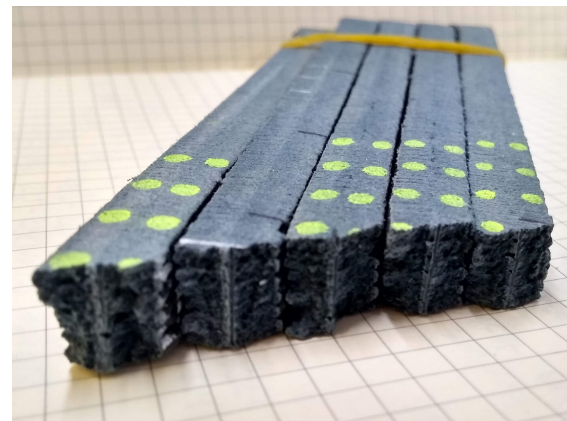
**Figure 5.6:** Failure due to cracking

Of all 155 samples, 59 samples showed symptoms of delamination. For 51 samples the cause of failure can be attributed to full delamination, while the other eight samples fails due to a combination cracking and delamination along the interface. This means that almost one third of the samples (32.9%) have failed due to pure Mode II failure. The numbers of delaminated specimens per condition is indicated in table 5.14.

**Table 5.14:** Number of samples that failed due to Mode II delamination

Cooling time	Position					Subtotal	
	16.5 mm	36.5 mm	55.5 mm	75.5 mm	95.5 mm		
7.5 s					1	1	4.0%
20 s	1	2	1	2	2	8	32.0%
32.5 s		2		2	3	7	23.0%
45 s	2	1	1	1	1	6	25.0%
57.5 s	2	4	2	2	4	14	56.0%
207.5 s	1	1	1	1	1	5	100.0%
257.5 s					1	1	20.0%
395 s	1	1	1	1	1	5	100.0%
407.5 s	1	1	1			3	60.0%
420 s			1			1	20.0%
<b>Total</b>	8	12	8	9	14	5	
	25.8%	38.7%	25.8%	29.0%	45.2%		

Examining the delaminated and the cracked specimens, it is very likely that the post-processing of the specimens have influenced the results. Figure 5.7 shows that the crack propagation does not automatically continues at the crack front but is slightly shifted. Moreover, the crack front created with post-processing of the samples depicted in figure 5.8 clearly after failure due to cracking. Table 5.15 confirms these assumptions, because the post-processed specimens have a considerable lower delamination rate than the non post-processed specimens. Unfortunately, more data on the interlaminar fracture toughness would have been available with a large printed gap and no post-processing, but this also indicate that the relevance of delamination as a failure mechanism in the interlayer bonds is even more significant.

**Figure 5.7:** Discontinuity at the crackfront**Figure 5.8:** Post-processing has affected the material at the crackfront.

### 5.3.2. Test results

For the remaining 51 test samples only the samples that meet the criterion of (3.16) are included for the estimation of the critical energy release rate. Only 33 specimens remain for the determination of interlaminar fracture toughness,  $G_{IIc}$ . These values are depicted in table 5.16. Valid energy release rates,  $G_{IIc}$ , are ordered by plate from which the samples are cut. The number corresponds to those of the delamination geometry in Appendix B.

**Table 5.15:** Part of non post-processed and post-processed specimens that delaminates.

Interaction time	Non post-processed		Post-processed	
	Subtotal	Delaminated	Subtotal	Delaminated
7.5 s	5	0.0%	20	5.0%
20 s	15	55.3%	10	0.0%
32.5 s	5	60.0%	25	16.0%
45 s			24	25.0%
57.5 s	10	80.0%	15	33.3%
207.5 s	5	100.0%		
257.5 s			5	20.0%
395 s	5	100.0%		
407.5 s			5	60.0%
420 s			5	20.0%
<b>Total</b>	<b>45</b>	<b>66.7%</b>	<b>109</b>	<b>19.3%</b>

**Table 5.16:**  $G_{IIc}$  [ $J m^{-2}$ ] of each specimen horizontally sorted by interaction time and individual plate and vertically sorted by the position in the plate. A 'x' indicated an invalid delaminated specimen.

Interaction time	Plate number	Vertical position				
		16.5 mm	36.5 mm	55.5 mm	75.5 mm	95.5 mm
7.5 s	31					984.89
20 s	10		876.15	1180.03	960.92	841.36
	19	1191.77	1422.98		x	x
32.5 s	14					716.17
	18		x		x	858.32
	29		x		1038.11	1154.18
45 s	23	x		x	729.80	618.07
	34	1004.07	x			
57.5 s	12	x	x	x	583.97	501.53
	22	x	1371.91			992.55
	27		806.42	713.78	577.70	x
	33		1102.15			x
207.5 s	21	x	561.41	596.56	x	783.64
257.5 s						x
395 s	6	820.20	705.55	681.53	601.92	610.31
407.5 s	5	x	914.45	861.95		
420 s	4			1019.16		

For a more general understanding of the values depicted by table 5.16 Appendix K reports the critical Strain Energy Release Rate of various adhesives used within the timber industry and several resins of Fibre Reinforced Composites. As can be seen most of the values of  $G_{IIc}$  obtained from the tests are significantly lower than those of the adhesives for wood-adhesive joints, while interlaminar fracture toughness for the resins are similar. Since FRP composites are often treated as laminated structures due to the weaker resins, the test results indicated the importance of the interlayer bonding for in the mechanical characterisation and modelling of the extrusion-based additively manufactured products.

### Vertical position

As expected the results indicates that the specimen closer to the printing bed are more prone to delamination. However, only four plates have provided at least three delaminated specimens from which the G-value can be estimated and these values partly contradict this assumption. So, based on the results no conclusive statement regarding the dependence of the  $G_{IIc}$  on the vertical position is established, but the depicted coherence is in accordance with the literature.

### Interaction time

Regarding the cooling time, an increase of elapsed time weakens the material. However, half of the extreme cases do not agree with this trend. A possible causes of higher G-values for the specimens with a cooling time greater than 400 seconds is the short timespan between print of the second filament and the first filament of next layer. This corresponds to cooling time of 45 and 47.5 s, which have values of the same magnitude. For now this is an educated guess, further research on thermal history has to proven this assumption.

### Print orientation

A more extensive examination reveals that the print direction potentially influences the probability of delamination. Within the print geometry four directions can be distinguished: two diagonal, one in the direction ( $//$  and  $\backslash\backslash$ ) of the global x-axis ( $=$ ) and one in the direction of global y-axis ( $||$ ). The amount of delaminated specimens with regard to their print orientation is reported in table 5.17. Of all orientations, the delamination rate of the  $//$ -oriented specimens is remarkably high, while only a few of  $\backslash\backslash$ -oriented specimens fails due to delamination of the interface.

**Table 5.17:** Failure related to the print orientation

Print direction	Number of specimens	
	Delaminated	Total tested
$//$	4	55
$\backslash\backslash$	31	58
$=$	15	35
$  $	0	5

Reviewing the averaged chord moduli per orientation of the print, show a significant deviation of the flexural stiffness for the same print direction. As the double layered specimens and the delamination specimen are obtained from to different print geometries this clearly indicates the importance of the print direction for the mechanical aspects of the print. As a result of a higher flexural stiffness the stresses at the interface increases under the identical deformation. These stress accumulation will eventually lead to failure of the intralayer bonds by Mode II delamination.

**Table 5.18:** Stiffness related to the print orientation

Print direction	$E_{t,chord}$			$E_{f,chord}$		
	N	$\mu_x$ [MPa]	CV [%]	N	$\mu_x$ [MPa]	CV [%]
$//$	11	733.09	3.99	10	1974.47	10.3
$\backslash\backslash$	8	725.49	5.50	11	2320.60	7.97
$=$	2	733.13	7.02	2	1989.77	7.53
$  $	2	775.30	6.48	2	2014.6	13.4

### Stiffness and the strength based on the build location

Since 5 samples for each of 25 print condition have been tested by means of three point bending test, the stiffness and its dependents on its vertical location and interaction time can be evaluated. The slope of the first test within compliance method is depicted in table 5.19. Only this slope is reviewed since the material has not been stressed by other tests. The specimens with a vertical position of 55.5 mm and 75.5 mm are the stiffest. This is assumed to be caused by sufficient reheating of the material

by the layers on top as the stiffness of the specimens at higher position in the print are lower. Based on literature, the stiffness of the lowest specimen in the plates is assumed to be reduced to greater distortion within the materials due the increasing gradient and the number of heating cycles. Based on the results, the stiffness is seemingly unaffected by interaction time.

**Table 5.19:** Slope of  $P\delta$ -diagram for specimen with 20 mm insert as indication of the stiffness [ $\text{N mm}^{-1}$ ]. The characteristic value is obtained from 125 tested specimens in total.

Interaction time	Vertical Position					Subtotal	
	16.5 mm	36.5 mm	55.5 mm	75.5 mm	95.5 mm		
7.5 s	$\mu_{\text{slope}}$	103.36	112.19	111.59	111.23	109.56	109.59
	$N$	5	5	5	5	5	25
	CV	3.7%	5.6%	6.5%	5.7%	7.5%	5.9%
20 s	$\mu_{\text{slope}}$	96.00	100.81	104.86	102.57	107.00	102.25
	$N$	5	5	5	5	5	25
	CV	8.3%	8.7%	7.8%	8.6%	6.0%	7.8%
32.5 s	$\mu_{\text{slope}}$	93.02	94.12	102.99	102.20	98.96	98.26
	$N$	5	5	5	5	5	25
	CV	8.6%	7.8%	7.2%	6.6%	10.9%	8.9%
45 s	$\mu_{\text{slope}}$	92.54	102.00	106.66	109.18	103.62	102.80
	$N$	5	5	5	5	5	25
	CV	9.2%	4.3%	8.9%	4.0%	5.4%	8.3%
57.5 s	$\mu_{\text{slope}}$	97.99	101.57	109.71	110.25	105.53	105.01
	$N$	5	5	5	5	5	25
	CV	6.3%	7.5%	5.5%	6.9%	6.2%	7.8%
Subtotal	$\mu_{\text{slope}}$	96.58	102.14	107.16	107.09	104.93	103.58
	$N$	25	25	25	25	25	125
	CV	7.9%	8.6%	7.2%	7.0%	7.6%	8.4%
<b>Characteristic value of slope, <math>X_k</math></b>						89.17	

**Table 5.20:** Averaged load at failure,  $P_c$ , per unit width [ $\text{N mm}^{-1}$ ]. Given:  $P_1 = \pm 227.50 \text{ N}$ ,  $P_2 = \pm 113.75 \text{ N}$ .

Interaction time	Vertical Position					Subtotal	
	16.5 mm	36.5 mm	55.5 mm	75.5 mm	95.5 mm		
7.5 s	$\mu_{P_c}$	24.58	27.64	26.66	24.60	27.53	26.20
	$N$	3	3	3	3	3	15
	CV	4.1%	7.8%	0.9%	7.6%	1.2%	7.0%
20 s	$\mu_{P_c}$	25.70	25.08	27.59	26.10	25.62	26.04
	$N$	2	3	3	3	3	14
	CV	1.5%	7.6%	3.5%	11.7%	13.5%	8.4%
32.5 s	$\mu_{P_c}$	25.73	23.87	27.22	26.14	24.80	25.51
	$N$	3	4	4	4	5	20
	CV	8.6%	7.8%	7.2%	6.6%	10.9%	7.5%
45 s	$\mu_{P_c}$	25.19	25.47	28.30	27.79	27.61	26.73
	$N$	4	4	4	3	2	17
	CV	3.9%	12.0%	1.2%	7.9%	3.5%	8.0%
57.5 s	$\mu_{P_c}$	22.57	23.39	25.51	28.12	22.69	24.18
	$N$	4	3	3	2	2	14
	CV	18.4%	19.8%	26.3%	6.9%	23.3%	18.8%
Subtotal	$\mu_{P_c}$	24.59	25.04	27.14	26.42	25.60	25.76
	$N$	16	17	17	15	15	80
	CV	9.5%	11.6%	9.7%	8.5%	10.8%	10.5%
<b>Characteristic value of max load, <math>X_k</math></b>						21.35	

Subsequently, the maximum load which is equal to the load of failure of the third test of the compliance method is reviewed. Since the peak forces have continuously been adapted during the test, only specimens with the most common loading conditions are evaluated. The averaged values per build location are shown in table 5.20. The results are in accordance with the stiffness variations across the print locations and no particular deviations are reported.

Hence, mechanical properties related of the prints are mainly influenced by the vertical positions in the print.

## 5.4. Summary

Based on the test results within the research and the examined materials in the previous researches<sup>13,77</sup>, this composition of thermoplastics as an feed material for extrusion-based additive manufacturing has shown significant improvements for the mechanical aspects of the printed product. However, with increasing strength and stiffness the probability of failure due to delamination increases. Evaluation of the results indicates a dependency of the interlaminar fracture toughness of the build location and orientation. Unfortunately, this dependency cannot be quantified.

## 5.5. Design criteria

Finally, for a better understanding of the delamination properties of the Extrusion-based Additively Manufactured products by Aectual and its relevance for structural design, the interlaminar fracture toughness can be linked to the dimensions of the 3D printed samples. The flexural resistance,  $M_{\text{capacity}}$  [N mm], for a double layered joint of a façade with a specific single layer thickness,  $t$ , is expressed by:

$$M_{\text{capacity}} = \frac{f_y \cdot I_{\text{cross}}}{z} \quad (5.11)$$

The bending moment can be converted into a point load,  $P$  [N], that is working on the joint out of plane of the intralayer bond.

$$\begin{aligned} M_{\text{load}} &= M_{\text{capacity}} \\ \frac{1}{4} \cdot P_f \cdot (2L_s) &= \frac{f_y \cdot I_{\text{cross}}}{z} \\ \frac{1}{2} \cdot P_f \cdot (L_s) &= \frac{f_y \cdot w \cdot (2t)^2}{6} \\ P_f &= \frac{4f_y \cdot w \cdot t^2}{3 \cdot L_s} \end{aligned} \quad (5.12)$$

Regarding the structure feasibility of the print, it is presumed that Mode II delamination within the joint, i.e. failure of intralayer bonds, for values lower than  $P_f$  is undiserable.

$$P_c \geq P_f \quad (5.13)$$

Given the following definition for the critical load for delamination,  $P_c$ . This expression is identical to (3.15).

$$P_c = \frac{4w}{3a} \sqrt{G_{\text{IIC}} \cdot E_{\text{If}} \cdot (\beta t_d)^3}$$

Hence, thickness  $t$  must be increased to at least  $t_d$  to prevent Mode II delamination before the applied load has a magnitude equal to  $P_f$ . Increasing the half thickness obviously increases the moment capacity, but only the initial moment capacity is of interest.

Solving equation (5.13), results in the following expression for  $t_d$ .

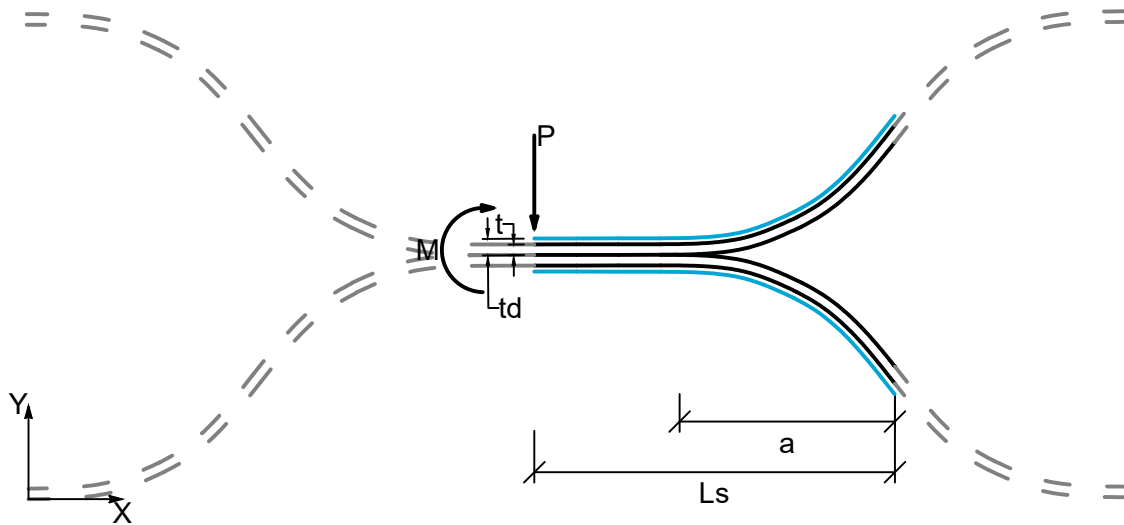


Figure 5.9: Schematised joint within a façade panel designed by DUS. Architects

$$t_d \geq \sqrt[3]{\frac{f_y^2 \cdot a^2 \cdot t}{G_{IIc} \cdot E_{If} \cdot L_s^2}} \cdot t \quad (5.14)$$

$$\beta \geq \sqrt[3]{\frac{f_y^2 \cdot a^2 \cdot t}{G_{IIc} \cdot E_{If} \cdot L_s^2}} \quad (5.15)$$

Given the most unfavourable material properties obtained from the flexural and Mode II fracture test, the scale factor, *beta*, is solely dependent on the geometric parameters:

- the extent of the crack, *a*.
- the half-length between the two considered supports, *L<sub>s</sub>*.
- the initial half thickness of the joint, *t*.

Table 5.21: Most unfavourable material parameters properties

Parmeter	Value
$f_y$	55.47 N mm <sup>-2</sup>
$G_{IIc}$	0.502 J mm <sup>-2</sup>
$E_{If}$	2798.59 MPa

$$\beta \geq \sqrt[3]{\frac{55.47^2 \cdot a^2 \cdot t}{0.502 \cdot 2798.59 \cdot L_s^2}} \quad (5.16)$$

Considering ENF specimens as designed for the estimation of Mode II Interlaminar Fracture Toughness within these report ( $L_s=50\text{mm}$ ,  $a=30\text{mm}$  and  $t=5.12\text{mm}$ ) the layer thickness of the prints have to be

scaled by a factor a factor of 1.54 to withstand the a load that causes flexural failure at the initial width. Since a worst case scenario is considered, this new dimension is aspected to be valid for all tested specimens.

Since the scaling is reasonable, it is relevant to consider this in the design of structural elements. But one must regard the simplicity of this approach: no shear effects are taken into account and pure bending is assumed. Moreover, a sufficient thickness is only obtained by an extra filament which introduce an extra interface.



# 6

## Summary

### 6.1. Previous research

The mechanical properties of additively manufactured products are strongly related to the mesostructure of the print. The mesostructure consist of printed filaments and the bonds between those filaments. The bonds are inferior and introduce discontinuities in the printed material, which result in stress accumulation due to heating and cooling cycles. Also the thermal gradient affects the bonds and are responsible for distortion of the the prints and can even lead to delamination and collapse of the complete printed structure.

Prior to this research the strength of the bonds between the filaments has only been examined in three different researches, which all date back to 2017. Both Aliheidari et al.<sup>4</sup> and Spoerk et al.<sup>62</sup> have investigated the Mode I, while Seppala et al.<sup>60</sup> has implemented a Mode III failure test to determine the mechanical behaviour of the weld zone of the interlayer bond. None of these researches have included numerical result of the delamination test, but have introduced a method to evaluate the bond strength. The results have confirmed the influential factors for delamination which all are strong related to thermal history of the printed product.

Literature indicates that the bond strength and the over all functionality of the prints is effects the most by the following print process parameters:

- Extrusion temperature
- Envelope temperature
- Vertical potion within the print
- The designed print pattern
- Build location within the print envelope

Prior to printing the required geometries the centre-to-centre distance, the extrusion temperature and the envelope temperature have been optimized to enhance the print quality and assure adequate bonding. This must contribute to more reliable results for the determination of the interlaminar fracture toughness. Hence, the research have assessed the interlaminar shear strength mainly on the design of the print pattern and the vertical location.

### 6.2. Test setup

The tensile en fracture test specimens are designed and tested in accordance with the researches of Baran<sup>13</sup> and Wang<sup>77</sup>, because the standards that preferably only test specimens with similar dimensions and test condition shall be compared.

### 6.2.1. Tensile test

Results for the tensile test show no significant difference between specimen cut out of the upper and lower parts of the prints. Moreover, the obtained strength and stiffness from the single and double layered tensile samples are of the same order and do not differ much. However, the single layered specimen have more scattering in the results, which is assumed to be caused by local defects in a printed filament. This is more likely to result in stress concentration than a fault in the double layered specimens. Lastly all valid specimens have failed on the edge of the narrow part and the fillets due stress concentration near the fillets. The failure mechanisms also indicated failure due to a combination of shear and tension stresses. Consequently, the obtained values are lower limits.

### 6.2.2. Flexural test

Each type of flexural specimen show a smaller covariance than for the tensile test, which can be predicted by the absence of corner as they introduce stress concentrations. However, the stiffness of the double layered specimens is smaller than the single layered specimens. This is assumed to be caused by the development of shear stresses in the interface between the printed plates. Some of the tested specimens even show a shift of the crack at the interface, which confirms this assumption.

### 6.2.3. Interlaminar fracture toughness test

The bond strength is evaluated by means of a test methodology derived from the fracture mechanics. This field of expertise focusses on the energy balance at the crack front along the width. By means of a compliance test the correct Strain Energy Release Rate (SERR) or Interlaminar Fracture Toughness of the intralayer can be estimated. The evaluated test-setup is linked to Mode II failure, also known as the sliding mode. This test set-up is favourable, because it does not require adhesives or special measuring equipment. Consequently, this contributes to the reliability of test results and a reduction of errors. Of all 155 specimens tested, 59 specimens showed signs of delamination. 51 specimens have failed due to pure Mode II delamination and 33 specimens met the criterion for the estimation of the Strain Energy Release Rate. This value varied widely for the printed conditions of the specimen. The print condition of each specimen is specified by the vertical position within the printed plate and the interaction time of between the two printed filaments.

Regarding the results, the interlayer bond strength must be included in the mechanical characterisation and the modelling of the printed products. For the structural design of the geometry, a simple hand calculation for the worst case scenario indicated that the scaling-up the thickness of tested geometry by a factor 1.6 would be sufficient to assure no delamination until the critical bending moment related to initial thickness.

## 6.3. Influential factors on the intralayer bonding strength

Due all lot of possible combinations in print conditions, only a few of the combination have more than two valid result related to pure delamination. No adequate mean value have been estimated, but the results have clearly indicated the degradation of the bond strength reversed to the vertical build direction. Hence an increase print height, will enhance the probability of delamination. The relationship between the bond strength and the interaction time is less evident. For the specimens with interaction time of 7.5, 20, 32.5, 45 and 57.5 s there is clear trend of strength reduction when the cooling time increase, but the extreme cases do not confirm this trend. Its exact cause is unknown, but concerning the designed print path the elapsed time between the print of the second filament and the first filament in the next layer is extreme cases significantly smaller and may result in more adequate bonding.

# 7

## Conclusions

This research have tried to estimated a proper method to evaluate the intralayer bond strength of extrusion-based additively manufactured polymers. Via a study on the available literature related to additive manufacturing and the design and implementation of a test method the answers on the following question are determined.

### What is the relevance of intralayer bonding of extrusion-based additively manufactured material for structural purposes?

- What is known within the 3D community about the bonding strength between filaments?
- Which failure test setup is the most relevant and reliable method for the determination of the bonding strength?
- What affects the intralayer bonding strength?

#### 7.0.1. Prior knowledge

The strength of a printed product is predominantly affected by the composition of the mesostructure. The bonds form the weakest link in this mesostructure and the gaps introduces stress concentrations. This magnitude of these stress concentrations is strongly related to the thermal history of each filament and bond. A bigger amount of heating and cooling cycles and greater thermal gradient will result in higher stress concentrations until these exceed a certain limit leading to distortion, delamination or even total collapse of the structure.

#### 7.1. Determination of the bond strength

The bond strength is estimated by means of the test method as prescribed by ASTM-standard D7905/7905M-14. This test demands an rectangular test specimen with insert of at least 55 mm, which are included in the design of the print paths by a means of a small shift perpendicular to print direction. Post-processing of the insert prior test must be avoided, because it strongly affects the probability of delamination.

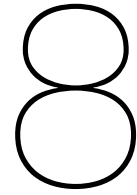
Video records of the test are not necessary, since the obtained load-displacement diagrams clearly indicates the failure mechanism.

#### 7.2. Influential factors

In accordance with the literature and regarding the print restriction of the extrusion-based additive manufacturing process, the strength of the intralayer bond is affected by the vertical location and the interaction time between adjacent filaments within one layer. Moreover, orientation of the print appeared to be of significant impact on both the probability of delamination and the stiffness of the prints.

### **7.3. The relevance of the intra layer bonds**

The results of this research, have proven the importance of the intralayer bonding strength for the the mechanical characterisation of a extrusion-based additively manufactured product. So, when structural elements are fabricated by the printers of Aectual, it is favourable to model the geometries as laminated structure where the filaments are represent by shells as earlier design by Baran<sup>13</sup> and the interlayer bonds between the filaments as interface elements.



## Recommendation

### 8.1. Test specimens

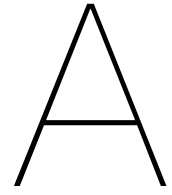
Based on the test of this research, it is concluded that discontinuities strongly affects the mechanical behaviour of the printed specimens. Regarding the design and fabrication of the test specimens it is recommended to:

- En large the radius of the fillets of the tensile specimen to assure failure within the narrow section in stead on the edge close to the fillets.
- Post processing of the delamination specimens to enlarge the insert must be avoided. Hence, redesign the print pattern to assure sufficient large inserts directly after cutting the specimens with the water jet.
- Recommended spacing for cutting by water jet, to prevent loss of specimens by in correction dimension and provide sufficient support during the water jetting.
- Take into account a minim distance of 10 mm between the specimens to assure straight specimens.
- Adjust the order of testing specimens between different plates, to assure a sufficient amount of valid test result per print condition. i.e. Do not always start with the top or bottom specimen of a plate, because when the first specimen of the plate is more likely to be excluded from further evaluation due to the criterion 3.16.

### 8.2. Further research

Regarding the intralayer bonding strength the following topic are relevant for further research:

- Time dependent effects on the bonding strength.
- The actual thermal history of filaments and bonds to predict the bond formation and quantify the effects on various parameters on the bonding strength.
- Experimentally test single and multiple cells to describe the mechanical behaviour of the façade by means of FEM Model and establish useful design criteria related to delamination.



## Properties of feed material



## ■ Scolefin® 53 G 10-0

Polypropylene  
Prime Compound

### Description:

PPH, 30% glass filled, chemically coupled, heat stabilized, natural

### General

MFI (230°/2,16kg)	ISO 1133	15	g/10min
Density	ISO 1183	1.12	g/cm <sup>3</sup>

### Thermal

HDT/A (1,82MPa)	ISO 75A	145	°C
-----------------	---------	-----	----

### Mechanical

Charpy notched impact strength (23 °C)	ISO 179/1eA	8	kJ/m <sup>2</sup>
Charpy unnotched impact strength (23 °C)	ISO 179/1eU	40	kJ/m <sup>2</sup>
Tensile stress at yield	ISO 527	90	MPa
Tensile modulus	ISO 527	6800	MPa

### Various

Ash content (700 °C)	ISO 3451	30	%
----------------------	----------	----	---

Datasheet

The data and information contained herein are typical average values, based on our current level of knowledge and experience, and do not constitute sales specifications. No liability, warranty or guarantee of product performance is created by this document. It is the buyer's responsibility to inspect and test our products in order to determine the suitability for the buyer's application.

### Ravago Group Headquarters

Moerenstraat 85A  
B - 2370 Arendonk

Tel: +32 (0)14 67 25 11  
Fax: +32 (0)14 67 20 12

www.ravago.com  
manufacturing@ravago.com

Issue Date:  
Jul 2014

Page 1 of 1

**Figure A.1:** The Mechanical properties of Polypropylene (PP).

## Technical Data Sheet



### QCP™ PE 5404EX - 0100

#### Product Characteristics

QCP™ PE 5404EX - 100 is a circular high density polyethylene grade supplied in pellet form for extrusion applications.

#### Sustainability

QCP™ PE 5404EX - 0100 contains at least 95% of post-consumer material from pre-sorted plastic packaging waste.

#### Recommended Applications

QCP™ PE 5404EX - 0100 is a general purpose grade that can be used for non-pressure (corrugated) pipe and sheet extrusion applications.

This product is in particular not tested and therefore not validated for use in food, pharmaceutical, medical or potable water applications.

Properties	Units	Nominal Value <sup>1</sup>	Test method
<b>Physical</b>			
Density	kg/m <sup>3</sup>	956	ISO 1183
Melt mass-Flow Rate (MFR) 190 °C, 2.16 kg	g/10 min	0.40	ISO 1133
Melt Volume-flow Rate (MVR) 230 °C, 2.16 kg	cc/10 min	0.52	ISO 1133
Colour		RAL 7012 <sup>2</sup>	CIELlab
Bulk density	kg/m <sup>3</sup>	580	ISO 60
Ash content	%	< 2	ISO 3451-1/A/600°C
Filtration level	µm	150	-
Volatiles	%	< 0.2	ASTM D6980 @ 120°C
Recycled content	%	> 95	EN 15343
<b>Mechanical<sup>3</sup></b>			
Modulus of elasticity	MPa	830	ISO 527-2/1A/1
Tensile strength	MPa	23	ISO 527-2/1A/50
Tensile strain at break	%	85	ISO 527-2/1A/50
Flexural modulus	MPa	870	ISO 178/2
<b>Impact</b>			
Notched Charpy Impact Strength 23 °C, injection moulded	kJ/m <sup>2</sup>	15	ISO 179-1/1eA

<sup>1</sup>) The nominal values are typical values

<sup>2</sup>) closest RAL colour based on CIELab L\*a\*b\* values

<sup>3</sup>) Properties were determined on injection moulded specimens prepared in accordance with ISO 1872-2



Figure A.2: The Mechanical properties of High Density Polyethylene (HDPE).



B

Print patterns for the single layered,  
double layered and delamination  
geometries

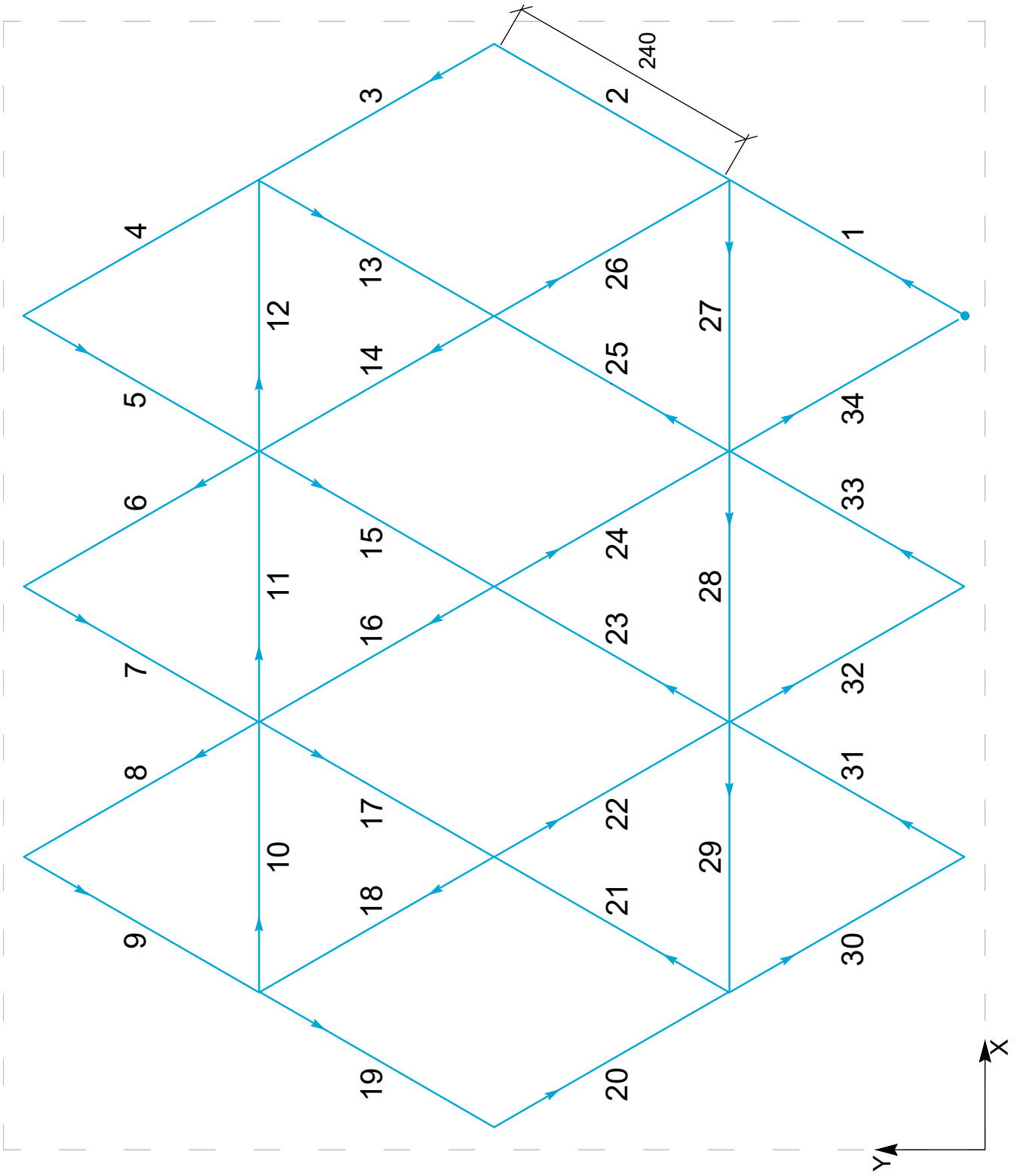


Figure B.1: Print pattern for single layered geometries

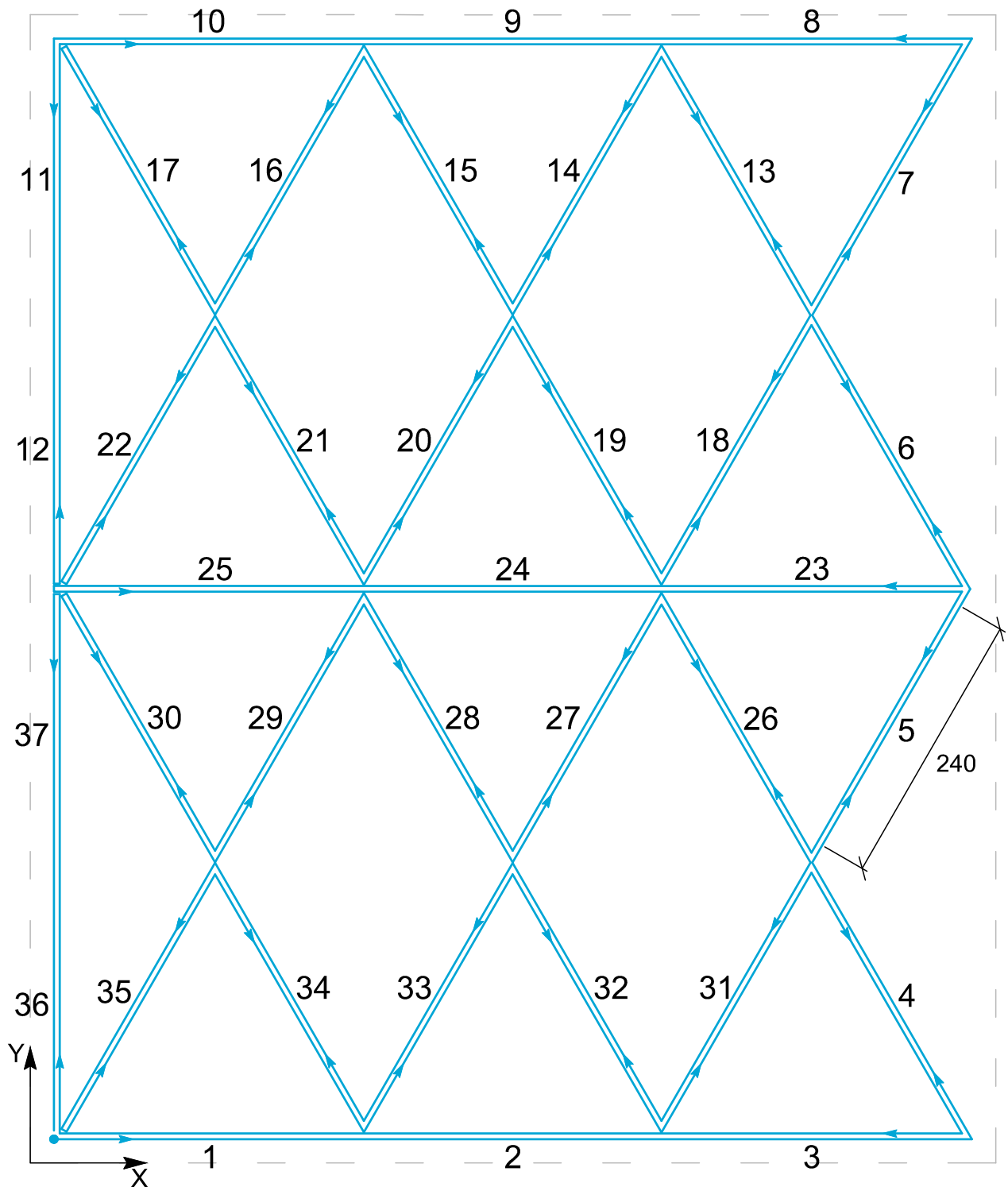


Figure B.2: Print pattern for double layered geometries

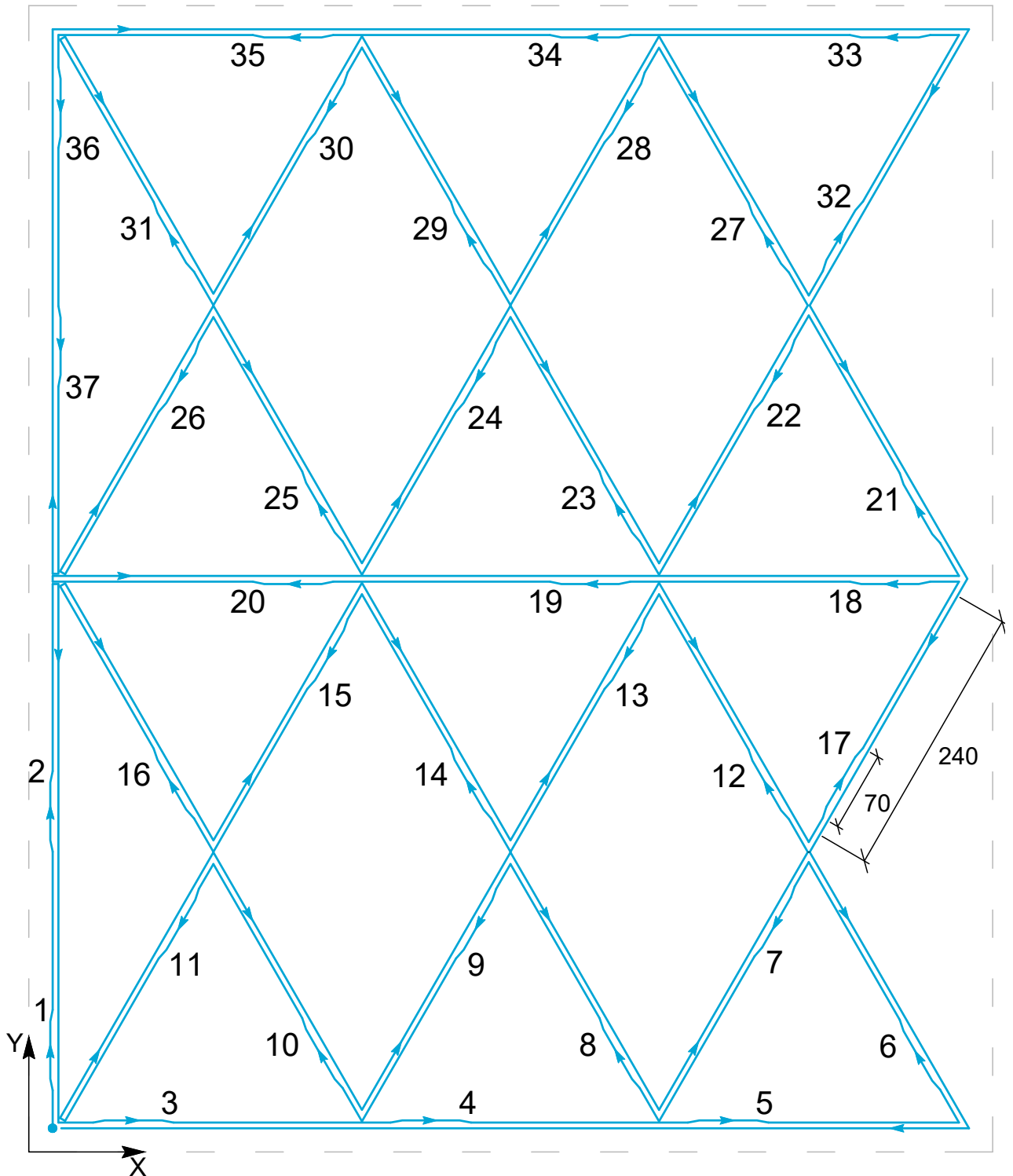
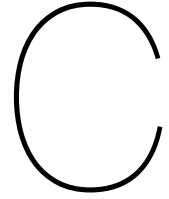


Figure B.3: Print pattern for delamination geometries



## Parameters of the cross-section

### C.1. Parameters

The relevant parameters for the determination of the cross-sectional area and the moment of inertia of the total cross-section are described in the table C.1.

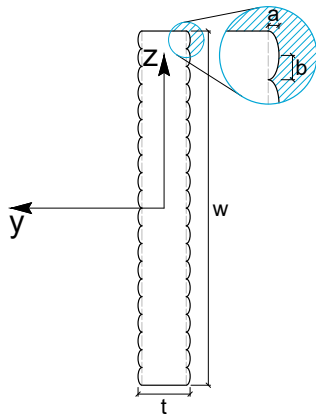


Figure C.1: Composition of the cross-section

Table C.1: Relevant parameters

Element	Parameter	Unit
height of ribs	$a$	mm
half-width of ribs	$b$	mm
thickness of total cross-section	$t$	mm
width of total cross-section	$w$	mm
y-coordinate of centre of gravity	$\bar{y}$	mm
z-coordinate of centre of gravity	$\bar{z}$	mm
cross-sectional area	$A$	mm <sup>2</sup>
moment of inertia	$I$	mm <sup>4</sup>

Since the opening of the nozzle has a circular shape, the extruded filament deforms into an ellipse due to gravity and cohesion to the printed material underneath. This results in a cross-section as depicted in figure C.1. Hence, the cross-section of the prints is schematised as a rectangular core with semi-ellipses on the long edges.

#### C.1.1. Cross-section of the core

The core of the cross-section has a rectangular shape and its width is equal to the measured width. The thickness of this core is equal to the measured thickness minus twice the height of the ribs.

$$A_{\text{core}} = w \cdot (t - 2a) \quad (\text{C.1})$$

#### C.1.2. Cross-section of the ribs

The ribs of the cross-section are shaped like semi-ellipses. The formula of ellipse will be used to calculate the cross-sectional area and the moment of inertia in section C.3.2.

$$\frac{y^2}{a^2} + \frac{z^2}{b^2} = 1 \quad (\text{C.2})$$

The formula of an ellipse can be rewritten as the variable  $y$  which a function of the variable  $z$ .

$$y = a \cdot \sqrt{1 - \frac{z^2}{b^2}} \quad (\text{C.3})$$

The surface area of the semi-ellipse is equal to the integral of expression C.3 from  $x = -b$  to  $x = b$ . This integration is elaborated below.

$$\begin{aligned} A_{\text{rib}} &= \int_{-b}^b y \, dz \\ &= a \cdot \int_{-b}^b \sqrt{1 - \frac{z^2}{b^2}} \, dz \\ &= ab \cdot \int_{-\pi/2}^{\pi/2} \sqrt{1 - \sin^2(u)} \cdot \cos(u) \, du \quad \left. \begin{array}{l} z = b \cdot \sin(u) \\ dz = b \cdot \cos(u) \, du \end{array} \right\} \\ &= ab \cdot \int_{-\pi/2}^{\pi/2} \sqrt{\cos^2(u)} \cdot \cos(u) \, du \\ &= ab \cdot \int_{-\pi/2}^{\pi/2} \cos^2(u) \, du \quad \left. \right\} \cos^2(u) = \frac{1}{2} + \frac{1}{2} \cos(2u) \\ &= \frac{ab}{2} \cdot \int_{-\pi/2}^{\pi/2} 1 + \cos(2u) \, du \\ &= \frac{ab}{2} \cdot \left[ u + \frac{1}{2} \cdot \sin(2u) \right]_{-\pi/2}^{\pi/2} \\ A_{\text{rib}} &= \frac{ab \cdot \pi}{2} \quad (\text{C.4}) \end{aligned}$$

### C.1.3. Number of ribs

The width of one rib is equal to  $2b$  and ribs are present along the width at both sides of the sample. So the number of ribs  $n_{\text{ribs}}$  is equal to twice the width of the specimen divided by the width of one rib.

$$\begin{aligned} n_{\text{ribs}} &= 2 \cdot \frac{w}{2b} \\ n_{\text{ribs}} &= \frac{w}{b} \quad (\text{C.5}) \end{aligned}$$

### C.1.4. Total area of the cross-section

The total cross-sectional area is equal to the summation of the cross-sectional area of the core and all ribs together. So, combining (C.1), (C.4) and (C.5) the total number of ribs provides the formula for the total cross-sectional of the specimen.

$$\begin{aligned} A_{\text{cross}} &= A_{\text{core}} + n_{\text{ribs}} \cdot A_{\text{rib}} \\ &= w \cdot (t - 2a) + \frac{w}{b} \cdot \frac{ab \cdot \pi}{2} \\ A_{\text{cross}} &= \left( t - 2a + \frac{a \cdot \pi}{2} \right) \cdot w \quad (\text{C.6}) \end{aligned}$$

## C.2. Centre of gravity

To determine the moment of inertia of the composed cross-sectional area about the z-axis, the y-coordinates of the centre of gravity of each subarea within the cross-section are required. This is elaborated in the following subsections.

### C.2.1. Centre of gravity of the core element

The location of the centre of gravity of the core is equal to the centre of gravity of the total cross-section:  $\bar{y}_{core}$  and  $\bar{z}_{core}$  are both equal to zero.

$$\bar{y}_{core} = 0 \quad (C.7)$$

### C.2.2. Centre of gravity of the ribs

The z-coordinates of the centre of gravity of each rib depends on its location along the width with respect to the centre of gravity of the complete cross-section and varies per rib. Since only the moment of inertia with respect to z-axis is relevant for this research, the z-coordinates will not be determined. The position of the ribs with respect to the y-axis is constant and equal for all ribs, hence the absolute value of the y-coordinate of the centre of gravity is constant and identical for all ribs. To determine  $\bar{y}$  for one particular rib, a local coordinate system is adopted. The origin of the local coordinate system for each rib is located at the edge of core element:  $\frac{1}{2}(t - 2a)$ , at half-length of the width of the rib.

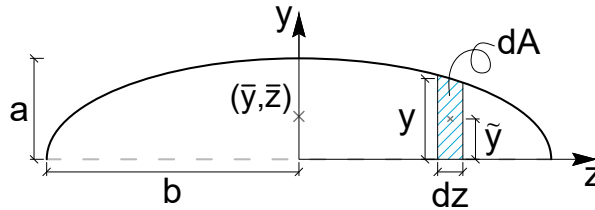


Figure C.2: The determination of the centre of gravity of a rib

As depicted in figure C.2, the surface is divided into very narrow rectangles with a width  $dx$  and a corresponding height  $y$ . The centre of gravity of the semi-ellipse is calculated by means of summation of the products of the area of each small rectangular shape,  $dA$ , with their centre of gravity,  $\tilde{y}$ , divided by the total area of the semi-ellipse:

$$\begin{aligned}
 \bar{y}_{rib}^{local} &= \int_{-b}^b \frac{\tilde{y} dA}{A} \\
 &= \int_{-b}^b \frac{y^2}{2A} dx \\
 &= \int_{-b}^b \frac{y^2}{ab \cdot \pi} dz \\
 &= \frac{2a}{b^3 \cdot \pi} \cdot \int_{-b}^b b^2 - z^2 dz \\
 &= \frac{2a}{b^3 \cdot \pi} \cdot \left[ b^2 z - \frac{z^3}{3} \right]_{-b}^b \\
 &= \frac{2a}{b^3 \cdot \pi} \cdot \left( b^3 - \frac{1}{3} b^3 \right) \\
 \bar{y}_{rib}^{local} &= \frac{4a}{3\pi} \quad (C.8)
 \end{aligned}
 \begin{array}{l}
 \left. \begin{array}{l} \tilde{y} = y/2 \\ dA = y dz \\ A = \frac{1}{2} ab \cdot \pi \\ y^2 = \frac{a^2}{b^2} (b^2 - z^2) \end{array} \right\}
 \end{array}$$

Combining the local y-coordinate of the centre of gravity the location of the local coordinate system in the global system provides the centre of gravity of the rib. This coordinate has the same value for all ribs.

$$\bar{y}_{rib} = \frac{4a}{3\pi} + \frac{t - 2a}{2} \quad (C.9)$$

### C.3. Moment of inertia

The moment of inertia  $I$  is a parameter which indicates the resistance of an object to a change of its orientation. In the mechanics is especially useful for the calculation of the resistance of a cross-section against bending. The moment of inertia of any arbitrary cross-section can be calculated by application of the Steiner's theorem. If the origin of the global coordinate system is located at the centroid of the cross-section, the moment of inertia of the complete cross-section is the summation of the following components:

- the moment of inertia about the line trough the centroid parallel to the axis of interest,  $I_{xc}$ , for each component of the cross-section;
- the product of the area of each component,  $A$ , and the distance between its centre of gravity and the axis of interest,  $d$ , squared. In this report the moment of inertia about the z-axis is concerned, so  $d$  is equal to  $\bar{y}$  of each component.

$$I_{xx} = \sum I_{xc} + A \cdot \bar{y}^2 \quad (\text{C.10})$$

As earlier indicated, the cross-section is composed out of a core element and ribs, located at over entire width of the cross-section.

#### C.3.1. Moment of inertia of the core element

The core element has a rectangular shape and its centroid is equal to the centroid of the complete cross-section. Which results in the following moment of inertia:

$$\begin{aligned} I_{xx}^{\text{core}} &= \frac{1}{12} w t_{\text{core}}^3 \\ I_{xx}^{\text{core}} &= \frac{(t - 2a)^3}{12} \cdot w \end{aligned} \quad (\text{C.11})$$

#### C.3.2. Moment of inertia of the ribs

The ribs are located at long edges of the cross-section, at a distance  $\bar{y}_{\text{rib}}$ . The area of an individual rib is defined by expression (C.4). Only the moment of inertia  $I_{xc}^{\text{rib}}$  is still unknown. For the determination of this parameter the same local coordinate system as in subsection C.2.1 is adopted.

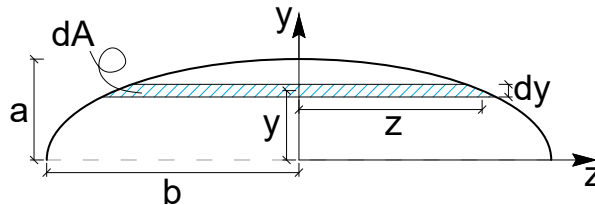


Figure C.3: The determination of the moment of inertia about the local z-axis of a rib

#### Moment of inertia of an individual rib about the local x-axis

Firstly, the moment of inertia with respect to this local z-axis,  $I_{zz}$ , is calculated. The surface of the semi-ellipse is divided in to small rectangles with a width of  $2z$  and a height of  $dy$ . Each area,  $dA$ , is located at a distance  $y$  from the local z-axis. The product of this distance squared and the related area with a limit of  $dy$  to zero provides an integral. The moment of inertia  $I_{xx}^{\text{rib}}$  is equal to this integral from  $y = 0$  to  $y = a$ .

$$\begin{aligned} I_{xx}^{\text{rib}} &= \int_0^a y^2 dA \\ &= \int_0^a y^2 2z dy \\ &= 2 \frac{b}{a} \cdot \int_0^a y^2 \sqrt{a^2 - y^2} dy \end{aligned} \quad \left. \begin{array}{l} dA = 2z dy \\ z = \frac{b}{a} \sqrt{a^2 - y^2} \end{array} \right\} \quad (\text{C.12})$$



$$\begin{aligned}
I_{xx}^{\text{rib}} &= 2 \frac{b}{a} \cdot \int_0^a y^2 \sqrt{a^2 - y^2} dy \\
&= 2 \frac{b}{a} \cdot \int_0^{\frac{\pi}{2}} a^2 \sin^2(u) \cdot \sqrt{a^2 \cdot [1 - \sin^2(u)]} \cdot a \cos(u) du \quad \left. \begin{array}{l} y = a \cdot \sin(u) \\ dy = a \cdot \cos(u) du \end{array} \right\} \\
&= 2a^3 b \cdot \int_0^{\frac{\pi}{2}} \sin^2(u) \cdot \sqrt{\cos^2(u)} \cdot \cos(u) du \\
&= 2a^3 b \cdot \int_0^{\frac{\pi}{2}} \sin^2(u) \cdot \cos^2(u) du \\
&= 2a^3 b \cdot \int_0^{\frac{\pi}{2}} \frac{1}{4} \cdot \sin^2(u) du \quad \left. \begin{array}{l} \sin(u) \cdot \cos(u) = \frac{1}{2} \sin(2u) \\ \sin^2(u) = \frac{1}{2} - \frac{1}{2} \cos(2u) \end{array} \right\} \\
&= \frac{2a^3 b}{8} \cdot \int_0^{\frac{\pi}{2}} 1 - \cos(4u) du \\
&= \frac{a^3 b}{4} \cdot \left[ u - \frac{1}{4} \sin 4u \right]_0^{\frac{\pi}{2}} \\
&= \frac{a^3 b}{4} \cdot \left( \frac{\pi}{2} - \frac{1}{4} \sin(2\pi) \right) \\
I_{xx}^{\text{rib}} &= \frac{a^3 b \cdot \pi}{8} \tag{C.13}
\end{aligned}$$

#### Moment of inertia of an individual rib about the line parallel to the z-axis through the centroid

To determine the moment of inertia about the line parallel to the z-axis through its centre of gravity,  $I_{xx}^{\text{rib}}$ , equation (C.10) is used in reversed order.

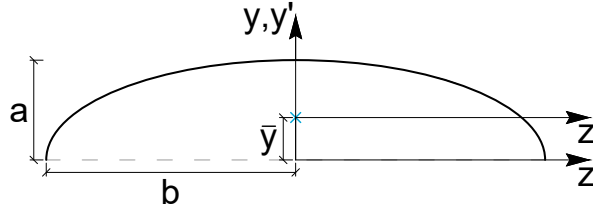


Figure C.4: Shift of the local axis towards the centroid of the rib

$$\begin{aligned}
I_{xc}^{\text{rib}} &= I_{xx}^{\text{rib}} - A_{\text{rib}} \cdot \left( \frac{y_{\text{rib}}^{\text{local}}}{3\pi} \right)^2 \\
&= \frac{a^3 b \cdot \pi}{8} - \frac{ab \cdot \pi}{2} \cdot \left( \frac{4a}{3\pi} \right)^2 \\
&= \frac{a^3 b \cdot \pi}{8} - \frac{ab \cdot \pi}{2} \cdot \frac{16a^2}{9\pi^2} \\
&= \frac{a^3 b \cdot \pi}{8} - \frac{8a^3 b}{9\pi} \\
I_{xc}^{\text{rib}} &= a^3 b \cdot \left( \frac{\pi}{8} - \frac{8}{9\pi} \right) \tag{C.14}
\end{aligned}$$

#### Moment of inertia of all ribs about the x-axis

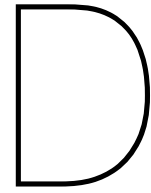
Subsequently, equation (C.10) is used for the determination of  $I_{xx}^{\text{ribs}}$ . Since all ribs have the same dimensions and are all located at distance  $\bar{y}_{\text{rib}}$ , the summation is multiplication of the  $I_{xx}$  for an individual rib and the total number of ribs,  $n_{\text{ribs}}$ .

$$\begin{aligned}
I_{xx}^{\text{ribs}} &= \sum I_{xc}^{\text{rib}} + A_{\text{rib}} \cdot \bar{y}_{\text{rib}}^2 \\
&= n_{\text{ribs}} \cdot (I_{xc}^{\text{rib}} + A_{\text{rib}} \cdot \bar{y}_{\text{rib}}^2) \\
&= \frac{w}{b} \cdot \left[ a^3 b \cdot \left( \frac{\pi}{8} - \frac{8}{9\pi} \right) + \frac{ab \cdot \pi}{2} \cdot \left( \frac{4a}{3\pi} + \frac{t-2a}{2} \right)^2 \right] \\
I_{xx}^{\text{ribs}} &= \left[ a^2 \cdot \left( \frac{\pi}{8} - \frac{8}{9\pi} \right) + \frac{\pi}{2} \cdot \left( \frac{4a}{3\pi} + \frac{t-2a}{2} \right)^2 \right] \cdot wa \tag{C.15}
\end{aligned}$$

### Moment of inertia of the complete cross-section

The moment of inertia of all ribs about the global x-axis are calculated and the moment of inertia of the the core element of the cross-section is known. An addition of these two terms provides the moment of inertia of the whole cross-section.

$$\begin{aligned}
I_{xx}^{\text{print}} &= I_{xx}^{\text{core}} + I_{xx}^{\text{ribs}} \\
I_{xx}^{\text{print}} &= \frac{1}{12} w \cdot (t-2a)^3 + \left[ a^2 \cdot \left( \frac{\pi}{8} - \frac{8}{9\pi} \right) + \frac{\pi}{2} \cdot \left( \frac{4a}{3\pi} + \frac{t-2a}{2} \right)^2 \right] \cdot wa \tag{C.16}
\end{aligned}$$



## The equivalent length

The preparations and tests of the tensile specimens are in accordance to the standard regulated by the Netherlands Normalisatie-Instituut<sup>42</sup> and previous researches of Baran<sup>13</sup> and Wang<sup>77</sup>. However, due to the bad adhesion properties of the material extensometers have not been assembled on the tensile specimens. Other secure measure methods were not available either. Baran stated that the absence of gauges in the setup for testing the tensile samples can be compensated by determination of an equivalent length,  $L_{eq}$ . This equivalent length is used to divide the measured deformation,  $u$ , and obtain the true yield strain,  $\varepsilon_y$ .

However, it is questionable whether this method is valid. For the purpose of comparison this methodology is included in the report and is considered as an upper bound during the determination of the tensile modulus.

### D.1. Previous researches

The fact that the setup for testing the tensile samples does not include extensometers is compensated in the previous researches by determination of an equivalent length,  $L_{eq}$ . The tested tensile specimen has the shape of a dog-bone, with a narrow section and so-called fillets at both sides of the narrow section. The grips of the testing machine are placed at the end of the fillets, these parts are indicated as the shoulders of the tensile specimen. So only the narrow section and the fillets are subject to tension during the test.

The equivalent length,  $L_{eq}$ , is in fact the length of a tensile specimen with a rectangular cross-section, which has dimensions equal to the cross-section at the middle of the tested tensile specimen and is used to determine the "true" yield strength as stated by Baran<sup>13</sup>.

#### D.1.1. Definition of the width as function of the length

For the calculation of the equivalent length the width along the length must be determined. The narrow section has a constant width,  $w$ , but the width of the fillets varies along the length. The width of the fillets the specimen and is defined by a circle equation.

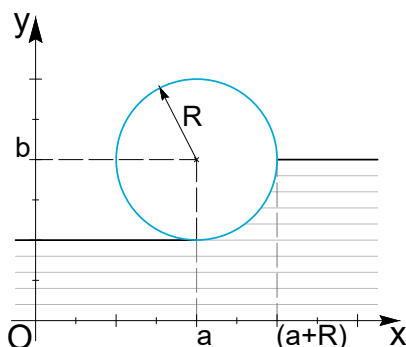
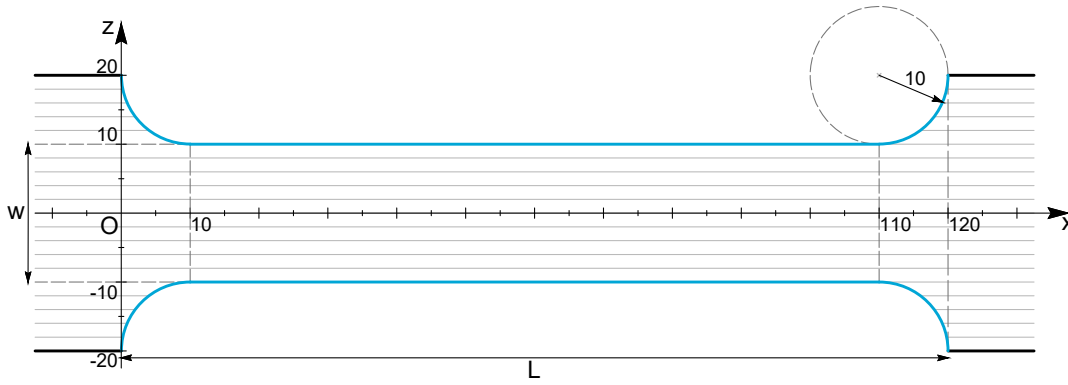


Figure D.1: Numerical representation of a fillet:  $(x - a)^2 + (y - b)^2 = R^2$

$$\begin{aligned}(x - a)^2 + (y - b)^2 &= R^2 \\(y - b)^2 &= R^2 - (x - a)^2 \\y &= b + \sqrt{R^2 - (x - a)^2}\end{aligned}\quad (D.1)$$



**Figure D.2:** Numerical representation of the narrow section and the fillets of a tensile specimen.

Considering the geometry as expressed in figure D.2, the upper fillets are described by the following functions:

$$z_{\text{top, left}} = 0.5w + 10 + \sqrt{100 - (x - 10)^2} \quad (\text{D.2})$$

$$z_{\text{top, right}} = 0.5w + 10 + \sqrt{100 - (x - 110)^2} \quad (\text{D.3})$$

Since the width,  $w$ , is defined by the distance between the cuts and is sliced along the print direction, it varies slightly per specimen. However the radius,  $R$ , is cut at once and is therefore not affected by inaccuracy of the water jet and the ribbed surface. Therefore, the radius is constant and the width is a variable.

Due to symmetry about the  $x$ -axis, the width of the section between the shoulder of the tensile specimen is described by three different functions, each related to a specific domain within this region.

$$w(x) = \begin{cases} w + 20 + 2 \cdot \sqrt{100 - (x - 10)^2} & 0 \leq x \leq 10 \\ w & 10 \leq x \leq 110 \\ w + 20 + 2 \cdot \sqrt{100 - (x - 110)^2} & 110 \leq x \leq 120 \end{cases} \quad (\text{D.4})$$

### D.1.2. Deformation of the specimen

According to the linear theory, the deflection,  $u$ , is equal to the integral of the strain,  $\varepsilon$ , over the length of the section submitted to the tensile load. Subsequently, the strain is a function of the Young's modulus,  $E$ , and the tensile stress,  $\sigma_t$ . The Young's modulus is a properties of the tested material and therefore independent of  $x$ . The tensile stress is equal to the fraction of the applied load,  $P$ , and the cross-sectional area,  $A$ . As is shown in (C.6), the cross-section is a function of the width, and therefore depends on the coordinate  $x$  on the domain of 0 to  $L$ .

$$u = \int_0^L \varepsilon(x) dx \quad (\text{D.5})$$

$$\begin{aligned} &= \int_0^L \frac{\sigma_t(x)}{E} dx \\ &= \frac{1}{E} \cdot \int_0^L \frac{P}{A(x)} dx \\ &= \frac{P}{E} \cdot \int_0^L \frac{1}{(t - 2b + \frac{b \cdot \pi}{2}) \cdot w(x)} dx \\ u &= \frac{P}{E \cdot (t - 2b + \frac{b \cdot \pi}{2})} \cdot \int_0^L \frac{1}{w(x)} dx \end{aligned} \quad (\text{D.6})$$

### D.1.3. The equivalent length

An equivalent specimen has a cross-section with dimensions equal to the narrow section of tested tensile samples. The deformation of this equivalent specimen is expected to be equal to the deformation of the tested specimen under the same loading conditions.

$$u_{\text{eq}} = \frac{P}{E \cdot \left(t - 2b + \frac{b \cdot \pi}{2}\right)} \cdot \int_0^{L_{\text{eq}}} \frac{1}{w(x)} dx$$

$$u_{\text{eq}} = \frac{P}{E \cdot \left(t - 2b + \frac{b \cdot \pi}{2}\right)} \cdot \frac{L_{\text{eq}}}{w} \quad (\text{D.7})$$

Based on (D.4) and (D.6), the deflection of the tested geometry is defined by the following expression.

$$u = \frac{P}{E \cdot \left(t - 2b + \frac{b \cdot \pi}{2}\right)} \cdot \left[ \int_0^{10} \frac{1}{w + 20 + 2 \cdot \sqrt{100 - (x - 10)^2}} dx + \int_{10}^{110} \frac{1}{w} dx + \int_{110}^{120} \frac{1}{w + 20 + 2 \cdot \sqrt{100 - (x - 110)^2}} dx \right]$$

The equivalent length can be calculated via the equality of  $u$  and  $u_{\text{eq}}$ . Because the method is based on identical deformation under the same load conditions for both specimens and the dimensions of the ribs do not depend on the width, the term before the integral is crossed out.

The averaged width,  $w$ , over all specimens is equal to 20.0mm.

$$\frac{L_{\text{eq}}}{20} = \int_0^{10} \frac{1}{40 + 2 \cdot \sqrt{100 - (x - 10)^2}} dx + \int_{10}^{110} \frac{1}{20} dx + \int_{110}^{120} \frac{1}{40 + 2 \cdot \sqrt{100 - (x - 110)^2}} dx$$

$$L_{\text{eq}} = \left[ \int_0^{10} \frac{1}{40 + 2 \cdot \sqrt{100 - (x - 10)^2}} dx + \int_{10}^{110} \frac{1}{20} dx + \int_{110}^{120} \frac{1}{40 + 2 \cdot \sqrt{100 - (x - 110)^2}} dx \right] \cdot 20$$

$$= \left[ \left( \frac{\pi}{4} - \frac{\sqrt{3} \cdot \pi}{9} \right) + 5 + \left( \frac{\pi}{4} - \frac{\sqrt{3} \cdot \pi}{9} \right) \right] \cdot 20$$

$$= \left[ 5 + \frac{\pi}{2} - \frac{2\sqrt{3} \cdot \pi}{9} \right] \cdot 20$$

$$L_{\text{eq}} = 107.23 \text{ mm}$$

## D.2. Deviation from previous reports

Compared to the calculation in the research of Baran<sup>13</sup>, the expression for the width in (D.4) is different due to a typo in the transformation of the circle equation. The sign before the square root was a minus, but expression (D.1) showed that this has to be a plus. In accordance with the calculations in the previous reports, the width is identified as follows:

$$w(x) = \begin{cases} 40 - 2 \cdot \sqrt{100 - (x - 10)^2} & 0 \leq x \leq 10 \\ 20 & 10 \leq x \leq 110 \\ 40 - 2 \cdot \sqrt{100 - (x - 110)^2} & 110 \leq x \leq 120 \end{cases}$$

For the sake of comparison, the equivalent length as defined in the previous reports is calculated as well.

$$\begin{aligned} \frac{L_{\text{eq}}^{\text{old}}}{20} &= \int_0^{10} \frac{1}{40 - 2 \cdot \sqrt{100 - (x - 10)^2}} dx + \int_{10}^{110} \frac{1}{20} dx + \int_{110}^{120} \frac{1}{40 - 2 \cdot \sqrt{100 - (x - 110)^2}} dx \\ L_{\text{eq}}^{\text{old}} &= \left[ \int_0^{10} \frac{1}{40 - 2 \cdot \sqrt{100 - (x - 10)^2}} dx + \int_{10}^{110} \frac{1}{20} dx + \int_{110}^{120} \frac{1}{40 - 2 \cdot \sqrt{100 - (x - 110)^2}} dx \right] \cdot 20 \\ &= \left[ \left( -\frac{\pi}{4} + \frac{\sqrt{3} \cdot \pi}{9} \right) + 5 + \left( -\frac{\pi}{4} + \frac{\sqrt{3} \cdot \pi}{9} \right) \right] \cdot 20 \\ &= \left[ 5 - \frac{\pi}{2} + \frac{2\sqrt{3} \cdot \pi}{9} \right] \cdot 20 \end{aligned}$$

$$L_{\text{eq}}^{\text{old}} = 116.95 \text{ mm}$$

E

## Domain of Tensile Chord Modulus

Interval	Lowerbound	Upperbound	R <sup>2</sup>
0.25	0.1	0.35	0.995379
	0.125	0.375	0.996514
	0.15	0.4	0.997346
	0.175	0.425	0.997933
	0.2	0.45	0.998350
	0.225	0.475	0.998657
	0.25	0.5	0.998887
	0.275	0.525	0.999071
	0.3	0.55	0.999230
	0.325	0.575	0.999388
	0.35	0.6	0.999527
	0.375	0.625	0.999632
	0.4	0.65	0.999706
	0.425	0.675	0.999765
	0.45	0.7	0.999813
	0.475	0.725	0.999848
	0.5	0.75	0.999875
	0.525	0.775	0.999898
	0.55	0.8	0.999918
	0.575	0.825	0.999933
	<b>0.6</b>	<b>0.85</b>	<b>0.999944</b>
	0.625	0.875	0.999935
	0.65	0.9	0.999884
	0.675	0.925	0.999842
	0.7	0.95	0.999810
	0.725	0.975	0.999773

Interval	Lowerbound	Upperbound	R <sup>2</sup>
0.225	0.1	0.325	0.995788
	0.125	0.35	0.996837
	0.15	0.375	0.997602
	0.175	0.4	0.998149
	0.2	0.425	0.998531
	0.225	0.45	0.998810
	0.25	0.475	0.999013
	0.275	0.5	0.999172
	0.3	0.525	0.999306
	0.325	0.55	0.999443
	0.35	0.575	0.999571
	0.375	0.6	0.999669
	0.4	0.625	0.999736
	0.425	0.65	0.999789
	0.45	0.675	0.999830
	0.475	0.7	0.999862
	0.5	0.725	0.999886
	0.525	0.75	0.999906
	0.55	0.775	0.999925
	0.575	0.8	0.999939
	0.6	0.825	0.999948
	<b>0.625</b>	<b>0.85</b>	<b>0.999955</b>
	0.65	0.875	0.999939
	0.675	0.9	0.999873
	0.7	0.925	0.999829
	0.725	0.95	0.999801
	0.75	0.975	0.999770

Interval	Lowerbound	Upperbound	R <sup>2</sup>
0.2	0.1	0.3	0.996234
	0.125	0.325	0.997196
	0.15	0.35	0.997877
	0.175	0.375	0.998368
	0.2	0.4	0.998719
	0.225	0.425	0.998970
	0.25	0.45	0.999150
	0.275	0.475	0.999282
	0.3	0.5	0.999389
	0.325	0.525	0.999505
	0.35	0.55	0.999617
	0.375	0.575	0.999707
	0.4	0.6	0.999768
	0.425	0.625	0.999815
	0.45	0.65	0.999850
	0.475	0.675	0.999877
	0.5	0.7	0.999897
	0.525	0.725	0.999915
	0.55	0.75	0.999932
	0.575	0.775	0.999945
	0.6	0.8	0.999954
	0.625	0.825	0.999959
	<b>0.65</b>	<b>0.85</b>	<b>0.999963</b>
	0.675	0.875	0.999939
	0.7	0.9	0.999856
	0.725	0.925	0.999812
	0.75	0.95	0.999795
	0.775	0.975	0.999768

Interval	Lowerbound	Upperbound	R <sup>2</sup>
0.175	0.1	0.275	0.996703
	0.125	0.3	0.997579
	0.15	0.325	0.998181
	0.175	0.35	0.998598
	0.2	0.375	0.998903
	0.225	0.4	0.999134
	0.25	0.425	0.999292
	0.275	0.45	0.999400
	0.3	0.475	0.999478
	0.325	0.5	0.999572
	0.35	0.525	0.999669
	0.375	0.55	0.999746
	0.4	0.575	0.999799
	0.425	0.6	0.999842
	0.45	0.625	0.999873
	0.475	0.65	0.999895
	0.5	0.675	0.999909
	0.525	0.7	0.999924
	0.55	0.725	0.999939
	0.575	0.75	0.999951
	0.6	0.775	0.999959
	0.625	0.8	0.999965
	0.65	0.825	0.999968
	<b>0.675</b>	<b>0.85</b>	<b>0.999969</b>
	0.7	0.875	0.999934
	0.725	0.9	0.999829
	0.75	0.925	0.999796
	0.775	0.95	0.999793
	0.8	0.975	0.999764

Interval	Lowerbound	Upperbound	R <sup>2</sup>
0.15	0.1	0.25	0.997208
	0.125	0.275	0.997966
	0.15	0.3	0.998498
	0.175	0.325	0.998851
	0.2	0.35	0.999088
	0.225	0.375	0.999287
	0.25	0.4	0.999435
	0.275	0.425	0.999525
	0.3	0.45	0.999574
	0.325	0.475	0.999642
	0.35	0.5	0.999724
	0.375	0.525	0.999789
	0.4	0.55	0.999830
	0.425	0.575	0.999867
	0.45	0.6	0.999895
	0.475	0.625	0.999914
	0.5	0.65	0.999923
	0.525	0.675	0.999932
	0.55	0.7	0.999946
	0.575	0.725	0.999958
	0.6	0.75	0.999964
	0.625	0.775	0.999969
	0.65	0.8	0.999973
	<b>0.675</b>	<b>0.825</b>	<b>0.999974</b>
	0.7	0.85	0.999972
	0.725	0.875	0.999921
	0.75	0.9	0.999793
	0.775	0.925	0.999783
	0.8	0.95	0.999792
	0.825	0.975	0.999735

Interval	Lowerbound	Upperbound	R <sup>2</sup>
0.125	0.1	0.225	0.997747
	0.125	0.25	0.998371
	0.15	0.275	0.998805
	0.175	0.3	0.999111
	0.2	0.325	0.999292
	0.225	0.35	0.999431
	0.25	0.375	0.999562
	0.275	0.4	0.999651
	0.3	0.425	0.999676
	0.325	0.45	0.999713
	0.35	0.475	0.999777
	0.375	0.5	0.999834
	0.4	0.525	0.999863
	0.425	0.55	0.999891
	0.45	0.575	0.999915
	0.475	0.6	0.999933
	0.5	0.625	0.999940
	0.525	0.65	0.999943
	0.55	0.675	0.999950
	0.575	0.7	0.999963
	0.6	0.725	0.999970
	0.625	0.75	0.999972
	0.65	0.775	0.999976
	<b>0.675</b>	<b>0.8</b>	<b>0.999978</b>
	<b>0.7</b>	<b>0.825</b>	<b>0.999978</b>
	0.725	0.85	0.999972
	0.75	0.875	0.999897
	0.775	0.9	0.999743
	0.8	0.925	0.999779
	0.825	0.95	0.999764
	0.85	0.975	0.999670

**Figure E.1:** Inspection of domain with the most appropriate approximation with a linear function for the slope of the  $P,u$ -diagram of all tensile tests. The lower- and upperbound are fractions of the maximum load, which is the applied load at failure.



F

## Raw data - Tensile Test

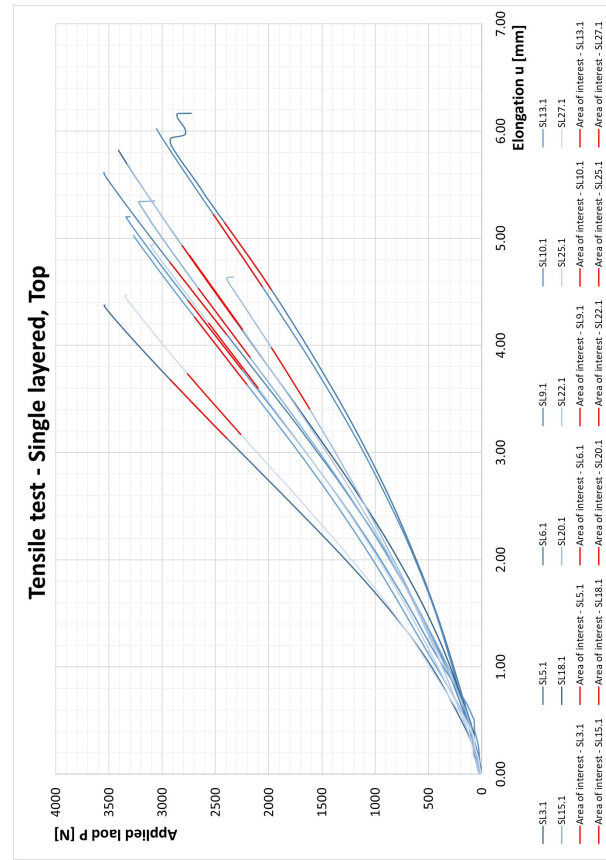


**Figure F.1:** Recorded data of tensile tests applied to single layered specimens that originates from the upper half of the plate.

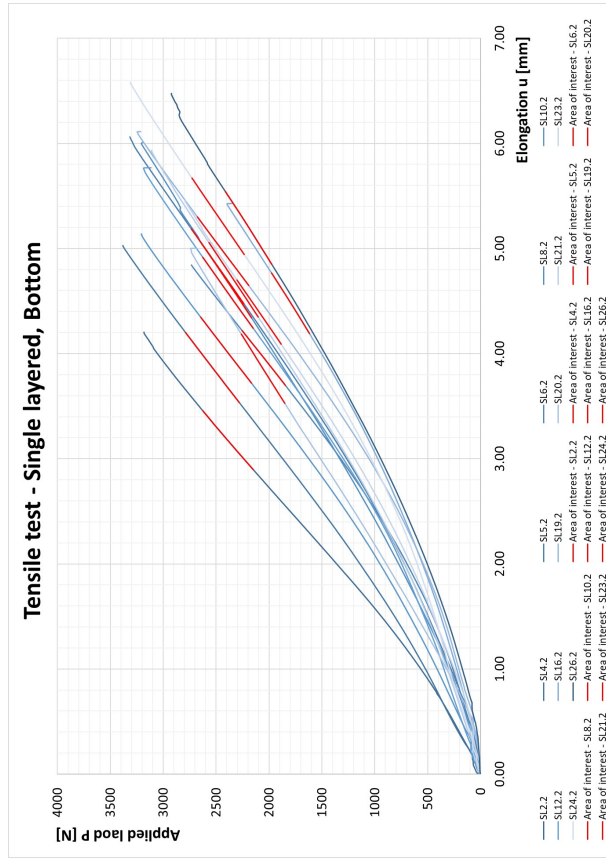


**Figure F.2:** Recorded data of tensile tests applied to single layered specimens that originates from the lower half of the plate.

Table F.1: Raw data of the tensile test performed on single layered specimens.

Test ID	CONDITION				CROSS-SECTIONAL PARAMETERS										INITIAL LENGTH										RESULTS									
	Plate number	Specimen type	Vertical position [mm]	Interaction time [s]	Print direction	Averaged width [mm]	Averaged thickness [mm]	$A_{hib}$ [mm <sup>2</sup> ]	$A_{core}$ [mm <sup>2</sup> ]	$A_{cross}$ [mm <sup>2</sup> ]	$l_0$ [mm]	$l_{eq}^{old}$ [mm]	$l_{eq}$ [mm]	$u_{max}$ [mm]	$P_{max}$ [N]	$\epsilon_{r,max}$ [%]	$\sigma_{r,max}$ [N/mm <sup>2</sup> ]	$u_1$ [mm]	$P_1$ [N]	$u_2$ [mm]	$P_2$ [N]	$l_0$ [MPa]	$E_{t,cbord}$	$l_{eq}^{old}$ [MPa]	$l_{eq}$ [MPa]									
																										$l_0$ [mm]	$l_{eq}^{old}$ [mm]	$l_{eq}$ [mm]	$u_{max}$ [mm]	$P_{max}$ [N]	$\epsilon_{r,max}$ [%]	$\sigma_{r,max}$ [N/mm <sup>2</sup> ]	$u_1$ [mm]	$P_1$ [N]
2	3	Single	Top	n/a	\	20.10	5.45	0.69	91.86	105.75	100.00	116.95	107.23	4.37	3546.05	4.37	33.53	3.13	2394.97	3.68	2924.15	920.35	1076.36	986.91										
3	5	Single	Top	n/a	/	20.07	5.43	0.69	91.37	105.24	100.00	116.95	107.23	5.90	2925.84	5.90	27.80	4.52	1976.15	5.14	2413.17	666.54	779.54	714.75										
4	6	Single	Top	n/a	\	20.12	5.48	0.69	92.60	106.51	100.00	116.95	107.23	5.61	3548.43	5.61	33.32	4.10	2396.41	4.77	2926.85	741.74	867.48	795.38										
11	9	Single	Top	n/a	/	18.90	5.53	0.69	87.95	101.01	100.00	116.95	107.23	6.02	3053.21	6.02	30.23	4.55	2061.95	5.22	2518.43	674.63	789.00	723.42										
12	13	Single	Top	n/a	/	20.10	5.33	0.69	89.51	103.40	100.00	116.95	107.23	5.20	3340.44	5.20	32.30	3.78	2254.99	4.41	2755.50	758.52	887.10	813.37										
13	10	Single	Top	n/a	-	20.13	5.43	0.69	91.67	105.59	100.00	116.95	107.23	5.02	3268.19	5.02	30.95	3.64	2206.65	4.26	2696.02	739.56	864.94	793.05										
14	15	Single	Top	n/a	/	18.80	5.37	0.69	84.35	97.34	100.00	116.95	107.23	5.34	3223.58	5.34	33.12	3.89	2176.51	4.53	2658.99	772.64	903.62	828.52										
5	16	Single	Top	n/a	\	20.20	5.27	0.69	88.61	102.57	100.00	116.95	107.23	6.14	2986.84	6.14	29.12	4.52	2016.34	5.25	2463.78	590.85	691.01	633.58										
6	18	Single	Top	n/a	\	20.23	5.32	0.69	89.77	103.75	100.00	116.95	107.23	5.82	3410.04	5.82	32.87	4.22	2302.50	4.93	2812.72	689.35	806.21	739.20										
7	20	Single	Top	n/a	\	20.02	5.43	0.69	91.14	104.98	100.00	116.95	107.23	4.62	2394.16	4.62	22.81	3.41	1617.39	3.98	1975.01	596.51	697.63	639.65										
8	22	Single	Top	n/a	\	20.23	5.35	0.69	90.44	104.43	100.00	116.95	107.23	5.70	3326.63	5.70	31.86	4.15	2246.06	4.84	2743.52	687.80	804.39	737.54										
9	25	Single	Top	n/a	/	20.08	5.50	0.69	92.79	106.67	100.00	116.95	107.23	4.93	3108.77	4.93	29.15	3.60	2099.67	4.21	2564.56	719.96	842.00	772.02										
10	27	Single	Top	n/a	/	19.93	5.27	0.69	87.44	101.22	100.00	116.95	107.23	4.46	3350.12	4.46	33.10	3.17	2262.10	3.73	2762.55	873.14	1021.15	936.28										
15	2	Single	Bottom	n/a	/	18.80	5.40	0.69	84.98	97.97	100.00	116.95	107.23	4.20	3183.29	4.20	32.49	2.89	2148.90	3.45	2625.63	869.44	1016.83	932.32										
16	4	Single	Bottom	n/a	\	20.08	5.43	0.69	91.45	105.33	100.00	116.95	107.23	5.02	3381.76	5.02	32.11	3.53	2282.80	4.20	2789.57	723.54	846.19	775.86										
17	5	Single	Bottom	n/a	/	20.12	5.37	0.69	90.26	104.16	100.00	116.95	107.23	6.06	3315.53	6.06	31.83	4.47	2238.40	5.19	2735.03	668.54	781.87	716.89										
18	6	Single	Bottom	n/a	\	20.20	5.37	0.69	90.63	104.59	100.00	116.95	107.23	4.84	2734.00	4.84	26.14	3.70	1846.39	4.22	2254.54	750.62	877.87	804.91										
19	8	Single	Bottom	n/a	\	20.03	5.35	0.69	89.55	103.40	100.00	116.95	107.23	6.00	3206.96	6.00	31.02	4.34	2165.62	5.06	2645.62	645.96	755.46	692.67										
20	10	Single	Bottom	n/a	-	19.80	5.23	0.69	86.20	99.88	100.00	116.95	107.23	5.13	3207.98	5.13	32.12	3.72	2166.69	4.35	2646.14	766.07	895.94	821.48										
21	12	Single	Bottom	n/a	-	20.15	5.27	0.69	88.39	102.32	100.00	116.95	107.23	5.76	3185.87	5.76	31.14	4.24	2150.93	4.92	2627.62	690.12	807.11	740.03										
22	16	Single	Bottom	n/a	\	20.05	5.30	0.69	88.62	102.48	100.00	116.95	107.23	5.42	2397.32	5.42	23.39	4.19	1618.49	4.77	1977.09	607.98	711.04	651.95										
23	19	Single	Bottom	n/a	/	20.20	5.42	0.69	91.64	105.60	100.00	116.95	107.23	6.11	3247.18	6.11	30.75	4.65	2192.38	5.30	2677.81	704.83	824.31	755.80										
24	20	Single	Bottom	n/a	\	20.10	5.47	0.69	92.19	106.08	100.00	116.95	107.23	5.00	2742.96	5.00	25.86	3.53	1851.57	4.19	2262.34	588.03	687.72	630.56										
25	21	Single	Bottom	n/a	/	20.18	5.42	0.69	91.57	105.51	100.00	116.95	107.23	5.93	3113.95	5.93	29.51	4.35	2102.92	5.06	2568.73	623.20	728.85	668.27										
27	23	Single	Bottom	n/a	/	18.83	5.43	0.69	85.75	98.77	100.00	116.95	107.23	5.46	2793.20	5.46	28.28	4.09	1885.85	4.70	2303.76	693.22	810.73	743.35										
26	24	Single	Bottom	n/a	\	20.15	5.40	0.69	91.08	105.00	100.00	116.95	107.23	6.57	3309.86	6.57	31.52	4.94	2234.87	5.67	2729.10	647.26	756.99	694.07										
1	26	Single	Bottom	n/a	\	20.13	5.52	0.69	93.35	107.27	100.00	116.95	107.23	6.47	2925.05	6.47	27.27	4.85	1975.18	5.54	2412.49	590.99	691.18	633.73										

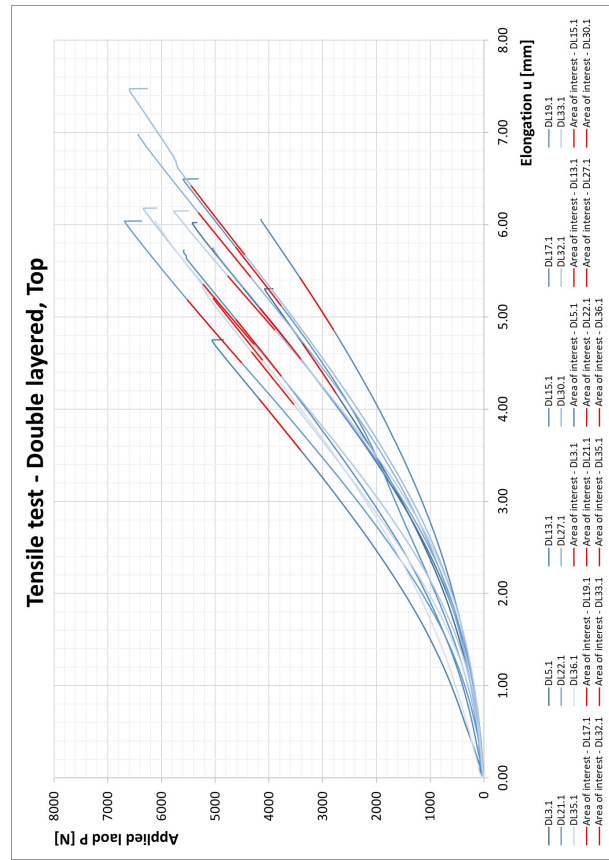


Figure F.3: Recorded data of tensile tests applied to double layered specimens that originates from the upper half of the plate.

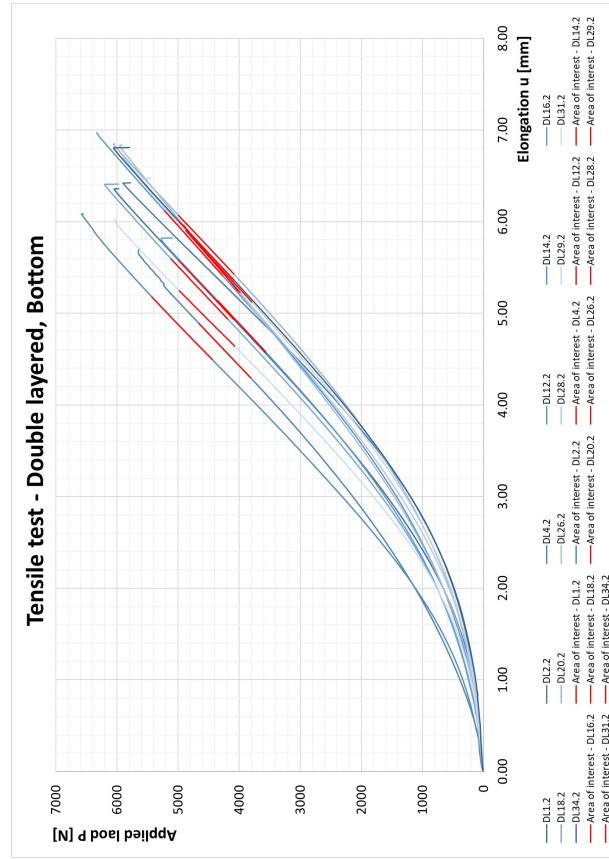


Figure F.4: Recorded data of tensile tests applied to double layered specimens that originates from the lower half of the plate.

Table F.2: Raw data of the tensile test performed on double layered specimens.

Test ID	Plate number	Specimen type	CONDITION			CROSS-SECTIONAL PARAMETERS					INITIAL LENGTH					RESULTS								
			Vertical position [mm]	Interaction time [s]	Print direction	Averaged width [mm]	Averaged thickness [mm]	$A_{fb}$ [mm <sup>2</sup> ]	$A_{core}$ [mm <sup>2</sup> ]	$A_{cross}$ [mm <sup>2</sup> ]	$L_0$ [mm]	$L_{eq}^{old}$ [mm]	$L_{eq}$ [mm]	$u_{max}$ [mm]	$P_{max}$ [N]	$\epsilon_{l,max}$ [%]	$\sigma_{l,max}$ [N/mm <sup>2</sup> ]	$u_1$ [mm]	$P_1$ [N]	$u_2$ [mm]	$P_2$ [N]	$L_0$ [MPa]	$F_{t,chorrd}$ [MPa]	$L_{eq}^{old}$ [MPa]
42	3	Double	Top	299.8	=	20.28	10.52	0.63	197.09	209.83	100.00	116.95	107.23	5.30	4082.60	5.30	19.46	4.17	2756.51	4.70	3366.21	550.44	643.75	590.25
43	5	Double	Top	189.4	//	20.35	10.62	0.63	199.77	212.56	100.00	116.95	107.23	6.01	5424.31	6.01	25.52	4.73	3663.15	5.31	4473.89	656.69	768.01	704.18
30	13	Double	Top	42.2	\	19.93	10.23	0.63	188.04	200.56	100.00	116.95	107.23	4.74	5060.41	4.74	25.23	3.56	3416.28	4.10	4172.71	692.20	809.54	742.26
32	15	Double	Top	23.8	\	19.98	10.77	0.63	199.17	211.72	100.00	116.95	107.23	6.05	4147.45	6.05	19.59	4.86	2800.36	5.42	3420.21	521.49	609.89	559.20
33	17	Double	Top	5.4	\	20.05	10.63	0.63	197.16	209.76	100.00	116.95	107.23	5.71	5591.10	5.71	26.66	4.36	3775.05	4.97	4610.31	654.25	765.16	701.57
34	19	Double	Top	34	\	20.23	10.13	0.63	188.84	201.56	100.00	116.95	107.23	6.49	5598.39	6.49	27.78	5.12	3779.17	5.75	4616.81	659.56	771.36	707.26
35	21	Double	Top	14.6	\	20.22	10.30	0.63	192.06	204.76	100.00	116.95	107.23	6.04	6688.50	6.04	32.66	4.51	4515.81	5.18	5516.01	722.51	844.99	774.76
36	22	Double	Top	5.4	//	20.12	10.55	0.63	196.14	208.78	100.00	116.95	107.23	5.74	5048.99	5.74	24.18	4.54	3409.41	5.09	4164.99	658.45	770.07	706.07
37	27	Double	Top	34	//	19.97	10.42	0.63	192.01	204.56	100.00	116.95	107.23	6.98	6434.08	6.98	31.45	5.43	4345.05	6.13	5307.99	679.49	794.67	728.63
38	30	Double	Top	5.4	\	20.18	10.35	0.63	192.75	205.43	100.00	116.95	107.23	7.46	6599.97	7.46	32.13	5.68	4456.53	6.42	5443.91	648.10	757.97	694.97
39	32	Double	Top	34	\	19.75	10.30	0.63	187.63	200.03	100.00	116.95	107.23	6.17	6335.04	6.17	31.67	4.70	4277.90	5.35	5224.51	729.03	852.61	781.75
41	33	Double	Top	23.8	//	20.07	10.57	0.63	195.98	208.59	100.00	116.95	107.23	6.15	5773.57	6.15	27.68	4.86	3897.66	5.44	4762.88	715.17	836.41	766.90
40	35	Double	Top	5.4	//	18.77	10.50	0.63	182.04	193.83	100.00	116.95	107.23	5.33	5242.78	5.33	27.05	4.05	3539.96	4.62	4322.63	712.34	833.09	763.85
29	36	Double	Top	14.6	//	20.20	10.63	0.63	198.63	211.33	100.00	116.95	107.23	6.04	6107.23	6.04	28.90	4.53	4122.53	5.20	5037.82	649.76	759.91	696.76
44	1	Double	Bottom	318.2	=	20.08	10.30	0.63	190.79	203.41	100.00	116.95	107.23	6.36	6050.22	6.36	29.74	4.93	4085.00	5.58	4990.71	689.88	806.83	739.77
45	2	Double	Bottom	309	=	20.25	10.12	0.63	188.66	201.39	100.00	116.95	107.23	6.42	5901.94	6.42	29.31	5.14	3985.51	5.72	4868.32	756.14	884.32	810.82
46	4	Double	Bottom	290.6	\	20.28	10.10	0.63	188.64	201.38	100.00	116.95	107.23	5.67	5653.11	5.67	28.07	4.30	3817.44	4.89	4661.39	708.24	828.31	759.46
47	12	Double	Bottom	5.4	//	20.12	10.17	0.63	188.43	201.07	100.00	116.95	107.23	6.08	6582.26	6.08	32.74	4.50	4443.49	5.18	5428.40	717.60	839.25	769.50
48	14	Double	Bottom	34	//	19.93	10.75	0.63	198.34	210.86	100.00	116.95	107.23	6.97	6331.45	6.97	30.03	5.41	4274.86	6.12	5222.04	635.77	743.55	681.75
49	16	Double	Bottom	14.6	//	19.95	10.63	0.63	196.18	208.71	100.00	116.95	107.23	5.81	5278.34	5.81	25.29	4.58	3563.66	5.14	4363.74	673.58	787.76	722.29
50	18	Double	Bottom	42.2	//	18.89	10.65	0.63	186.03	197.90	100.00	116.95	107.23	6.41	6203.55	6.41	31.35	4.94	4187.74	5.59	5117.27	712.97	833.83	764.53
51	20	Double	Bottom	23.8	//	20.05	10.48	0.63	194.15	206.75	100.00	116.95	107.23	6.84	6055.98	6.84	29.29	5.43	4089.03	6.07	4993.95	685.06	801.20	734.61
52	26	Double	Bottom	42.2	\	20.12	10.15	0.63	188.09	200.73	100.00	116.95	107.23	6.83	5956.53	6.83	29.67	5.24	4021.40	5.96	4911.69	619.98	725.07	664.81
53	28	Double	Bottom	23.8	\	20.12	10.15	0.63	188.09	200.73	100.00	116.95	107.23	6.71	5906.22	6.71	29.42	5.23	3986.94	5.90	4871.73	653.07	763.78	700.30
54	29	Double	Bottom	14.6	//	19.92	10.48	0.63	192.86	205.37	100.00	116.95	107.23	6.47	5620.73	6.47	27.37	5.12	3794.61	5.73	4636.33	676.13	790.75	725.03
55	31	Double	Bottom	42.2	//	20.50	10.40	0.63	196.80	209.68	100.00	116.95	107.23	6.01	6036.71	6.01	28.79	4.64	4075.84	5.24	4960.03	714.43	835.55	766.10
56	34	Double	Bottom	14.6	\	20.30	10.28	0.63	192.51	205.27	100.00	116.95	107.23	6.81	6056.17	6.81	29.50	5.36	4088.08	6.01	4994.29	681.92	797.52	731.24

G

## Domain of Flexural Chord Modulus

Interval	Lowerbound	Upperbound	R <sup>2</sup>
0.25	0.1	0.35	0.999881
	<b>0.125</b>	<b>0.375</b>	<b>0.999890</b>
	0.15	0.4	0.999886
	0.175	0.425	0.999873
	0.2	0.45	0.999851
	0.225	0.475	0.999816
	0.25	0.5	0.999773
	0.275	0.525	0.999731
	0.3	0.55	0.999703
	0.325	0.575	0.999688
	0.35	0.6	0.999678
	0.375	0.625	0.999659
	0.4	0.65	0.999615
	0.425	0.675	0.999541
	0.45	0.7	0.999439
	0.475	0.725	0.999318
	0.5	0.75	0.999193
	0.525	0.775	0.999084
	0.55	0.8	0.998986
	0.575	0.825	0.998886
	0.6	0.85	0.998763
	0.625	0.875	0.998588
	0.65	0.9	0.998370
	0.675	0.925	0.998094
	0.7	0.95	<b>0.997013</b>
	0.725	0.975	<b>0.996371</b>

Interval	Lowerbound	Upperbound	R <sup>2</sup>
0.225	0.1	0.325	0.999896
	<b>0.125</b>	<b>0.35</b>	<b>0.999909</b>
	0.15	0.375	0.999907
	0.175	0.4	0.999902
	0.2	0.425	0.999889
	0.225	0.45	0.999866
	0.25	0.475	0.999831
	0.275	0.5	0.999796
	0.3	0.525	0.999764
	0.325	0.55	0.999745
	0.35	0.575	0.999739
	0.375	0.6	0.999736
	0.4	0.625	0.999718
	0.425	0.65	0.999672
	0.45	0.675	0.999596
	0.475	0.7	0.999495
	0.5	0.725	0.999385
	0.525	0.75	0.999289
	0.55	0.775	0.999215
	0.575	0.8	0.999145
	0.6	0.825	0.999062
	0.625	0.85	0.998949
	0.65	0.875	0.998787
	0.675	0.9	0.998587
	0.7	0.925	0.998340
	0.725	0.95	0.997183
	0.75	0.975	<b>0.996539</b>

Interval	Lowerbound	Upperbound	R <sup>2</sup>
0.2	0.1	0.3	0.999908
	0.125	0.325	0.999924
	<b>0.15</b>	<b>0.35</b>	<b>0.999925</b>
	0.175	0.375	0.999922
	0.2	0.4	0.999918
	0.225	0.425	0.999904
	0.25	0.45	0.999880
	0.275	0.475	0.999850
	0.3	0.5	0.999823
	0.325	0.525	0.999800
	0.35	0.55	0.999789
	0.375	0.575	0.999791
	0.4	0.6	0.999790
	0.425	0.625	0.999772
	0.45	0.65	0.999722
	0.475	0.675	0.999644
	0.5	0.7	0.999548
	0.525	0.725	0.999464
	0.55	0.75	0.999401
	0.575	0.775	0.999354
	0.6	0.8	0.999301
	0.625	0.825	0.999226
	0.65	0.85	0.999124
	0.675	0.875	0.998974
	0.7	0.9	0.998798
	0.725	0.925	0.998586
	0.75	0.95	0.997310
	0.775	0.975	<b>0.996654</b>

Interval	Lowerbound	Upperbound	R <sup>2</sup>
0.175	0.1	0.275	0.999914
	0.125	0.3	0.999938
	<b>0.15</b>	<b>0.325</b>	<b>0.999939</b>
	0.175	0.35	0.999937
	0.2	0.375	0.999936
	0.225	0.4	0.999932
	0.25	0.425	0.999917
	0.275	0.45	0.999895
	0.3	0.475	0.999872
	0.325	0.5	0.999853
	0.35	0.525	0.999836
	0.375	0.55	0.999834
	0.4	0.575	0.999839
	0.425	0.6	0.999839
	0.45	0.625	0.999817
	0.475	0.65	0.999763
	0.5	0.675	0.999685
	0.525	0.7	0.999610
	0.55	0.725	0.999556
	0.575	0.75	0.999521
	0.6	0.775	0.999490
	0.625	0.8	0.999444
	0.65	0.825	0.999378
	0.675	0.85	0.999286
	0.7	0.875	0.999153
	0.725	0.9	0.999007
	0.75	0.925	0.998830
	0.775	0.95	0.997381
	0.8	0.975	<b>0.996667</b>

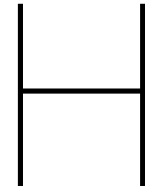
  

Interval	Lowerbound	Upperbound	R <sup>2</sup>
0.15	0.1	0.25	0.999913
	0.125	0.275	0.999948
	<b>0.15</b>	<b>0.3</b>	<b>0.999951</b>
	0.175	0.325	0.999948
	0.2	0.35	0.999948
	0.225	0.375	0.999950
	0.25	0.4	0.999944
	0.275	0.425	0.999929
	0.3	0.45	0.999913
	0.325	0.475	0.999896
	0.35	0.5	0.999882
	0.375	0.525	0.999874
	0.4	0.55	0.999875
	0.425	0.575	0.999883
	0.45	0.6	0.999881
	0.475	0.625	0.999854
	0.5	0.65	0.999796
	0.525	0.675	0.999732
	0.55	0.7	0.999683
	0.575	0.725	0.999656
	0.6	0.75	0.999637
	0.625	0.775	0.999613
	0.65	0.8	0.999573
	0.675	0.825	0.999513
	0.7	0.85	0.999436
	0.725	0.875	0.999325
	0.75	0.9	0.999209
	0.775	0.925	0.999069
	0.8	0.95	0.997347
	0.825	0.975	<b>0.996529</b>

Interval	Lowerbound	Upperbound	R <sup>2</sup>
0.125	0.1	0.225	0.999901
	0.125	0.25	0.999958
	0.15	0.275	0.999960
	0.175	0.3	0.999958
	0.2	0.325	0.999956
	<b>0.225</b>	<b>0.35</b>	<b>0.999961</b>
	<b>0.25</b>	<b>0.375</b>	<b>0.999961</b>
	0.275	0.4	0.999955
	0.3	0.425	0.999943
	0.325	0.45	0.999932
	0.35	0.475	0.999919
	0.375	0.5	0.999913
	0.4	0.525	0.999907
	0.425	0.55	0.999913
	0.45	0.575	0.999920
	0.475	0.6	0.999913
	0.5	0.625	0.999879
	0.525	0.65	0.999829
	0.55	0.675	0.999787
	0.575	0.7	0.999763
	0.6	0.725	0.999752
	0.625	0.75	0.999740
	0.65	0.775	0.999721
	0.675	0.8	0.999684
	0.7	0.825	0.999635
	0.725	0.85	0.999578
	0.75	0.875	0.999486
	0.775	0.9	0.999401
	0.8	0.925	0.999302
	0.825	0.95	0.997157
	0.85	0.975	<b>0.996077</b>

**Figure G.1:** Inspection of domain with the most appropriate approximation with a linear function for the slope of the  $P, v$ -diagram of all tensile tests. The lower- and upperbound are fractions of the maximum load, which is the applied load at failure.



## Raw data - Flexural Test



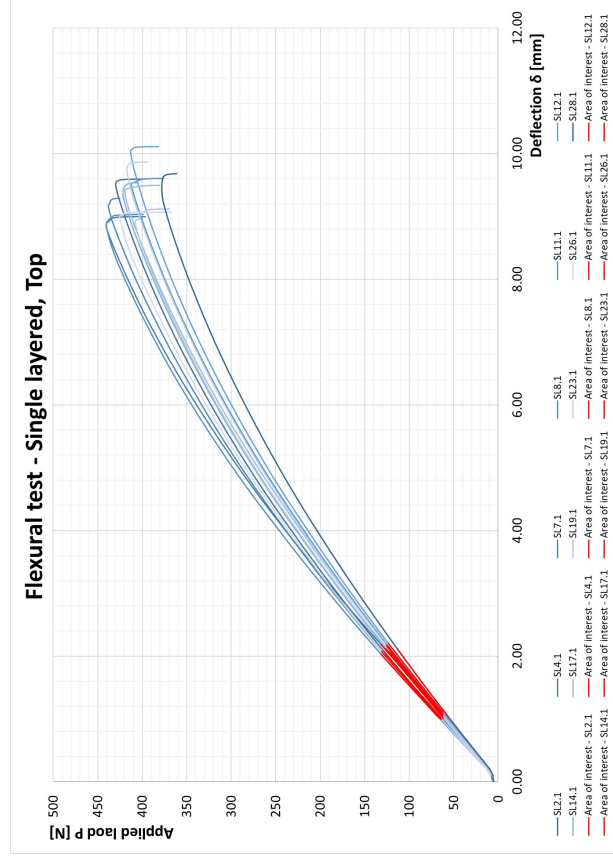


Figure H.1: Recorded data of flexural tests applied to single layered specimens that originates from the upper half of the plate.

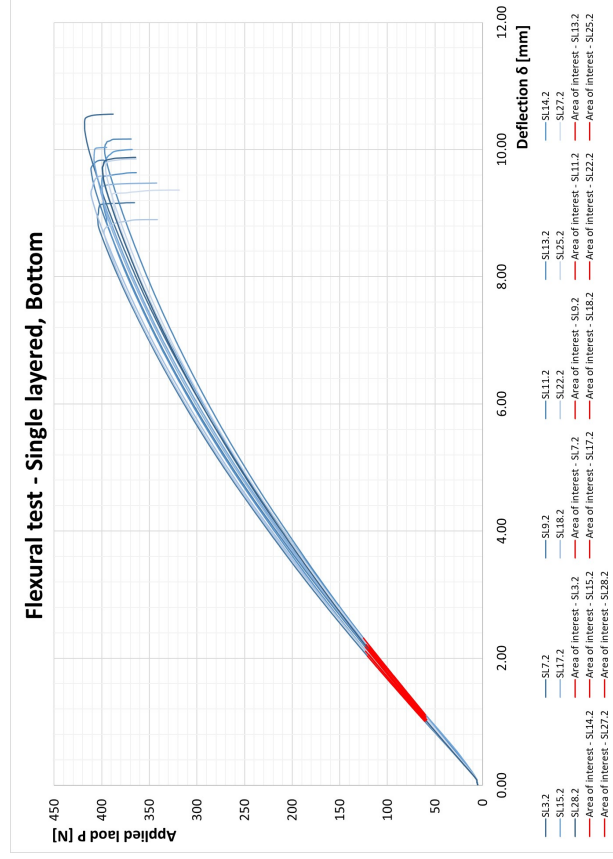


Figure H.2: Recorded data of flexural tests applied to single layered specimens that originates from the lower half of the plate.

Table H.1: Raw data of Flexural Test  
All specimens are single layered.

Test ID	CONDITION				CROSS-SECTIONAL PARAMETERS										RESULTS						
	Plate Number	Specimen type	Vertical position [mm]	Interaction time [s]	Print direction	Averaged width [mm]	Averaged thickness [mm]	$I_{core}$ [mm <sup>4</sup> ]	$I_{rib}$ [mm <sup>4</sup> ]	$A_{rib}$ [mm <sup>2</sup> ]	$z_{rib}$ [mm]	$I_{gross}$ [mm <sup>4</sup> ]	$\delta_{max}$ [mm]	$P_{f,max}$ [N]	$\varepsilon_{f,max}$ [%]	$\sigma_{f,max}$ [Nmm <sup>-2</sup> ]	$\delta_1$ [mm]	$P_1$ [N]	$\delta_2$ [mm]	$P_2$ [N]	$E_{f,chord}$ [MPa]
129	2	Single	Top	n/a	/	48.80	5.41	378.66	0.01	0.69	2.45	582.07	9.50	430.05	2.3334	57.48	1.03	64.82	2.08	128.65	3310.19
130	4	Single	Top	n/a	\	50.04	5.36	375.56	0.01	0.69	2.43	579.90	8.87	440.62	2.1577	58.57	1.09	66.47	2.19	131.86	3272.61
131	7	Single	Top	n/a	/	50.07	5.38	399.57	0.01	0.63	2.46	589.89	9.17	438.16	2.2359	57.39	1.03	66.19	2.08	131.32	3331.39
132	8	Single	Top	n/a	\	50.05	5.53	418.00	0.01	0.69	2.51	636.27	8.87	440.34	2.2243	54.96	1.01	66.05	2.03	131.90	3198.16
133	11	Single	Top	n/a	—	49.89	5.28	352.93	0.01	0.69	2.38	549.40	9.52	412.46	2.2772	56.93	1.07	62.23	2.15	123.32	3278.14
134	12	Single	Top	n/a	—	48.75	5.29	347.83	0.01	0.69	2.39	540.83	10.02	413.21	2.4044	58.07	1.11	62.26	2.21	123.71	3272.82
135	14	Single	Top	n/a	\	49.91	5.36	374.62	0.01	0.69	2.43	578.45	9.35	421.91	2.2744	56.22	1.05	63.37	2.12	126.31	3233.27
136	17	Single	Top	n/a	/	50.00	5.40	384.77	0.01	0.69	2.45	592.12	9.39	419.60	2.3006	55.01	1.08	63.12	2.17	125.76	3071.15
137	19	Single	Top	n/a	/	47.61	5.51	394.44	0.01	0.69	2.50	601.05	8.90	408.03	2.2249	53.79	1.01	61.54	2.06	122.01	3036.31
139	23	Single	Top	n/a	/	50.01	5.49	407.66	0.01	0.69	2.49	622.52	9.76	417.36	2.4311	52.89	1.06	62.74	2.16	125.20	2889.68
140	24	Single	Top	n/a	\	50.11	5.53	418.53	0.01	0.69	2.51	637.07	9.36	432.09	2.3470	53.87	1.10	65.17	2.15	129.12	3029.13
141	26	Single	Top	n/a	\	50.08	5.53	418.21	0.01	0.69	2.51	636.59	9.00	425.48	2.2550	53.08	1.00	63.99	2.02	127.55	3086.50
142	28	Single	Top	n/a	—	46.69	5.46	374.39	0.01	0.69	2.48	572.97	9.46	378.08	2.3456	51.82	1.05	56.96	2.11	113.40	2925.95
143	3	Single	Bottom	n/a	\	50.05	5.44	394.82	0.01	0.69	2.47	605.56	10.42	418.15	2.5713	53.97	1.16	62.77	2.31	125.22	2821.14
144	7	Single	Bottom	n/a	/	50.13	5.43	392.17	0.01	0.69	2.46	602.16	8.94	404.70	2.2005	52.41	1.01	61.11	2.03	121.11	3079.77
145	9	Single	Bottom	n/a	/	48.91	5.48	395.45	0.01	0.69	2.48	604.54	9.69	411.42	2.4068	53.56	1.06	61.85	2.17	123.40	2911.12
146	11	Single	Bottom	n/a	—	48.83	5.24	336.65	0.01	0.69	2.37	525.93	10.00	397.12	2.3773	56.85	1.07	59.58	2.19	118.95	3202.98
147	13	Single	Bottom	n/a	/	49.90	5.36	374.52	0.01	0.69	2.43	578.31	9.50	400.00	2.3112	53.32	1.01	60.16	2.06	119.75	3109.58
148	14	Single	Bottom	n/a	\	49.63	5.35	369.35	0.01	0.69	2.42	570.97	9.71	399.76	2.3561	53.84	1.11	60.14	2.20	119.62	3023.68
149	15	Single	Bottom	n/a	/	50.00	5.44	394.43	0.01	0.69	2.47	604.96	9.85	408.24	2.4291	52.75	1.13	61.25	2.21	122.42	2958.47
150	17	Single	Bottom	n/a	/	50.00	5.45	397.68	0.01	0.69	2.47	609.28	9.33	400.23	2.3074	51.46	1.07	60.28	2.13	119.82	2924.78
151	18	Single	Bottom	n/a	\	50.04	5.45	397.98	0.01	0.69	2.47	609.74	9.32	411.36	2.3033	52.86	1.05	62.22	2.11	123.06	2986.54
152	22	Single	Bottom	n/a	\	50.06	5.53	418.11	0.01	0.69	2.51	636.43	8.69	397.67	2.1788	49.63	1.02	60.05	2.04	119.15	2870.23
153	25	Single	Bottom	n/a	/	50.01	5.40	384.87	0.01	0.69	2.45	592.27	9.71	396.06	2.3796	51.91	1.07	59.69	2.16	118.57	2885.56
154	27	Single	Bottom	n/a	—	49.91	5.38	377.76	0.01	0.69	2.43	582.64	9.28	388.97	2.2629	51.58	1.03	58.67	2.08	116.46	2993.69
155	28	Single	Bottom	n/a	—	49.96	5.39	381.30	0.01	0.69	2.44	587.44	9.71	399.29	2.3726	52.64	1.02	59.95	2.13	119.64	2905.09

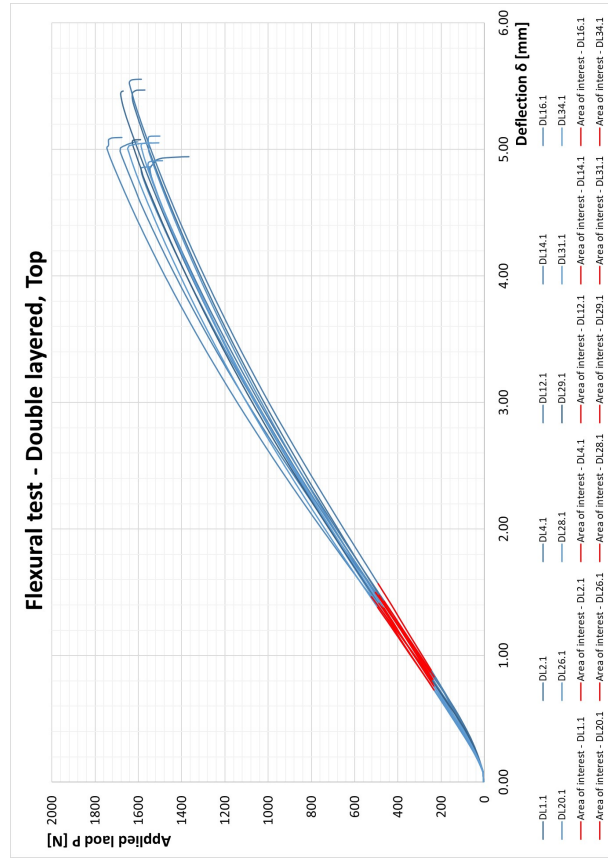


Figure H.3: Recorded data of flexural tests applied to double layered specimens that originates from the upper half of the plate.

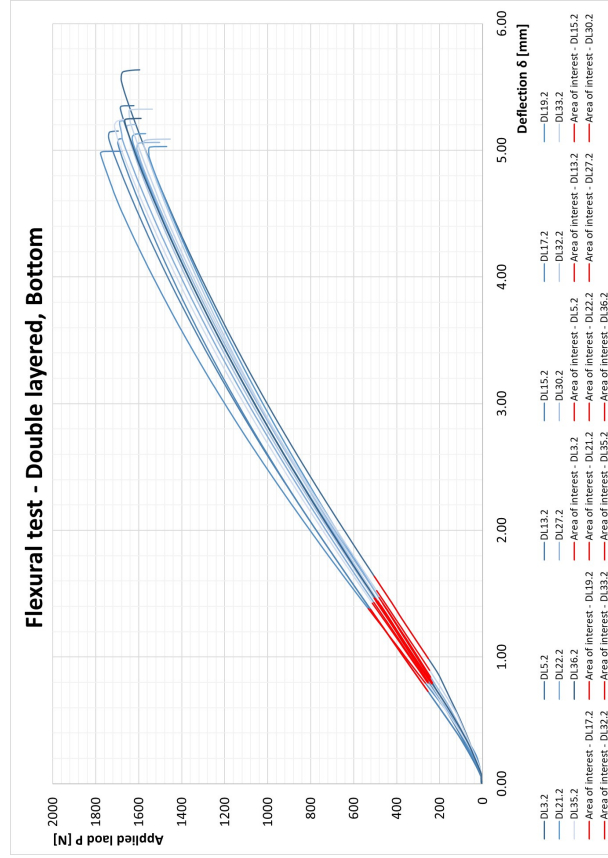


Figure H.4: Recorded data of flexural tests applied to double layered specimens that originates from the lower half of the plate.

Table H.2: Raw data of Flexural Test  
All specimens are double layered.

Test ID	CONDITION										CROSS-SECTIONAL PARAMETERS										RESULTS									
	Plate Number	Specimen type	Vertical position [mm]	Interaction time [s]	Print direction	Averaged width [mm]	Averaged thickness [mm]	$I_{core}$ [mm <sup>4</sup> ]	$I_{fib}$ [mm <sup>4</sup> ]	$A_{fib}$ [mm <sup>2</sup> ]	$z_{fib}$ [mm]	$I_{cross}$ [mm <sup>4</sup> ]	$\delta_{max}$ [mm]	$P_{max}$ [N]	$\epsilon_{f,max}$ [%]	$\sigma_{f,max}$ [N/mm <sup>2</sup> ]	$\delta_1$ [mm]	$P_1$ [N]	$\delta_2$ [mm]	$P_2$ [N]	$E_{f, chord}$ [MPa]									
156	1	Double	Top	318.2	=	50.13	10.43	3724.56	0.01	0.63	4.98	4506.70	5.44	1682.23	2.5713	55.94	0.87	252.48	1.50	503.62	2806.56									
157	2	Double	Top	309	=	50.19	10.34	3628.42	0.01	0.63	4.94	4397.85	5.42	1628.94	2.5411	55.04	0.81	244.53	1.48	487.64	2643.16									
158	4	Double	Top	290.6	\	50.15	10.46	3770.15	0.01	0.63	5.00	4558.57	4.85	1546.77	2.3019	51.03	0.83	232.95	1.43	463.90	2679.30									
159	12	Double	Top	5.4	\	49.96	10.40	3683.64	0.01	0.63	4.97	4459.33	5.53	1642.46	2.6079	55.06	0.88	246.80	1.57	492.12	2551.19									
160	14	Double	Top	34	\	50.14	10.73	4084.82	0.01	0.63	5.13	4914.95	4.99	1684.74	2.4287	52.85	0.88	253.05	1.50	505.05	2635.09									
161	16	Double	Top	14.6	\	50.15	10.86	4258.02	0.01	0.63	5.20	5110.74	5.01	1745.98	2.4695	53.34	0.86	262.50	1.46	523.32	2666.67									
162	20	Double	Top	23.8	\	50.25	10.68	4032.42	0.01	0.63	5.11	4856.33	4.85	1588.58	2.3499	50.20	0.81	238.35	1.43	475.66	2514.35									
163	26	Double	Top	42.2	\	49.98	10.26	3528.49	0.01	0.63	4.90	4283.08	5.07	1554.67	2.3613	53.55	0.76	234.34	1.38	465.34	2763.67									
164	28	Double	Top	23.8	\	49.99	10.25	3515.41	0.01	0.63	4.89	4268.26	4.87	1555.82	2.2659	53.71	0.73	233.59	1.33	466.68	2845.30									
165	29	Double	Top	14.6	\	50.00	10.65	3981.97	0.01	0.63	5.09	4797.77	5.06	1628.36	2.4456	51.96	0.81	244.26	1.41	488.19	2663.52									
166	31	Double	Top	42.2	\	50.04	10.61	3939.61	0.01	0.63	5.08	4750.03	5.00	1649.93	2.4092	52.99	0.77	248.49	1.38	494.80	2686.93									
167	34	Double	Top	14.6	\	49.99	10.28	3543.38	0.01	0.63	4.91	4300.08	5.03	1588.05	2.3438	54.55	0.78	238.79	1.39	475.59	2851.53									
168	3	Double	Bottom	299.8	=	49.44	10.29	3518.28	0.01	0.63	4.91	4268.56	5.57	1682.33	2.5980	58.28	0.99	252.88	1.64	504.69	2875.45									
169	5	Double	Bottom	189.4	\	50.14	10.51	3828.02	0.01	0.63	5.03	4624.15	5.33	1686.33	2.5427	55.11	0.81	254.13	1.46	505.45	2612.84									
170	13	Double	Bottom	42.2	\	50.03	10.60	3923.59	0.01	0.63	5.07	4731.82	5.11	1741.02	2.4564	56.06	0.74	262.14	1.38	521.96	2754.65									
171	15	Double	Bottom	23.8	\	49.96	10.50	3799.95	0.01	0.63	5.02	4591.33	5.06	1697.61	2.4084	55.81	0.73	254.68	1.34	508.84	2859.23									
172	17	Double	Bottom	5.4	\	50.11	10.64	3975.75	0.01	0.63	5.09	4791.38	4.97	1778.33	2.4001	56.75	0.79	267.09	1.38	532.62	2989.19									
173	19	Double	Bottom	34	\	50.15	10.28	3554.90	0.01	0.63	4.91	4314.06	4.99	1554.31	2.3273	53.22	0.79	233.41	1.42	465.72	2712.77									
174	21	Double	Bottom	14.6	\	50.10	10.13	3385.35	0.01	0.63	4.83	4120.75	5.09	1630.95	2.3376	57.61	0.81	245.49	1.44	488.13	2953.90									
175	22	Double	Bottom	5.4	\	49.93	10.51	3811.80	0.01	0.63	5.03	4604.55	5.22	1689.76	2.4895	55.46	0.79	253.90	1.43	506.50	2730.40									
176	27	Double	Bottom	34	\	50.06	10.36	3647.92	0.01	0.63	4.95	4419.32	5.01	1609.43	2.3553	54.25	0.84	242.37	1.47	481.81	2739.03									
177	30	Double	Bottom	5.4	\	50.00	10.19	3446.98	0.01	0.63	4.86	4190.44	5.18	1656.13	2.3951	57.88	0.82	249.41	1.44	496.53	3000.86									
178	32	Double	Bottom	34	\	50.06	10.19	3451.29	0.01	0.63	4.86	4195.67	5.05	1577.72	2.3335	55.07	0.79	237.66	1.40	472.40	2875.13									
179	33	Double	Bottom	23.8	\	49.78	10.55	3844.54	0.01	0.63	5.04	4640.81	5.31	1645.71	2.5393	53.78	0.89	247.02	1.52	493.30	2676.08									
180	35	Double	Bottom	5.4	\	50.05	10.70	4046.96	0.01	0.63	5.12	4871.60	5.19	1713.42	2.5180	54.10	0.80	257.88	1.42	513.67	2665.71									
181	36	Double	Bottom	14.6	\	49.91	10.39	3665.59	0.01	0.63	4.96	4438.57	5.24	1665.72	2.4673	56.04	0.83	250.84	1.46	499.28	2811.93									



# Raw data - Mode II Interlaminar Fracture Toughness Test

**Table 1.1:** Raw data of Mode II Interlaminar Fracture Test  
 The test specimens originate from plates 2, 18, 19, 33 and 34. All 25 specimens are tested 30 days after printing.  
 An 'x' indicates that the subject of interest is applicable to that specific specimen, while a '~' indicates that the subject only applies to the specimen under specific conditions.

Test ID	CONDITION										EXAMINATION										RESULTS									
	Plate Number	Vertical Position [mm]	Print Direction	Interaction time [s]	Averaged Width [mm]	Averaged Height [mm]	Staggered?	Scabrous?	Post-Processed	Delamination?	Applied max load 20mm [N]	Applied max load 40mm [N]	Applied max load 30mm [N]	% $\epsilon_{fc}$ 20mm	% $\epsilon_{fc}$ 40mm	Valid	Slope of $P_c$ -curve 20mm [N mm <sup>-1</sup> ]	Slope of $P_c$ -curve 30mm [N mm <sup>-1</sup> ]	Slope of $P_c$ -curve 40mm [N mm <sup>-1</sup> ]	CC-coefficients m	A	$G_{IIC}$ [Jm <sup>-2</sup> ]								
201	2	17.34		7.5	11.86	10.23			x		250.36	125.19	328.44	25.8%	25.8%		105.43	89.04	68.14	9.27E-08	8.74E-03	1138.79								
204	2	37.09		7.5	12.00	10.32			x		250.39	125.21	325.16	26.4%	26.4%		106.29	92.41	69.31	9.07E-08	8.56E-03	1079.18								
207	2	56.79		7.5	11.87	10.72			x		250.42	125.26	332.71	25.2%	25.2%		109.51	94.70	76.10	7.14E-08	8.59E-03	898.65								
210	2	76.41		7.5	11.93	10.30			x		250.38	125.17	355.14	22.1%	22.1%		115.26	97.90	75.59	8.13E-08	8.02E-03	1160.81								
213	2	96.48		7.5	11.90	10.36			x		250.45	125.20	352.52	22.4%	22.4%		119.45	99.24	73.84	9.25E-08	7.61E-03	1304.08								
216	19	18.61	=	20	12.04	10.11			x		250.42	125.19	289.87	33.2%	33.2%	x	96.88	78.85	57.48	1.27E-07	9.29E-03	1191.77								
219	19	35.11	=	20	12.04	10.12			x		250.42	125.18	323.27	26.7%	26.7%	x	99.30	83.31	59.52	1.21E-07	9.95E-03	1422.98								
222	19	52.11	=	20	11.07	10.11					250.38	125.21	291.00	32.9%	32.9%		97.26	79.86	58.04	1.24E-07	9.24E-03	1285.26								
225	19	69.11	=	20	11.65	10.15			x		250.42	125.17	256.39	42.4%	42.4%		93.67	75.10	54.27	1.38E-07	9.57E-03	1053.87								
228	19	86.11	=	20	12.19	10.09			x		250.39	125.18	280.36	35.4%	35.4%		106.68	88.53	63.22	1.16E-07	8.33E-03	1009.97								
231	18	18.11	=	32.5	12.05	9.93					227.41	113.64	298.83	25.7%	25.7%		99.04	80.59	62.17	1.06E-07	9.37E-03	1059.78								
234	18	35.11	=	32.5	11.78	10.20			x		226.93	113.65	245.12	38.1%	38.2%		97.01	83.47	59.49	1.18E-07	9.14E-03	812.65								
237	18	51.61	=	32.5	11.33	10.14					227.39	113.69	327.76	21.4%	21.4%		103.76	87.52	63.50	1.10E-07	8.63E-03	1410.49								
240	18	67.11	=	32.5	11.15	10.18			x		227.42	113.68	263.92	33.0%	33.0%	~	98.72	82.22	62.13	1.07E-07	9.28E-03	898.08								
243	18	85.11	=	32.5	12.04	10.13			x		227.39	113.65	281.86	28.9%	28.9%	x	107.28	91.42	68.14	9.64E-08	8.46E-03	858.32								
246	34	18.11	=	45	11.92	10.14			x		227.41	113.63	285.66	28.2%	28.1%	x	95.94	76.71	60.20	1.09E-07	9.77E-03	1004.07								
249	34	38.11	=	45	11.79	10.46			x		227.35	113.69	247.91	37.4%	37.4%		101.44	85.00	60.97	1.18E-07	8.78E-03	830.58								
252	34	58.11	=	45	11.80	10.19			x		227.40	113.63	329.96	21.1%	21.1%		110.91	92.79	71.53	8.84E-08	8.34E-03	1100.77								
255	34	78.11	=	45	11.91	10.18			x		227.34	113.67	354.42	18.3%	18.3%		113.90	96.91	73.13	8.79E-08	8.03E-03	1250.86								
258	34	98.11	=	45	11.95	9.99			~		227.43	113.66	321.70	22.2%	22.2%		110.05	90.35	69.28	9.49E-08	8.40E-03	1109.10								
261	33	18.11	=	57.5	11.85	10.15			x		227.40	113.66	301.16	25.3%	25.3%		103.49	83.48	63.39	1.08E-07	8.90E-03	1118.50								
264	33	37.61	=	57.5	11.70	10.46			x		227.35	113.64	304.89	24.7%	24.7%	x	110.12	95.52	67.91	1.03E-07	8.03E-03	1102.15								
267	33	58.11	=	57.5	11.87	10.42			x		227.40	113.63	365.69	17.2%	17.2%		116.91	99.31	76.13	8.19E-08	7.88E-03	1246.35								
270	33	78.11	=	57.5	11.90	10.23			x		227.41	113.66	350.76	18.7%	18.7%		118.83	98.38	75.72	8.51E-08	7.79E-03	1188.34								
273	33	98.11	=	57.5	11.79	9.96			x		227.45	113.65	223.45	46.1%	46.0%		105.91	83.66	60.28	1.27E-07	8.46E-03	728.01								

**Table 12:** Raw data of Mode II Interlaminar Fracture Test  
 The test specimens originate from plates 7, 8, 9, 10 and 11. All 25 specimens are tested 30 days after printing.  
 An 'x' indicates that the subject of interest is applicable to that specific specimen, while a '-' indicates that the subject only applies to the specimen under specific conditions.

Test ID	CONDITION										EXAMINATION										RESULTS									
	Plate Number	Vertical Position [mm]	Print Direction	Interaction time [s]	Averaged Width [mm]	Averaged Height [mm]	Staggered?	Scabrous?	Post-Processed	Delamination?	Applied max load			% $\epsilon_{IIC}$		Valid	Slope of $P_c$ -curve			CC-coefficients			$G_{IIC}$ [ $J\text{mm}^{-2}$ ]							
											20mm [N]	40mm [N]	30mm [N]	20mm	40mm		20 mm [ $N\text{mm}^{-1}$ ]	30mm [ $N\text{mm}^{-1}$ ]	40mm [ $N\text{mm}^{-1}$ ]	m	A									
276	11	18.11	//	7.5	12.04	10.34	x	x			227.43	113.62	293.68	26.7%	26.6%		102.61	84.53	65.41	9.82E-08	9.05E-03	950.26								
279	11	38.11	//	7.5	12.20	10.30	x	x			227.39	113.67	360.96	17.6%	17.6%		112.41	95.76	73.04	8.59E-08	8.17E-03	1238.94								
282	11	58.11	//	7.5	12.16	10.50	x	x			227.39	113.64	320.68	22.3%	22.3%		119.91	98.29	76.69	8.30E-08	7.78E-03	948.23								
285	11	78.11	//	7.5	12.07	10.36	x	x			227.43	113.63	276.44	30.1%	30.0%		110.36	88.95	64.31	1.16E-07	8.12E-03	991.13								
289	11	98.11	//	7.5	11.95	10.36	x	x			227.47	113.68	326.74	21.5%	21.5%		103.50	84.14	67.05	9.22E-08	9.11E-03	1111.76								
292	10	17.11	\	20	11.96	10.37					227.38	113.63	310.61	23.8%	23.8%		105.28	87.90	66.95	9.70E-08	8.74E-03	1056.29								
295	10	37.11	\	20	12.09	10.41			x		227.44	113.63	279.10	29.5%	29.5%	x	101.83	86.28	64.79	1.01E-07	7.96E-03	876.15								
298	10	57.11	\	20	12.02	10.55			x		227.40	113.63	321.46	22.2%	22.2%	x	114.77	91.94	69.20	1.02E-07	7.99E-03	1180.03								
301	10	77.11	\	20	12.14	10.36			x		227.42	113.62	283.92	28.5%	28.5%	x	111.06	92.73	66.86	1.07E-07	8.04E-03	960.92								
304	10	97.11	\	20	12.11	10.37			x		227.39	113.64	262.22	33.4%	33.4%	x	107.50	91.58	65.12	1.10E-07	8.24E-03	841.36								
307	9	17.11	//	32.5	10.67	10.18		x			227.43	113.64	280.51	29.2%	29.2%		83.24	74.04	53.31	1.23E-07	1.07E-02	1228.59								
310	9	37.11	//	32.5	10.69	10.10		x			227.43	113.66	272.32	31.0%	31.0%		83.05	71.30	51.73	1.32E-07	1.08E-02	1235.71								
313	9	57.11	//	32.5	10.83	10.20		x			227.43	113.65	296.03	26.2%	26.2%		94.63	81.58	61.00	1.05E-07	9.61E-03	1148.12								
316	9	77.11	//	32.5	10.83	10.03		x			227.46	113.61	289.10	27.5%	27.5%		90.40	76.41	58.89	1.06E-07	1.02E-02	1100.37								
319	9	97.11	//	32.5	10.58	10.15		x			227.44	113.63	281.50	29.0%	29.0%		89.53	77.73	57.24	1.14E-07	1.01E-02	1154.48								
322	8	18.11	\	45	11.97	10.18		x			227.40	113.63	313.09	23.4%	23.4%		102.18	87.17	66.02	9.62E-08	8.96E-03	1063.57								
325	8	38.11	\	45	12.08	10.38		x			227.38	113.66	321.34	22.3%	22.2%		100.97	85.20	64.92	9.84E-08	9.10E-03	1134.75								
328	8	58.11	\	45	11.91	10.28		x			227.39	113.62	335.32	20.4%	20.4%		112.34	93.12	73.45	8.33E-08	8.34E-03	1061.69								
331	8	78.11	\	45	11.96	10.21		x			227.39	113.64	303.81	24.9%	24.9%		108.75	91.23	65.36	1.10E-07	8.18E-03	1147.76								
334	8	98.11	\	45	11.83	10.21		x			227.43	254.61				103.68	64.22	1.06E-07	8.80E-03	782.74										
336	7	17.61	//	57.5	12.12	10.15		x			227.43	113.63	318.57	22.7%	22.6%		98.89	84.85	57.69	1.32E-07	8.73E-03	1490.80								
339	7	37.61	//	57.5	11.82	10.30		x			227.40	113.62	307.85	24.3%	24.2%		91.65	74.07	59.24	1.05E-07	1.03E-02	1131.54								
342	7	57.61	//	57.5	12.06	10.11		x			227.41	113.63	334.48	20.5%	20.5%		104.78	85.70	63.33	1.12E-07	8.65E-03	1396.82								
345	7	77.61	//	57.5	12.04	10.19		x			227.41	113.63	322.10	22.2%	22.1%		109.16	90.96	68.36	9.77E-08	8.37E-03	1136.52								
348	7	97.61	//	57.5	11.98	10.16		x			227.37	113.68	316.50	22.9%	22.9%		100.79	86.60	67.04	8.95E-08	9.18E-03	1010.26								

**Table 1.3:** Raw data of Mode II Interlaminar Fracture Test  
 The test specimens originate from plates 12, 13, 14, 15 and 16. All 25 specimens are tested 31 days after printing.  
 An 'x' indicates that the subject of interest is applicable to that specific specimen, while a '-' indicates that the subject only applies to the specimen under specific conditions.

Test ID	CONDITION										EXAMINATION										RESULTS									
	Plate Number	Vertical Position [mm]	Print Direction	Interaction time [s]	Averaged Width [mm]	Averaged Height [mm]	Staggered?	Scabrous?	Post-Processed	Delamination?	Applied max load 20mm [N]	Applied max load 40mm [N]	Applied max load 30mm [N]	% $\epsilon_{fbc}$ 20mm	% $\epsilon_{fbc}$ 40mm	Valid	Slope of $p_c$ 20mm [Nmm <sup>-1</sup> ]	Slope of $p_c$ 30mm [Nmm <sup>-1</sup> ]	Slope of $p_c$ 40mm [Nmm <sup>-1</sup> ]	CC-coefficients m	A	$G_{IIC}$ [Jm <sup>-2</sup> ]								
351	12	17.11	∥	57.5	12.00	10.10				x	227.41	113.65	207.38	53.4%	53.4%		96.19	79.44	58.15	1.22E-07	9.37E-03	589.47								
354	12	37.11	∥	57.5	11.98	10.18				x	227.39	113.67	216.24	49.1%	49.1%		106.06	87.35	65.63	1.04E-07	8.62E-03	545.43								
357	12	57.11	∥	57.5	12.02	10.29				x	227.43	113.66	216.10	49.2%	49.2%		108.56	90.16	68.57	9.57E-08	8.47E-03	502.15								
360	12	77.11	∥	57.5	11.94	10.24				x	179.87	89.99	239.68	25.0%	25.1%	x	115.17	93.94	72.64	8.99E-08	8.07E-03	583.97								
363	12	97.11	∥	57.5	11.94	10.24				x	179.93	89.96	208.86	33.0%	33.0%	x	107.20	88.63	66.56	1.02E-07	8.52E-03	501.53								
366	13	17.11	∥	45	10.73	10.01	x		x		227.44	113.67	266.44	32.4%	32.4%		80.37	68.74	51.13	1.28E-07	1.13E-02	1145.80								
369	13	36.61	∥	45	11.98	9.99	x		x		227.41	113.68	314.15	23.3%	23.3%		98.89	81.70	62.32	1.06E-07	9.32E-03	1173.81								
372	13	56.61	∥	45	11.94	10.13	x		x		227.35	113.65	338.34	20.1%	20.1%		111.41	91.86	68.80	9.92E-08	8.19E-03	1283.64								
375	13	76.61	∥	45	12.00	10.02	x		x		227.39	113.65	338.47	20.1%	20.0%		108.90	90.36	69.02	9.44E-08	8.46E-03	1217.25								
378	13	96.61	∥	45	12.01	10.06	x		x		227.40	113.64	339.84	19.9%	19.9%		107.70	89.68	69.08	9.23E-08	8.59E-03	1198.41								
381	14	19.11	∥	32.5	11.98	10.08			x		227.37	113.66	312.51	23.5%	23.5%		103.10	87.01	68.93	8.53E-08	9.09E-03	938.54								
384	14	39.11	∥	32.5	11.97	10.06			x		227.34	113.63	294.58	26.5%	26.5%		100.69	86.67	64.50	1.01E-07	9.01E-03	984.41								
387	14	59.11	∥	32.5	12.03	10.21			x		227.42	113.62	318.84	22.6%	22.6%		112.86	95.31	76.18	7.55E-08	8.33E-03	861.67								
390	14	79.11	∥	32.5	12.05	10.18			x		227.43	113.68	333.38	20.7%	20.7%		110.69	95.31	71.60	8.89E-08	8.23E-03	1106.93								
393	14	99.11	∥	32.5	11.71	10.11			x		227.40	113.65	260.11	34.0%	33.9%	x	99.11	89.11	66.17	9.18E-08	9.11E-03	716.17								
396	15	18.11	∥	20	11.91	10.11			x		227.44	113.66	302.81	25.1%	25.0%		92.33	78.76	58.21	1.14E-07	9.79E-03	1189.58								
399	15	35.11	∥	20	12.05	9.94			x		227.41	113.65	304.60	24.8%	24.8%		97.62	79.32	61.52	1.06E-07	9.53E-03	1103.90								
402	15	52.11	∥	20	11.86	10.15			x		227.45	113.66	339.77	19.9%	19.9%		106.83	88.81	65.95	1.04E-07	8.50E-03	1364.51								
405	15	69.11	∥	20	11.97	10.02			x		227.39	113.66	305.09	24.7%	24.7%		103.47	85.15	65.78	9.82E-08	8.96E-03	1030.39								
408	15	86.11	∥	20	11.99	10.05			x		227.44	113.66	325.24	21.7%	21.7%		109.01	88.11	67.53	9.96E-08	8.49E-03	1187.25								
411	16	18.11	∥	7.5	11.91	10.09			x		227.37	113.62	305.80	24.6%	24.5%		100.06	83.30	64.53	9.77E-08	9.27E-03	1035.78								
414	16	38.11	∥	7.5	11.99	10.24			x		227.41	113.64	335.70	20.4%	20.4%		109.25	89.57	69.83	9.13E-08	8.53E-03	1158.67								
417	16	58.11	∥	7.5	11.96	10.21			x		227.41	113.63	320.60	22.4%	22.3%		108.08	91.61	70.15	8.95E-08	8.52E-03	1038.44								
420	16	78.11	∥	7.5	12.08	10.24			x		227.41	113.64	292.96	26.8%	26.8%		110.47	97.08	67.91	1.04E-07	7.93E-03	995.91								
423	16	98.11	∥	7.5	12.01	10.10			x		227.42	113.69	334.90	20.5%	20.5%		110.45	92.02	71.37	8.80E-08	8.41E-03	1110.28								



**Table 1.4:** Raw data of Mode II Interlaminar Fracture Test  
 The test specimens originate from plates 22, 23, 24, 25 and 26. All 25 specimens are tested 31 days after printing.  
 An 'x' indicates that the subject of interest is applicable to that specific specimen, while a '.' indicates that the subject only applies to the specimen under specific conditions.

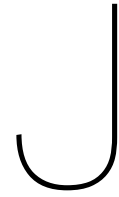
Test ID	CONDITION										EXAMINATION										RESULTS									
	Plate Number	Vertical Position [mm]	Print Direction	Interaction time [s]	Averaged Width [mm]	Averaged Height [mm]	Staggered?	Scabrous?	Post-Processed	Delamination?	Applied max load		% $\epsilon_{fIC}$		Valid	Slope of $p_c$ $\delta$ -curve			CC-coefficients			$\epsilon_{fIC}$ [ $\mu m^{-2}$ ]								
											20mm [N]	40mm [N]	20mm [N]	40mm [N]		20mm [N mm <sup>-1</sup> ]	30mm [N mm <sup>-1</sup> ]	40mm [N mm <sup>-1</sup> ]	m	A										
351	12	17.11	∥	57.5	12.00	10.10					227.41	113.65	207.38	53.4%	53.4%	x	96.19	79.44	58.15	1.22E-07	9.37E-03	589.47								
354	12	37.11	∥	57.5	11.98	10.18					227.39	113.67	216.24	49.1%	49.1%	x	106.06	87.35	65.63	1.04E-07	8.62E-03	545.43								
357	12	57.11	∥	57.5	12.02	10.29					227.43	113.66	216.10	49.2%	49.2%	x	108.56	90.16	68.57	9.57E-08	8.47E-03	502.15								
360	12	77.11	∥	57.5	11.94	10.24					179.87	89.99	239.68	25.0%	25.1%	x	115.17	93.94	72.64	8.99E-08	8.07E-03	583.97								
363	12	97.11	∥	57.5	11.94	10.24					179.93	89.96	208.86	33.0%	33.0%	x	107.20	88.63	66.56	1.02E-07	8.52E-03	501.53								
366	13	17.11	∥	45	10.73	10.01	x	x	x		227.44	113.67	266.44	32.4%	32.4%		80.37	68.74	51.13	1.28E-07	1.13E-02	1145.80								
369	13	36.61	∥	45	11.98	9.99	x	x	x		227.41	113.68	314.15	23.3%	23.3%		98.89	81.70	62.32	1.06E-07	9.32E-03	1173.81								
372	13	56.61	∥	45	11.94	10.13	x	x	x		227.35	113.65	338.34	20.1%	20.1%		111.41	91.86	68.80	9.92E-08	8.19E-03	1283.64								
375	13	76.61	∥	45	12.00	10.02	x	x	x		227.39	113.65	338.47	20.1%	20.0%		108.90	90.36	69.02	9.44E-08	8.46E-03	1217.25								
378	13	96.61	∥	45	12.01	10.06	x	x	x		227.40	113.64	339.84	19.9%	19.9%		107.70	89.68	69.08	9.23E-08	8.59E-03	1198.41								
381	14	19.11	∥	32.5	11.98	10.08					227.37	113.66	312.51	23.5%	23.5%	x	103.10	87.01	68.93	8.53E-08	9.09E-03	938.54								
384	14	39.11	∥	32.5	11.97	10.06					227.34	113.63	294.58	26.5%	26.5%	x	100.69	86.67	64.50	1.01E-07	9.01E-03	984.41								
387	14	59.11	∥	32.5	12.03	10.21					227.42	113.62	318.84	22.6%	22.6%	x	112.86	95.31	76.18	7.55E-08	8.33E-03	861.67								
390	14	79.11	∥	32.5	12.05	10.18					227.43	113.68	333.38	20.7%	20.7%	x	110.69	95.31	71.60	8.89E-08	8.23E-03	1106.93								
393	14	99.11	∥	32.5	11.71	10.11					227.40	113.65	260.11	34.0%	33.9%	x	99.11	89.11	66.17	9.18E-08	9.11E-03	716.17								
396	15	18.11	∥	20	11.91	10.11					227.44	113.66	302.81	25.1%	25.0%	x	92.33	78.76	58.21	1.14E-07	9.79E-03	1189.58								
399	15	35.11	∥	20	12.05	9.94					227.41	113.65	304.60	24.8%	24.8%	x	97.62	79.32	61.52	1.06E-07	9.53E-03	1103.90								
402	15	52.11	∥	20	11.86	10.15					227.45	113.66	339.77	19.9%	19.9%	x	106.83	88.81	65.95	1.04E-07	8.50E-03	1364.51								
405	15	69.11	∥	20	11.97	10.02					227.39	113.66	305.09	24.7%	24.7%	x	103.47	85.15	65.78	9.82E-08	8.96E-03	1030.39								
408	15	86.11	∥	20	11.99	10.05					227.44	113.66	325.24	21.7%	21.7%	x	109.01	88.11	67.53	9.96E-08	8.49E-03	1187.25								
411	16	18.11	∥	7.5	11.91	10.09					227.37	113.62	305.80	24.6%	24.5%	x	100.06	83.30	64.53	9.77E-08	9.27E-03	1035.78								
414	16	38.11	∥	7.5	11.99	10.24					227.41	113.64	335.70	20.4%	20.4%	x	109.25	89.57	69.83	9.13E-08	8.53E-03	1158.67								
417	16	58.11	∥	7.5	11.96	10.21					227.41	113.63	320.60	22.4%	22.3%	x	108.08	91.61	70.15	8.95E-08	8.52E-03	1038.44								
420	16	78.11	∥	7.5	12.08	10.24					227.41	113.64	292.96	26.8%	26.8%	x	110.47	97.08	67.91	1.04E-07	7.93E-03	995.91								
423	16	98.11	∥	7.5	12.01	10.10					227.42	113.69	334.90	20.5%	20.5%	x	110.45	92.02	71.37	8.80E-08	8.41E-03	1110.28								

Test ID	CONDITION										EXAMINATION										RESULTS									
	Plate Number	Vertical Position [mm]	Print Direction	Interaction time [s]	Averaged Width [mm]	Averaged Height [mm]	Staggered?	Scabrous?	Post-Processed	Delamination?	Applied max load 20mm [N]	Applied max load 40mm [N]	Applied max load 30mm [N]	% $\epsilon_{fc}$ 20mm	% $\epsilon_{fc}$ 40mm	Valid	Slope of $P_c$ -curve 20mm [N mm <sup>-1</sup> ]	Slope of $P_c$ -curve 30mm [N mm <sup>-1</sup> ]	Slope of $P_c$ -curve 40mm [N mm <sup>-1</sup> ]	CC-coefficients m	A	$G_{IIC}$ [J m <sup>-2</sup> ]								
507	27	98.11	//		57.5	12.00	10.21																							
510	27	78.11	//		57.5	11.96	10.20																							
513	27	58.11	//		57.5	11.91	10.22																							
516	27	38.11	//		57.5	11.85	10.13																							
519	27	18.11	//		57.5	11.95	10.15																							
522	28	99.11	//		45	10.92	9.89																							
525	28	79.11	//		45	11.86	9.91																							
528	28	59.11	//		45	11.76	10.08																							
531	28	39.11	//		45	11.94	10.21																							
534	28	19.11	//		45	12.02	10.25																							
537	29	98.11	//		32.5	11.99	10.10																							
540	29	78.11	//		32.5	11.91	10.08																							
543	29	59.11	//		32.5	10.61	10.17																							
546	29	39.11	//		32.5	10.61	10.33																							
549	29	19.11	//		32.5	10.56	10.04																							
552	30	97.11	//		20	12.06	10.04																							
555	30	77.11	//		20	11.96	9.94																							
558	30	57.11	//		20	12.13	10.29																							
561	30	37.11	//		20	11.88	10.35																							
564	30	17.11	//		20	11.59	10.15																							
567	31	98.11	//		7.5	11.90	10.04																							
570	31	78.11	//		7.5	11.83	10.13																							
574	31	58.11	//		7.5	11.85	10.26																							
577	31	38.11	//		7.5	11.94	10.58																							
580	31	18.11	//		7.5	11.82	10.28																							

**Table 1.6:** Raw data of Mode II Interlaminar Fracture Test  
 The test specimens originate from plates 27, 28, 29, 30 and 31. All 25 specimens are tested 44 days after printing.  
 An 'x' indicates that the subject of interest is applicable to that specific specimen, while a '~' indicates that the subject only applies to the specimen under specific conditions.

**Table 16:** Raw data of Mode II Interlaminar Fracture Test  
 The test specimens originate from plates 4, 5, 6, 17 and 21. All 30 specimens are tested 50 days after printing.  
 An 'x' indicates that the subject of interest is applicable to that specific specimen, while a '~' indicates that the subject only applies to the specimen under specific conditions.

Test ID	CONDITION				EXAMINATION										RESULTS									
	Plate Number	Vertical Position [mm]	Print Direction	Interaction time [s]	Averaged Width [mm]	Averaged Height [mm]	Staggered?	Scabrous?	Post-Processed	Delamination?	Applied max load [N]		% $c_{flc}$		Valid	Slope of $P_f$ - $\beta$ -curve [N mm <sup>-1</sup> ]			CC-coefficients			$c_{flc}$		
											20mm	40mm	20mm	40mm		20 mm	30mm	40mm	m	n	A			
592	4	13.12	=	420	11.89	10.17			x		181.44	90.75	323.38	14.0%	14.0%		107.28	92.01	69.41	9.15E-08	8.51E-03	1086.50		
595	4	33.12	=	420	12.11	10.07			x	~	199.98	99.92	303.63	19.3%	19.3%		114.13	94.17	73.02	8.74E-08	8.14E-03	898.49		
598	4	53.12	=	420	12.17	10.21			x		199.96	99.97	294.53	20.5%	20.5%	x	117.98	96.36	69.52	1.06E-07	7.59E-03	1019.16		
601	4	73.12	=	420	12.21	10.13			x		199.96	99.91	347.51	14.7%	14.7%		124.84	100.74	79.63	7.98E-08	7.53E-03	1066.21		
605	4	93.12	=	420	12.12	10.18			x		199.96	99.93	375.64	12.6%	12.6%		129.91	102.52	80.31	8.33E-08	7.22E-03	1309.01		
608	6	94.61	//	395	12.08	10.40			x		181.48	90.71	232.81	27.0%	27.0%	x	129.54	105.92	75.05	1.01E-07	6.84E-03	610.31		
611	6	74.61	//	395	12.18	10.43			x		181.42	90.72	260.26	21.6%	21.6%	x	127.76	106.93	81.18	8.02E-08	7.19E-03	601.92		
614	6	54.61	//	395	12.05	10.49			x		181.37	90.68	250.31	23.3%	23.3%	x	126.32	101.83	74.82	9.71E-08	7.16E-03	681.53		
617	6	34.61	//	395	12.00	10.52			x		181.41	90.69	282.64	18.3%	18.3%	x	119.71	101.34	78.42	7.85E-08	7.74E-03	705.55		
620	6	14.61	//	395	11.84	10.65			x		181.38	90.68	309.41	15.3%	15.3%	x	125.55	108.17	82.34	7.51E-08	7.30E-03	820.20		
623	5	95.11	=	407.5	12.08	10.27			x		181.48	90.65	360.78	11.2%	11.2%		128.54	104.32	83.14	7.45E-08	7.34E-03	1083.72		
626	5	75.11	=	407.5	12.16	10.37			x		181.47	90.73	350.34	11.9%	11.9%		131.44	108.08	85.66	7.16E-08	7.15E-03	976.14		
630	5	55.11	=	407.5	12.06	10.38			x		181.43	90.77	287.37	17.7%	17.7%	x	122.14	96.44	74.14	9.32E-08	7.60E-03	861.95		
633	5	35.11	=	407.5	12.11	10.45			x		181.36	90.67	254.26	22.6%	22.6%	x	111.32	83.26	61.71	1.27E-07	8.21E-03	914.45		
636	5	15.11	=	407.5	12.12	10.73			x		181.39	90.67	332.96	13.2%	13.2%		130.70	103.28	76.70	9.55E-08	6.97E-03	1178.44		
639	17	95.11	//	257.5	12.12	10.14	x		x		181.48	90.68	340.43	12.6%	12.6%		118.66	94.55	71.37	9.88E-08	7.75E-03	1275.06		
642	17	75.11	//	257.5	12.13	10.33	x		x		181.42	90.67	346.75	12.2%	12.2%		125.21	96.76	72.16	1.04E-07	7.31E-03	1384.94		
645	17	55.11	//	257.5	12.08	10.45	x		x		181.41	90.69	398.20	9.2%	9.2%		129.56	104.46	79.56	8.59E-08	7.12E-03	1522.25		
648	17	35.11	//	257.5	12.03	10.26	x		x		204.90	102.46	343.24	15.8%	15.8%		114.63	90.19	68.96	1.02E-07	8.08E-03	1344.18		
651	17	15.11	//	257.5	11.80	10.30	x		x		204.89	102.48	339.94	16.1%	16.2%		104.53	90.29	64.37	1.09E-07	8.48E-03	1435.32		
655	21	94.11	//	207.5	12.10	10.22			x		181.39	90.70	251.11	23.2%	23.2%	x	114.28	90.49	66.54	1.11E-07	7.93E-03	783.64		
658	21	74.11	//	207.5	12.12	10.30			x		172.42	86.20	330.22	12.1%	12.1%		119.16	103.53	75.98	8.65E-08	7.55E-03	1050.21		
661	21	54.11	//	207.5	12.15	10.44			x		199.96	99.91	245.40	29.5%	29.5%	x	125.48	103.82	77.18	8.92E-08	7.24E-03	596.56		
664	21	34.11	//	207.5	12.15	10.29			x		187.42	93.67	229.25	29.7%	29.7%	x	118.05	92.33	71.65	9.61E-08	7.91E-03	561.41		
667	21	14.11	//	207.5	11.90	10.23			~		187.43	93.70				108.79		68.45	1.05E-07	7.35E-03	1144.79			
669	21	14.11	//	207.5	11.90	10.23			~		309.32					115.26			1.05E-07	7.35E-03	1144.79			
670	35	98.11	=	32.5	11.97	10.17			x		181.42	90.70	383.85	9.9%	9.9%		124.66	99.80	78.89	8.16E-08	7.55E-03	1355.22		
673	35	78.11	=	32.5	12.08	10.38			x		181.41	90.67	365.49	10.9%	10.9%		130.92	105.62	83.05	7.74E-08	7.16E-03	1154.78		
676	35	58.11	=	32.5	11.96	10.46			x		181.72	90.66	371.46	10.6%	10.6%		128.38	107.08	80.23	8.36E-08	7.10E-03	1302.32		
679	35	38.11	=	32.5	11.92	10.95			x		204.89	102.42	374.65	13.3%	13.3%		127.31	105.90	81.77	7.77E-08	7.28E-03	1235.52		
682	35	18.11	=	32.5	11.94	10.32			x		204.90	102.43	354.02	14.9%	14.9%		111.74	92.92	69.49	9.73E-08	8.16E-03	1378.99		



## Estimation of Characteristic values

The results obtained from the tests provide a good indication of the material behaviour. These results should be compared with the expected outcome. When the testing deviates significantly from the predicted results, this deviation needs to be justified by means of further analysis of the results and/or re-evaluation of the theorem on which the predictions are based. However, if the purpose of the tests is to predict the behaviour of the material of interest subject to different conditions as well, the following aspects must be taken into account.

- the scatter of test data
- statistical uncertainty associated with the number of test
- prior statistical knowledge

The determination of the so-called characteristic value  $X_k$  includes these aspects and is based on the coefficient of variation ( $CV$  or  $V_X$ ), the mean value of the property of interest,  $\mu_X$ , and the sampling factor,  $k_n$ , also indicated as the characteristic fractile factor by the Eurocode<sup>45</sup>.

$$X_d = \frac{\eta_d}{\gamma_m} \cdot \mu_X (1 - k_n V_X) \quad (\text{J.1})$$

$$X_d = \frac{\eta_d}{\gamma_m} \cdot X_k \quad (\text{J.2})$$

$$X_k = \mu_X (1 - k_n V_X) \quad (\text{J.3})$$

### J.1. Coefficient of variation

The scatter of test data is considered in the determination of coefficient of variation. This is ratio of estimated value of the standard deviation,  $s_X$ , and the mean value,  $\mu_X$ , of the properties  $x$ .

$$V_X = \frac{s_X}{\mu_X} \quad (\text{J.4})$$

$$s_X = \sqrt{\frac{\sum_{i=1}^N (x_i - \mu_X)^2}{N - 1}} \quad (\text{J.5})$$

## J.2. The characteristic fractile factor

The characteristic fractile factor depends on the sample length  $N$ . The Eurocode provides table J.1 as a support, which contains values of  $k_n$  related to several sample lengths  $N$ .

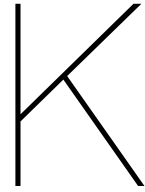
**Table J.1:** Values of  $k_n$  for the 5% characteristic value

$N$	1	2	3	4	5	6	8	10	20	30	$\infty$
$k_n$	2.31	2.01	1.89	1.83	1.80	1.77	1.74	1.72	1.68	1.67	1.64

However, a sample length different from those defined in table J.1 can not be determined by means of interpolation. Any arbitrary value of  $k_n$  can be estimated by direct evaluation of the fractile of the standardised distribution for probability 0.05,  $Z^{31}$ . This 5 percentile value is equal to 1.645.

$$k_n = Z \cdot \sqrt{\frac{N+1}{N}} \quad (\text{J.6})$$

$$k_n = 1.645 \cdot \sqrt{1 + \frac{1}{N}}$$



## Interlaminar Fracture Toughness of various adhesives and resins

**Table K.1:** Mode I and II Interlaminar Fracture Toughness for various adhesives of wood-adhesive joints as reported by Lim et al. <sup>38</sup>

Name	Type of Resin	$G_{Ic}$ [J m <sup>-2</sup> ]	$G_{IIc}$ [J m <sup>-2</sup> ]
AVUT	Water-based vinyl polymer-isocyanates H-3	333.4261	2010.363
EP007	Epoxy polyamine	274.59	2716.44
EP001	Epoxy polyamine	176.52	2108.43
PM200	Epoxy silicon	333.43	2745.86
EsetR	Epoxy polyamine	186.33	2520.31
EC3569	Epoxy polyamine	382.46	5442.69
KU224	Polyurethanes	98.07	1686.74
KU661/2	Polyester (polyol) polyisocyanates	196.13	3638.27
CH18	Polyacetates	235.36	2873.35
Y400	Polyacrylates	686.47	2069.20
SGA	Polyacrylates polyamines	235.36	2490.89
A-α	Poly(α=cyano acrylates)	98.07	9286.90
3000DHX	Poly(α=cyano acrylates)	107.87	3981.50

**Table K.2:** Mode I and II Interlaminar Fracture Toughness of various Resins of Carbon/Epoxy Laminates under the worst curing conditions as reported by Saidpour et al. <sup>58</sup>

Name	Curing conditions	$G_{Ic}$ [J m <sup>-2</sup> ]	$G_{IIc}$ [J m <sup>-2</sup> ]
HTM40/T800	2h at 180°C	n/a	1045
HTM45/IM7	2h at 180°C	n/a	1192
HTM45/T800	2h at 180°C	n/a	1097
MTM49-7/T800	16h at 80°C	n/a	600
MTM49-3/T800	16h at 80°C, post-cured at 97°C	n/a	585.3
LTM545-1/AS4	16h at 60°C, post-cured at 175°C	n/a	868.9

# References

- [1] Waste statistics, 2018. URL <internal-pdf://5.89.66.249/Wastestatistics.pdf>.
- [2] Mukesh K. Agarwala, Vikram R. Jamalabad, Noshir A. Langrana, Ahmad Safari, Philip J. Whalen, and Stephen C. Danforth. Structural quality of parts processed by fused deposition. *Rapid Prototyping Journal*. *Rapid Prototyping Journal*, 2(4):4–19, 1996.
- [3] Sung-Hoon Ahn, Michael Montero, Dan Odell, Shad Roundy, and Paul K Wright. Anisotropic material properties of fused deposition modeling ABS. *Rapid prototyping journal*, 8(4):248–257, 2002. ISSN 1355-2546. URL <internal-pdf://87.15.101.226/AnisotropicmaterialpropertiesofFDMABS.pdf>.
- [4] Nahal Aliheidari, Rajasekhar Tripuraneni, Amir Ameli, and Siva Nadimpalli. Fracture resistance measurement of fused deposition modeling 3D printed polymers. *Polymer Testing*, 60:94–101, 2017. ISSN 0142-9418. URL <internal-pdf://0085556598/FractureresistancemeasurementofFDM3Dprin.pdf>.
- [5] American Society for Testing Materials International. D6115-97(2011): Standard Test Method for Mode I Fatigue Delamination Growth Onset of Unidirectional Fiber Reinforced Polymer Matrix Composites, 2011.
- [6] American Society for Testing Materials International. D5528-13: Standard Test Method for Mode I Interlaminar Fracture Toughness of Unidirectional Fiber-Reinforced Polymer Matrix Composites, 2013. ISSN 1885-3137.
- [7] American Society for Testing Materials International. D6671/D6671M-13e1 - Standard Test Method for Mixed Mode I-Mode II Interlaminar Fracture Toughness of Unidirectional Fiber Reinforced Polymer Matrix Composites, 2013. ISSN 1468-0009.
- [8] American Society for Testing Materials International. D638-14: Standard test method for tensile properties of plastics, 2014. ISSN 01413910.
- [9] American Society for Testing Materials International. D7905/D7905M-14: Standard Test Method for Determination of the Mode II Interlaminar Fracture Toughness of Unidirectional Fiber-Reinforced Polymer, 2014. ISSN 0028646X.
- [10] American Society for Testing Materials International. D7264/D7264M-15: Standard Test Method for Flexural Properties of Polymer Matrix Composite Materials, 2015. ISSN 1098-4275.
- [11] American Society for Testing Materials International. D3039/D3039M-17: Standard Test Method for Tensile Properties of Polymer Matrix Composite Materials, 2017.
- [12] American Society for Testing Materials International. D790-17: Standard Test Methods for Flexural Properties of Unreinforced and Reinforced Plastics and Electrical Insulating Materials, 2017.
- [13] Paweł Krzysztof Baran. *Methodology and Tools for Test-ing, Numerical Analysis and De- sign of the 3D Printed Moulds*. Master's thesis, Delft University of Technology, Delft, 2016.
- [14] Céline T Bellehumeur, M K Bisaria, and J Vlachopoulos. An experimental study and model assessment of polymer sintering. *Polymer Engineering & Science*, 36(17):2198–2207, 1996. ISSN 1548-2634. URL <internal-pdf://187.221.253.2/Anexperimentalstudyandmodelassessmentof.pdf>.
- [15] Céline T. Bellehumeur, Longmei Li, Qian Sun, and Peihua Gu. Modeling of bond formation between polymer filaments in the fused deposition modeling process. *Journal of Manufacturing Processes*, 6(2):170–178, 2004. ISSN 1526-6125. URL <internal-pdf://89.78.14.209/ModelingofBondformationbetweenpolymerfil.pdf>.

- [16] Anna Bellini and Selçuk Güçeri. Mechanical characterization of parts fabricated using fused deposition modeling. *Rapid Prototyping Journal*, 9(4):252–264, 2003. ISSN 13552546. doi: 10.1108/13552540310489631.
- [17] Bjorn Berge. *The ecology of Buildings Material*. Number 11.06.2015. 2009. ISBN ISBN: 978-1-85617-537-1.
- [18] M. Bertoldi, M.A. Yardimci, C.M. Pistor, Selçuk I. Güçeri, and G. Sala. Mechanical characterization of parts processed via fused deposition. *Solid Freeform Fabrication Proceedings, Austin, TX*, pages 557–565, 1998.
- [19] Dat Bui. *Accelerated ageing - An experimental study on the weathering behaviour of a 3D printed polymer facade element*. Master's thesis, Delf University of Technology, Delft, 2005.
- [20] Richard A. Buswell, R.C. Soar, Alistair G.F. Gibb, and A. Thorpe. Freeform construction: mega-scale rapid manufacturing for construction. *Automation in construction*, 16(2):224–231, 2007. ISSN 0926-5805. URL <internal-pdf://0896673345/FreeformConstruction-Mega-scaleRapidManuf.pdf>.
- [21] R.S. Crockett and P.D. Calvert. The Liquid-to-Solid transition in Stereodeposition Techniques. pages 257–264, 1997.
- [22] Barry D. Davidson and Xuekun Sun. Geometry and Data Reduction Recommendations for a Standardized End Notched Flexure Test for. *Journal of ASTM International*, 3(9):1–19, 2011.
- [23] Dylan Drotman, Mamadou Diagne, Robert Bitmead, and Miroslav Krstic. *Control-Oriented Energy-Based Modeling of a Screw Extruder Used for 3D Printing*. oct 2016. doi: 10.1115/DSCC2016-9651.
- [24] Matthias Faes, Brecht van Hooreweder, Yueqi Wang, Pascal Lava, and David Moens. Variability in Mechanical Properties of ABS parts produced by Fused Deposition Modelling. *Proceedings of the 2015 NAFEMS World Congress*, (October 2017), 2015.
- [25] Matthias Faes, Eleonora Ferraris, and David Moens. Influence of inter-layer cooling time on the quasi-static properties of ABS components produced via fused deposition modelling. *Procedia CIRP*, 42:748–753, 2016. ISSN 2212-8271. URL <internal-pdf://176.235.179.171/InfluenceofInter-layerCoolingtimeontheQ.pdf>.
- [26] Anthony C. Fischer-Cripps. Linear Elastic Fracture Mechanics. In Frederick F. Ling, editor, *Introduction to Contact Mechanics*, chapter 2, pages 31–48. Springer Science+Business Media, New South Wales, 2 edition, 2007. ISBN 978-0-387-68187-0. doi: 10.1007/978-1-4419-9872-9\_1.
- [27] Monika G. Garrell, Albert J. Shih, Edgar Lara-Curzio, and Ronald O. Scattergood. Finite-element analysis of stress concentration in ASTM D 638 tension specimens. *Journal of testing and evaluation*, 31(1):52–57, 2003. ISSN 0090-3973.
- [28] Peihua Gu and Longmei Li. Fabrication of biomedical prototypes with locally controlled properties using FDM. *CIRP Annals-Manufacturing Technology*, 51(1):181–184, 2002. ISSN 0007-8506. URL <internal-pdf://0986912866/FabricationofBiomedicalPrototypeswithLoca.pdf>.
- [29] Pavan Kumar Gurralla and Srinivasa Prakash Regalla. Part strength evolution with bonding between filaments in fused deposition modelling: This paper studies how coalescence of filaments contributes to the strength of final FDM part. *Virtual and Physical Prototyping*, 9(3):141–149, 2014. ISSN 17452767. doi: 10.1080/17452759.2014.913400.
- [30] Nevin Hill and Mehrdad Haghi. Deposition direction-dependent failure criteria for fused deposition modeling polycarbonate. *Rapid Prototyping Journal*, 20(3): 221–227, 2014. ISSN 1355-2546. URL <internal-pdf://151.223.92.36/Depositiondirection-dependentfailurecriteri.pdf>.



- [31] Milan Holický, Karel Jung, and Miroslav Sýkora. Estimation of concrete strength from small samples. In Luc; Taerwe and Dirk Proske, editors, *5th International Probabilistic Workshop*, pages 233–240, Ghent, 2007.
- [32] Charles W. Hull. United States Patent - Apparatus for Production of Three-Dimensional Objects by Stereolithography, 1984.
- [33] Melvin F. Kanninen and Carl H. Popelar. Linear elastic fracture mechanics. In *Advanced fracture mechanics*, pages 138–171. Oxford University Press, Oxford, 1985. ISBN 0195035321.
- [34] Hideo Kodama. Automatic method for fabricating a three-dimensional plastic model with photo-hardening polymer. *Review of Scientific Instruments*, 52(11):1770–1773, 1981. ISSN 0034-6748. doi: 10.1063/1.1136492.
- [35] Charoula Kousiatza and Dimitris Karalekas. In-situ monitoring of strain and temperature distributions during fused deposition modeling process. *Materials & Design*, 97:400–406, 2016. ISSN 0264-1275. URL <internal-pdf://0390267212/In-situmonitoringofstrainandtemperature.pdf>.
- [36] Nathalie Labonnote, Anders Rønnquist, Bendik Manum, and Petra Rüter. Additive construction: State-of-the-art, challenges and opportunities. *Automation in Construction*, 72:347–366, 2016. ISSN 09265805. doi: 10.1016/j.autcon.2016.08.026. URL <http://dx.doi.org/10.1016/j.autcon.2016.08.026>.
- [37] S. Lim, R.A. Buswell, T.T. Le, S.A. Austin, A.G.F. Gibb, and T. Thorpe. Developments in construction-scale additive manufacturing processes. *Automation in Construction*, 21(1):262–268, 2012. ISSN 09265805. doi: 10.1016/j.autcon.2011.06.010.
- [38] Won Woo Lim, Yasunori Hatano, and Hiroshi Mizumachi. Fracture toughness of adhesive joints. I. Relationship between strain energy release rates in three different fracture modes and adhesive strengths. *Journal of applied polymer science*, 52(7):967–973, 1994. ISSN 0021-8995.
- [39] Farhad Asgari Mehrabadi and Mohammadreza Khoshravan. Mode III interlaminar fracture and damage characterization in woven fabric-reinforced glass/epoxy composite laminates. *Journal of Composite Materials*, 47(13):1583–1592, 2013. ISSN 00219983. doi: 10.1177/0021998312449770.
- [40] Michael Montero, Shad Roundy, Dan Odell, Sung-Hoon Ahn, and Paul K. Wright. Material characterization of fused deposition modeling (FDM) ABS by designed experiments. *Society of Manufacturing Engineers*, 10, 2001. URL <internal-pdf://178.26.178.129/MaterialCharacterizationofFDMABSbyDesign.pdf>.
- [41] Lisanne Mulders. *High quality recycling of construction and demolition waste in the Netherlands Lisanne Mulders*. Master's thesis, Utrecht University, Utrecht, 2013.
- [42] Nederlands Normalisatie-Instituut. NEN-EN-ISO 527-4: Plastics - Determination of tensile properties - Part 4: Test conditions for isotropic and orthotropic fibre-reinforced plastic composites, 1997.
- [43] Nederlands Normalisatie-Instituut. NEN-EN-ISO 14125: Fibre-reinforced plastic composites - Determination of flexural properties, 1998.
- [44] Nederlands Normalisatie-Instituut. NEN-ISO 15024: Fibre-reinforced plastic composites - Determination of mode I interlaminar fracture toughness, GIC, for unidirectionally reinforced materials, 2002.
- [45] Nederlands Normalisatie-Instituut. NEN-EN 1990: Basis of structural design, 2002.
- [46] Nederlands Normalisatie-Instituut. NEN-EN-ISO 527-5: Plastics - Determination of tensile properties - Part 5: Test conditions for unidirectional fibre-reinforced plastic composites, 2009.

- [47] Nederlands Normalisatie-Instituut. NEN-EN-ISO 178: Plastics - Determination of flexural properties, 2010.
- [48] Nederlands Normalisatie-Instituut. NEN-EN-ISO 527-1: Plastics - Determination of tensile properties - Part 1: General principles, 2012.
- [49] Nederlands Normalisatie-Instituut. NEN-ISO 15114: Fibre-reinforced plastic composites - Determination of the mode II fracture resistance for unidirectionally reinforced materials using the calibrated end-loaded split (C-ELS) test and an effective crack length approach, 2014.
- [50] Marko Pavlovic and Fruzsina Csillag. Lecture Notes FRP - Fibres , resins and cores, 2018.
- [51] Stephan F.G. Peulen. *Vergroten knik gedrag van een stalen staaf door inzet van 3D geprint materiaal*. Bachelor's thesis, Delft University of Technology, 2015.
- [52] Walter D. Pilkey. Stress concentration. In *Formulas for stress, strain, and structural matrices*, chapter 6, pages 255–271. John Wiley & Sons, Inc., Charlottesville, 2 edition, 2005. ISBN 0-471-03221-2.
- [53] P. Robinson and D.Q. Song. The Development of an Improved Mode III Delamination Test for Composites. *Composite Science and Technology*, 52:217–233, 1994.
- [54] J.F. Rodriguez, J.P. Thomas, and J.E. Renaud. Characterization of the mesostructure of styrene materials. *Rapid Prototyping Journal*, 6(3):175–185, 2000.
- [55] José F. Rodríguez, James P. Thomas, and John E. Renaud. Maximizing the strength of fused-deposition ABS plastic parts. In *Tenth Solid Freeform Fabrication Symposium (SFF), Austin, TX, Aug*, pages 9–11, 1999. URL [internal-pdf://253.50.156.194/MaximizingtheStrengthofFused-DepositionA.pdf](http://internal-pdf://253.50.156.194/MaximizingtheStrengthofFused-DepositionA.pdf).
- [56] Jose F. Rodríguez, James P. Thomas, and John E. Renaud. Mechanical behavior of acrylonitrile butadiene styrene (ABS) fused deposition materials. Experimental investigation. *Rapid Prototyping Journal*, 7(3):148–158, 2001.
- [57] David Roylance. Introduction to Fracture Mechanics, 2001.
- [58] Hossein Saidpour, Mehdi Barikani, and Mutlu Sezen. Mode-II Interlaminar Fracture Toughness of Carbon/Epoxy Laminates. *Iranian Polymer Journal*, 12(5):389–400, sep 2003. URL <http://hdl.handle.net/10552/1033>.
- [59] Piet J.G. Schreurs. Fracture Mechanics, 2012. ISSN 00255564. URL <http://doi.wiley.com/10.1002/9781118097298.weoc096>.
- [60] Jonathan E. Seppala, Seung Hoon Han, Kaitlyn E. Hillgartner, Chelsea S. Davis, and Kalman B. Migler. Weld formation during material extrusion additive manufacturing. *Soft Matter*, 13(38):6761–6769, 2017. ISSN 17446848. doi: 10.1039/c7sm00950j. URL <http://dx.doi.org/10.1039/C7SM00950J>.
- [61] Anoop Kumar Sood, R.K. Ohdar, and S.S. Mahapatra. Parametric appraisal of mechanical property of fused deposition modelling processed parts. *Materials and Design*, 31(1):287–295, 2010. ISSN 02641275. doi: 10.1016/j.matdes.2009.06.016. URL <http://dx.doi.org/10.1016/j.matdes.2009.06.016>.
- [62] Martin Spoerk, Florian Arbeiter, Hrvoje Cajner, Janak Sapkota, and Clemens Holzer. Parametric optimization of intra- and inter-layer strengths in parts produced by extrusion-based additive manufacturing of poly (lactic acid). *Journal of Applied Polymer Science*, 134(41), 2017. ISSN 1097-4628. URL [internal-pdf://231.250.127.43/Parametricoptimizationofintra-andinter-la.pdf](http://internal-pdf://231.250.127.43/Parametricoptimizationofintra-andinter-la.pdf).
- [63] Duncan Stewart. Technology, Media, and Telecommunications Predictions 2019. *Technology, Media, and Telecommunications Predictions*, pages 70–77, 2018. URL <file:///C:/Users/niels/Downloads/DI{ }TMT-predictions{ }2019.pdf>.

- [64] Stratasys. Legal Documents, 2018. URL <https://www.stratasys.com/legal/legal-information>.
- [65] Q. Sun, G.M. Rizvi, Céline T. Bellehumeur, and P. Gu. Experimental study of the cooling characteristics of polymer filaments in FDM and impact on the mesostructures and properties of prototypes. In *Proceedings of the 14th Solid Freeform Fabrication Symposium*, pages 170–178, 2003. URL <internal-pdf://0338683788/ExperimentalStudyoftheCoolingCharacterist.pdf>.
- [66] Q. Sun, G. M. Rizvi, C. T. Bellehumeur, and P. Gu. Effect of processing conditions on the bonding quality of FDM polymer filaments. *Rapid Prototyping Journal*, 14(2):72–80, 2008. ISSN 13552546. doi: 10.1108/13552540810862028.
- [67] András Szekrényes. The influence of crack length and delamination width on the mode-III energy release rate of laminated composites. *Journal of Composite Materials*, 45(3):279–294, 2011. ISSN 00219983. doi: 10.1177/0021998310376097.
- [68] James P. Thomas and José F. Rodríguez. Modeling the fracture strength between fused deposition extruded roads. In *Proceedings of the 11th Solid Freeform Fabrication Symposium*, pages 16–23, 2000. URL <internal-pdf://223.170.78.198/ModelingtheFractureStrengthBetweenFused-D.pdf>.
- [69] Angel R. Torrado and David A. Roberson. Failure analysis and anisotropy evaluation of 3D-printed tensile test specimens of different geometries and print raster patterns. *Journal of Failure Analysis and Prevention*, 16(1):154–164, 2016. ISSN 1547-7029. URL <internal-pdf://202.148.4.31/FailureAnalysisandAnisotropyEvaluationof.pdf>.
- [70] Brian N. Turner and Scott A. Gold. A review of melt extrusion additive manufacturing processes: II. Materials, dimensional accuracy, and surface roughness. *Rapid Prototyping Journal*, 21(3):250–261, 2015. ISSN 1355-2546.
- [71] Brian N. Turner, Robert Strong, and Scott A. Gold. A review of melt extrusion additive manufacturing processes: I. Process design and modeling. *Rapid Prototyping Journal*, 20(3):192–204, 2014. ISSN 1355-2546.
- [72] United Nations Environment Programme. Buildings and Climate Change. *Revue Internationale de la Croix-Rouge*, 2009. ISSN 00353361. doi: 10.1017/S0035336100129600.
- [73] Frans van der Meer. Lecture Notes FRP - Materials and Failure Analysis, 2016.
- [74] Arnoud van der Veen. *The structural feasibility of 3D-printing houses using printable polymers*. Master thesis, Delft University of Technology, Delft, 2014.
- [75] V. Vega, J. Clements, T. Lam, A. Abad, B. Fritz, N. Ula, and Omar S. Es-Said. The effect of layer orientation on the mechanical properties and microstructure of a polymer. *Journal of materials engineering and performance*, 20(6):978–988, 2011. ISSN 1059-9495. URL <internal-pdf://144.253.197.31/TheEffectofLayerOrientationontheMechani.pdf>.
- [76] Chun W. Wang. Introduction to fracture mechanics, 1996.
- [77] Jiayi Wang. *Optimisation methodology of large-scale 3D printing using recycled plastics*. Master's thesis, Delft University of Technology, Delft, 2018.
- [78] Tian Ming Wang, Jun Tong Xi, and Ye Jin. A model research for prototype warp deformation in the FDM process. *International Journal of Advanced Manufacturing Technology*, 33(11-12):1087–1096, 2007. ISSN 02683768. doi: 10.1007/s00170-006-0556-9.
- [79] Terry Wohlers and Tim Gornet. History of additive manufacturing. *Wohlers report*, 24(2014):118, 2014.

- [80] Peng Wu, Jun Wang, and Xiangyu Wang. A critical review of the use of 3-D printing in the construction industry. *Automation in Construction*, 68:21–31, 2016. ISSN 09265805. doi: 10.1016/j.autcon.2016.04.005. URL <http://dx.doi.org/10.1016/j.autcon.2016.04.005>.
- [81] M. Atif Yardimci, Takeshi Hattori, Selcuk I. Guceri, and Stephen C. Danforth. Thermal Analysis of Fused Deposition. In *Solid Freeform Fabrication Symposium Proceedings*, pages 689–698, Austin, 1997.
- [82] Alan T. Zehnder. *Fracture Mechanics*, volume 62. Springer, Ithaca, 2012. ISBN 9783642246371. doi: 10.1007/978-94-007-2595-9.
- [83] Y. Zhang and K. Chou. A parametric study of part distortions in fused deposition modelling using three-dimensional finite element analysis. *Proceedings of the Institution of Mechanical Engineers, Part B: Journal of Engineering Manufacture*, 222(8):959–968, 2008. ISSN 0954-4054.

# List of Figures

1.1	Full printed planters	2
1.2	Hybrid Floor	2
1.3	Staircase created with printed formwork	2
1.4	Façade designed by DUS. Archtiects	3
1.5	Façade is composed of cells	3
2.1	Sketch of a system for stereolithography in the patent of Charles Hull <sup>32</sup>	5
2.2	The core elements of the printhead <sup>23</sup>	6
2.3	Die swelling of the extruded material <sup>71</sup>	6
2.4	Insufficient volumetric flow rate at the corners	7
2.5	Insufficient volumetric flow rate at the joint	7
2.6	Composition of 3D printed structure <sup>15</sup>	8
2.7	The mesostructure of an additively manufactured product	8
2.8	Skewed Configuration <sup>54</sup>	8
2.9	Aligned Configuration <sup>54</sup>	8
2.10	The bond formation between two adjacent filaments <sup>66</sup>	9
2.11	The thermal development at the centre of a single printed bead over time for two different conditions as reported by Rodriguez et al. <sup>54</sup>	10
2.12	The thermal gradient within a single printed bead for $T_L = 285^\circ\text{C}$ and $T_E = 55^\circ\text{C}$ at approximately 0.18s after extrusion as reported by Rodriguez et al. <sup>54</sup>	10
2.13	Different gap sizes within the print. <sup>65</sup>	10
2.14	The thermal history for three extrusion temperatures <sup>66</sup>	11
2.15	The thermal history for three envelope temperatures <sup>66</sup>	11
2.16	The thermal history for two print heights <sup>66</sup>	11
2.17	The thermal history for two print patterns. <sup>66</sup>	11
2.18	The build location of each printed structure <sup>66</sup>	11
2.19	The thermal history for three different build locations <sup>66</sup>	11
2.20	The extrusion of a filament reheats the material in the layers below.	12
2.21	Front view of a full-print façade designed by DUS. Archtiects and produced by Aectual	13
2.22	Clos-up of the full-print façade.	13
2.23	Close-up of a joint of the full-print façade. The intralayer bonds within the joint are clearly visible.	13
3.1	Test sample to assess the print quality	14
3.2	The curved surface of the test sample	14
3.3	The structure of a fibre reinforce composite <sup>73</sup>	15
3.4	Specimen as prescribed by ISO527-4 <sup>42</sup>	17
3.5	Three fracture modes (after Kanninen and Popelar <sup>33</sup> ).	19
3.6	Unloading due to fracture (after Roylance <sup>57</sup> ).	19
3.7	Load-displacement diagram for a solid body with crack area $A_0$ .	20
3.8	Load-displacement diagram for a solid body with an increased crack area $A + dA$ .	20
3.9	Evaluation of the energy balance on an infinite small domain $dq$ .	22
3.10	Evaluation of the energy balance on an infinite small domain $dP$ .	22
3.11	Load displacement diagram of a linear elastic material.	22
3.12	Modified split-cantilver beam (MSCB) specimen designed for the determination of $G_{IIc}$ <sup>53</sup> .	23
3.13	Edge-crack torsion (ECT) specimen designed for the determination of $G_{IIc}$ <sup>39</sup> .	23
3.14	Double cantilever beam (DCB) specimen designed for the determination of $G_{Ic}$ <sup>6</sup> .	24
3.15	End-loaded split (ELS) specimen designed for the determination of $G_{IIc}$ <sup>49</sup> .	25
3.16	End notched flexure (ENF) specimen designed for the determination of $G_{IIc}$ <sup>9</sup> .	25

4.1	KamerMaker . . . . .	27
4.2	Static and Track Robot . . . . .	27
4.3	A brim of compressed layers and warping failure. . . . .	29
4.4	Fixation of the brim. . . . .	29
4.5	Distortion within the printed plate due to the corner. . . . .	29
4.6	The distribution of a single pellet with red colouring agent along the print path of a panel with a surface area of 2.45 x 0.40 m <sup>2</sup> . . . . .	30
4.7	1% UV+Antistatic . . . . .	31
4.8	5% Colour . . . . .	31
4.9	47% PP+GF . . . . .	31
4.10	47% HDPE . . . . .	31
4.11	Insufficient molten pellets . . . . .	31
4.12	Degradation of the polymers . . . . .	31
4.13	Plane fabricated by KamerMaker 2 for preliminary test . . . . .	31
4.14	Plane fabricated by Static Robot for final test . . . . .	31
4.15	Global and local axis . . . . .	32
4.16	Vertical position of tensile and flexural specimens . . . . .	33
4.17	Vertical position of delamination specimens . . . . .	33
4.18	The printed single layered geometry . . . . .	33
4.19	The printed double layered geometry . . . . .	33
4.20	The designed gap within the geometry for delamination specimens. . . . .	34
4.21	Delamination specimens with tracing marks. . . . .	34
5.1	Excluded tensile specimens. . . . .	35
5.2	Cracked tensile specimens. . . . .	36
5.3	Composition of the cross-section. . . . .	37
5.4	Shift in crack in the flexural specimen . . . . .	41
5.5	Failure due to pure delamination . . . . .	43
5.6	Failure due to cracking . . . . .	43
5.7	Discontinuity at the crackfront . . . . .	44
5.8	Post-processing has affected the material at the crackfront. . . . .	44
5.9	Schematised joint within a façade panel designed by DUS. Architects . . . . .	49
A.1	The Mechanical properties of Polypropylene (PP). . . . .	57
A.2	The Mechanical properties of High Density Polyethylene (HDPE). . . . .	58
B.1	Print pattern for single layered geometries . . . . .	60
B.2	Print pattern for double layered geometries . . . . .	61
B.3	Print pattern for delamination geometries . . . . .	62
C.1	Composition of the cross-section . . . . .	63
C.2	The determination of the centre of gravity of a rib . . . . .	65
C.3	The determination of the moment of inertia about the local z-axis of a rib . . . . .	66
C.4	Shift of the local axis towards the centroid of the rib . . . . .	67
D.1	Numerical representation of a fillet: $(x - a)^2 + (y - b)^2 = R^2$ . . . . .	69
D.2	Numerical representation of the narrow section and the fillets of a tensile specimen. . . . .	70
E.1	Inspection of domain with the most appropriate approximation with a linear function for the slope of the $P,u$ -diagram of all tensile tests. The lower- and upperbound are fractions of the maximum load, which is the applied load at failure. . . . .	74
F.1	Recorded data of tensile tests applied to single layered specimens that originates from the upper half of the plate. . . . .	76
F.2	Recorded data of tensile tests applied to single layered specimens that originates from the lower half of the plate. . . . .	76

---

F.3	Recorded data of tensile tests applied to double layered specimens that originates from the upper half of the plate. . . . .	78
F.4	Recorded data of tensile tests applied to double layered specimens that originates from the lower half of the plate. . . . .	78
G.1	Inspection of domain with the most appropriate approximation with a linear function for the slope of the $P, v$ -diagram of all tensile tests. The lower- and upperbound are fractions of the maximum load, which is the applied load at failure. . . . .	81
H.1	Recorded data of flexural tests applied to single layered specimens that originates from the upper half of the plate. . . . .	83
H.2	Recorded data of flexural tests applied to single layered specimens that originates from the lower half of the plate. . . . .	83
H.3	Recorded data of flexural tests applied to double layered specimens that originates from the upper half of the plate. . . . .	85
H.4	Recorded data of flexural tests applied to double layered specimens that originates from the lower half of the plate. . . . .	85